

TECHNISCHE UNIVERSITÄT MÜNCHEN  
Lehrstuhl für Physik funktionaler Schichtsysteme, E10

**Magnetization of correlated electron systems:  
MnSi thin films, CrB<sub>2</sub> single crystals and  
two-dimensional electron systems in MgZnO/ZnO**

Matthias Brasse

Vollständiger Abdruck der von der Fakultät für Physik der Technischen  
Universität München zur Erlangung des akademischen Grades eines

**Doktors der Naturwissenschaften**

genehmigten Dissertation.

Vorsitzender: Univ.-Prof. Dr. Peter Vogl

Prüfer der Dissertation:

1. Univ.-Prof. Dr. Dirk Grundler
2. Univ.-Prof. Dr. Peter Böni

Die Dissertation wurde am 16.10.2013 bei der Technischen Universität  
München eingereicht und durch die Fakultät für Physik am 05.02.2014  
angenommen.



# Short Abstract

Torque magnetometry at low temperature and in high magnetic fields is performed to investigate magnetic properties of material systems exhibiting electronic correlations. This work includes studies on MnSi thin films, single crystals of CrB<sub>2</sub> and two-dimensional electron systems (2DESs) formed at the interface of MgZnO and ZnO. From the experiments on MnSi we infer a preliminary magnetic phase diagram and a uniaxial magnetic anisotropy. We report the angular and temperature dependence of three de Haas-van Alphen (dHvA) frequencies in CrB<sub>2</sub> and compare the results with band structure calculations. In MgZnO/ZnO based 2DESs the dHvA effect, induced non-equilibrium currents and unexpected further signatures in the magnetization are observed. The data allow us to determine the thermodynamic energy gaps, the effective charge carrier mass, the resistance of quantum Hall states and the microscopic nature and density of the residual disorder.

Magnetische Eigenschaften von Materialsystemen, die elektronische Korrelationen aufweisen, werden bei tiefen Temperaturen und in hohen Magnetfeldern mit Drehmoment-Magnetometrie untersucht. Es handelt sich dabei konkret um MnSi-Dünnschichten, um Einkristalle aus CrB<sub>2</sub> und um zweidimensionale Elektronensysteme an der Grenzfläche von MgZnO und ZnO. Die Experimente an MnSi lassen Rückschlüsse auf das magnetische Phasendiagramm und die uniaxiale magnetische Anisotropie zu. Wir zeigen die Winkel- und Temperaturabhängigkeit von drei de Haas-van Alphen (dHvA) Frequenzen in CrB<sub>2</sub> und vergleichen die Ergebnisse mit Bandstrukturrechnungen. In MgZnO/ZnO-basierten zweidimensionalen Elektronensystemen werden der dHvA Effekt, induzierte Nicht-Gleichgewichtsströme sowie unerwartete weitere Signaturen in der Magnetisierung beobachtet. Aus den Daten lassen sich die thermodynamischen Energielücken, die effektiven Massen der Ladungsträger, die Widerstände in Quanten-Hall Zuständen sowie die mikroskopischen Eigenschaften und die Dichte von Kristallfehlern bestimmen.



# Abstract

Electronic correlations in condensed matter give rise to a manifold of electronic, magnetic or structural phenomena. This makes correlated materials interesting for basic research. If reliable methods to control and tailor the electronic correlations become available these materials are also candidates for device applications with novel functionalities.

In this thesis we investigate the magnetization of three, different, correlated electron systems: thin films of MnSi (manganese silicide), single crystals of the intermetallic compound CrB<sub>2</sub> (chromium diboride) and two-dimensional electron systems (2DESs) formed at the interface of an oxide heterostructure realized by MgZnO (magnesium zinc oxide) and ZnO (zinc oxide). We study these materials by means of highly sensitive cantilever torque magnetometry at low temperatures and in high magnetic fields. The following results are obtained:

- **MnSi thin films:** The torque magnetometry experiments allow us to infer a preliminary magnetic phase diagram. We observe two transitions: First, at  $T_c \approx 39$  K we find a transition from a paramagnetic to a magnetically ordered phase. Second, at  $B_c \approx 1$  T we identify a further transition from a non-collinear spin state to a field polarized state. Spike-like signatures are present at temperatures around 29 K and at magnetic fields of approximately 0.4 T, which point at the existence of a skyrmion phase. We study the angular dependent torque magnetization and find a dominating uniaxial magnetic anisotropy with an easy plane. The anisotropy constants range between  $1.2 \text{ kJm}^{-3}$  and  $7.9 \text{ kJm}^{-3}$ .
- **CrB<sub>2</sub>:** We study the angular and temperature dependence of the de Haas-van Alphen (dHvA) effect of a CrB<sub>2</sub> single crystal at temperatures down to 0.3 K and in magnetic fields up to 14 T. Three distinct dHvA frequencies are observed which belong to closed extremal cyclotron orbits on the Fermi surface of CrB<sub>2</sub>. Comparison

---

with electronic structure calculations<sup>1</sup> considering an incommensurate cycloidal magnetic order suggests that two of the observed dHvA oscillations arise from Fermi surface sheets formed by bands with strong B- $p_{x,y}$  character. It is likely that the third orbit corresponds to a Cr- $d$  derived Fermi surface sheet. We compare the measured effective masses with the calculated band masses and find a mass enhancement of a factor of about two. Correspondingly, upper bounds of the electron-phonon coupling constants are determined which range between 1 – 1.3 for the different orbits.

- **Two-dimensional electron system at the interface of MgZnO/ZnO:** We report the angular and temperature dependence of the dHvA effect of a 2DES in the oxide heterostructure MgZnO/ZnO. The temperature dependence of the dHvA amplitudes allows us to determine the effective charge carrier mass which yields  $m^* = 0.31 m_e$ . In addition we find that the thermodynamic energy gaps at low filling factors are enhanced over the values expected in the single particle picture, which we attribute to electron-electron interaction effects. At the same time, non-equilibrium currents (NECs) are observed. Decay times, temperature and sweep rate dependencies of the NECs are studied. From the data we infer an estimate of the resistivity of the quantum Hall state yielding  $\sim 10^{-10} \Omega/\square$ . Unexpected signatures of both, dHvA effect and NECs, allow us to identify the microscopic nature and density of residual disorder. The acceptor-type scatterers give rise to a magnetic thaw down effect which enhances the dHvA amplitude beyond the electron-electron interaction effects.

---

<sup>1</sup>Electronic structure calculations were performed by Dr. Jan Kuneš, Academy of Sciences, Praha 6 16253, Czech Republic and by Prof. Livio Chioncel, University of Augsburg, 86135 Augsburg, Germany.

# Contents

|  |           |
|--|-----------|
| <b>1. Introduction</b>   | <b>11</b> |
| <b>2. Fundamental theoretical concepts</b>                                       | <b>19</b> |
| 2.1. Magnetic Anisotropy . . . . .   | 19        |
| 2.1.1. Phenomenology . . . . .   | 20        |
| 2.1.2. Contributions to the magnetic energy density . . .                        | 21        |
| 2.1.3. Torque magnetization of thin film MnSi - model<br>calculations . . . . .  | 24        |
| 2.2. Equilibrium magnetization phenomena: De Haas-van Alphen<br>effect . . . . . | 27        |
| 2.2.1. Thermodynamic relations . . . . .   | 27        |
| 2.2.2. Quantization of orbits in a magnetic field . . . . .                      | 29        |
| 2.2.3. DHvA effect in 3DESSs . . . . .   | 31        |
| 2.2.4. DHvA effect in 2DESSs . . . . .   | 35        |
| 2.3. Non-equilibrium induced currents . . . . .                                  | 43        |
| 2.3.1. Phenomenology . . . . .   | 43        |
| 2.3.2. Charge redistribution model . . . . .                                     | 44        |
| <b>3. Micromechanical cantilever magnetometer</b>                                | <b>47</b> |
| 3.1. Principle of operation . . . . .  | 48        |
| 3.2. Capacitive readout . . . . .  | 50        |
| 3.3. Experimental setup . . . . .  | 53        |
| 3.4. Sensitivity . . . . .   | 54        |
| <b>4. Materials, sample details and preparation</b>                              | <b>57</b> |
| 4.1. MnSi thin films . . . . .   | 57        |
| 4.2. CrB <sub>2</sub> single crystals . . . . .                                  | 59        |
| 4.3. MgZnO/ZnO heterostructures . . . . .  | 60        |
| 4.4. Sensor preparation . . . . .  | 63        |
| 4.4.1. GaAs based sensors . . . . .  | 63        |

|   |            |
|---|------------|
| 4.4.2. CuBe based sensors . . . . .   | 65         |
| <b>5. Magnetization of MnSi thin films</b>  | <b>67</b>  |
| 5.1. Methods . . . . .  | 67         |
| 5.2. Experimental results . . . . .   | 68         |
| 5.3. Phase diagram inferred from torque magnetometry . . . . .                      | 72         |
| 5.4. Magnetic anisotropy . . . . .  | 75         |
| <b>6. De Haas-van Alphen effect and Fermi surface properties of CrB<sub>2</sub></b> | <b>79</b>  |
| 6.1. Experimental methods . . . . .   | 79         |
| 6.2. Experimental results . . . . .   | 80         |
| 6.2.1. Angular dependence . . . . .   | 82         |
| 6.2.2. Temperature dependence . . . . .   | 84         |
| 6.3. Electronic structure of CrB <sub>2</sub> . . . . .                             | 86         |
| 6.3.1. Theoretical methods . . . . .  | 87         |
| 6.3.2. Results from band structure calculations . . . . .                           | 87         |
| 6.3.3. Extraction of dHvA frequencies and band masses . . . . .                     | 90         |
| 6.4. Comparison of experiment and theory . . . . .                                  | 93         |
| 6.5. Comparison with MgB <sub>2</sub> . . . . .                                     | 95         |
| <b>7. Magnetization of a 2DES in a MgZnO/ZnO heterostructure</b>                    | <b>97</b>  |
| 7.1. Experimental methods . . . . .   | 98         |
| 7.2. Experimental results: Overview . . . . .                                       | 99         |
| 7.3. De Haas-van Alphen effect . . . . .  | 100        |
| 7.3.1. Angular dependence . . . . .   | 100        |
| 7.3.2. Temperature dependence of energy gaps . . . . .                              | 104        |
| 7.3.3. Discussion . . . . .   | 107        |
| 7.4. Non-equilibrium currents . . . . .   | 109        |
| 7.4.1. Sweep-rate dependence of NECs - Quantum Hall effect breakdown . . . . .      | 109        |
| 7.4.2. Decay of the induced currents . . . . .                                      | 112        |
| 7.4.3. Temperature dependence of NECs . . . . .                                     | 114        |
| 7.5. Asymmetric density of states (DOS) and nature of scattering centers . . . . .  | 116        |
| 7.6. Indications for magnetic thaw down . . . . .                                   | 118        |
| <b>8. Summary and outlook</b>   | <b>123</b> |



|   |            |
|---|------------|
| <b>Appendices</b>   | <b>128</b> |
| <b>A. Electronic structure calculations for nonmagnetic CrB<sub>2</sub></b> | <b>129</b> |
| <b>B. List of abbreviations</b>   | <b>133</b> |
| <b>List of figures</b>  | <b>135</b> |
| <b>Bibliography</b>   | <b>137</b> |
| <b>Publications</b>   | <b>149</b> |
| <b>Acknowledgments</b>  | <b>151</b> |



# Scientific collaborations

Parts of this thesis have profited from scientific collaborations. The author would like to state the contributions by the respective researchers and research groups respectively:

- The MnSi thin films were grown by the group of Prof. Thorsten Hesjedal at the University of Oxford, UK. They were provided and pre-characterized by Birgit Wiedemann from the group of Prof. Peter Böni, Technische Universität München.
- The CrB<sub>2</sub> single crystals were grown and provided by Andreas Bauer and Alexander Regnat from the group of Prof. Christian Pfleiderer, Technische Universität München.
- Band structure calculations of antiferromagnetic CrB<sub>2</sub> were performed by Dr. Jan Kuneš, Academy of Sciences, Prague, Czech Republic and by Prof. Livio Chioncel, University of Augsburg.
- MgZnO/ZnO heterostructures were provided by Y. Kozuka from the group of Prof. M. Kawasaki, University of Tokyo, Japan. Prior to our magnetometry experiments, the group of Prof. Kawasaki characterized the heterostructures via transport measurements.
- GaAs/AlAs heterostructures for the preparation of micromechanical sensors were provided by Dr. Ch. Heyn in the group of Prof. W. Hamsen, University of Hamburg.

The author would like to express his gratitude for the productive collaborations.



# 1. Introduction

The second half of the 20th century was marked by the rise of semiconductors in science and technology. Modern life would be unthinkable without semiconductor technology. For instance, about  $10^{18}$  transistors are produced every year [Ahn03]. They are employed in cars, computers or smartphones. The starting point of this boom was in the late 1940s with a major scientific breakthrough. Bardeen and Brattain invented the first transistor based on germanium [Bar48]. A transistor allows to amplify and switch electronic signals accompanied by rather low power consumption. The discovery led the foundation for the development of field effect transistors (FETs) and complementary metal-oxide-semiconductors (CMOS), which are at the heart of modern logic devices. At the same time, decisive progress in the growth of semiconductors was achieved. Sophisticated growth techniques were indispensable to synthesize ultra-clean structures and they were the key for further scientific advances and device development. For instance, Cho and Arthur invented the technique of molecular beam epitaxy (MBE) [Cho75] allowing to grow highly ordered atomic layers and high-quality heterostructures. This innovation paved the way for the growth of atomically sharp semiconductor interfaces hosting very clean low dimensional electron systems. The discovery of the quantum Hall effect in a two-dimensional electron system (2DES) realized with a silicon metal-oxide-semiconductor FET [Kli80] was a further milestone in the semiconductor research field. Up to date, the research activity in this field is still going on. Scientists search for novel ways to tailor the semiconducting materials via doping, nanostructuring or other methods. From today's point of view, this progress had enormous impact on the development of devices for applications.

Today, transistors and microchips approach already nanometer scale dimensions. Moore's law [Moo65] predicts, that the number of transistors on integrated circuits doubles every two years. Will this development continue forever? Taking into account the resolution limits set by lithography techniques and considering that the onset of quantum mechanical tunne-

ling might set limits to the further miniaturization of transistors, the end of Moore's law might be in sight. This development is also foreseen by the industry which started to look for alternative materials and architectures for computing beyond 2020 [Ard06].

A possible remedy may be to change the computing architecture conceptually. Currently, the working principle of semiconducting devices is quite conventional. They exploit the charge degree of freedom of the electrons or holes. Other degrees of freedom, for instance the one arising from spin or from orbital angular momentum, are not considered. Therefore, a key idea for further device development is to include also other degrees of freedom, which would open up a new era.

At this point, materials exhibiting electronic correlations might enter the stage. The term correlation arises from the Latin word *correlatio* - mutual relationship. In other words, the behavior of an electron is not independent of the other electrons in these systems, but they interact. This is in contrast to semiconducting materials, where electrons are generally free to move individually and usually treated in a single particle picture. Correlations between the conduction electrons are generally induced by the Coulomb interaction. They are responsible for the emergence of previously unimagined physical phenomena. Correlated materials often reveal novel ground states with fascinating electronic properties like, for instance, superconductivity, magnetism or antiferromagnetism. Furthermore, they often exhibit rich phase diagrams when exposed to external perturbations that might be provided by temperature, electric or magnetic fields. Thus, from the perspective of a scientist, correlated materials offer great opportunities to explore a rich variety of phenomena which are mediated by correlation effects and might lead to novel functionality.

Compounds which exhibit electronic correlations are mostly rather complex in terms of their composition. The materials often involve transition metals, rare earth elements or oxygen, which render in general also the electronic structure complicated. Owing to this, the research activity in this field was rather reserved. In recent years, however, enormous progress in growth and synthesis of correlated materials has been made. The methods for their characterization have been improved and a deeper theoretical understanding of correlation phenomena has been gained. It is now possible to grow for instance atomically sharp interfaces of correlated materials or to tailor bulk systems in order to control and exploit correlation effects. In this regard there are currently analogies to the development of

---

the semiconductor science some 50 years ago, as presented above. Hence, correlated materials bear great potential for functionalities and they may also become interesting for applications in the future, if reliable growth and characterization methods are available. However, it is well known that "*it is hard to beat silicon*". Or, in more general terms, due to the vast abundance of Si and the well established manufacturing techniques, we have to admit that it is unlikely that any material will replace Si on the long run. Still, correlated systems have at least the potential to complement semiconductors and to replace them in niche applications.

There is a variety of correlated materials which exhibit fascinating physical phenomena and which are potential candidates for applications. For instance, correlations are found in many differing systems including bulk crystals, thin films and low dimensional systems. Among the many different materials we focus on three highly interesting correlated electron systems in this thesis: thin films of MnSi (manganese silicide), single crystals of the intermetallic compound CrB<sub>2</sub> (chromium diboride) and 2DESs formed at the interface of an oxide based heterostructure realized by MgZnO (magnesium zinc oxide) and ZnO (zinc oxide). In the following we briefly introduce these correlated electron systems and motivate our research.

### **MnSi thin films**

Non-centrosymmetric magnetic materials have attracted enormous attention in recent years [Müh09, Lee09, Yu10a, Yu10b, Sek12, Ton12, Rit13]. This includes metallic as well as insulating compounds. Electronic correlations are omnipresent in these material systems which is manifested in the appearance of rich phase diagrams. For instance, different magnetic phases such as helical, conical and ferromagnetic order are reported [Pfl04, Müh09, Bau13]. In addition, chiral spin structures, so-called *skyrmions*, have been observed [Müh09, Ton12, Bau13]. This spin structure is particularly attractive due to its exotic topology. Skyrmions are small magnetic vortices. They are made up of a core spin with up- or downward direction. The peripheral spins twirl around the core exhibiting a unique chirality. It was found that a regular lattice of skyrmions is formed in helimagnets [Müh09, Ton12]. The dense and regular array of magnetic vortices gives rise to a gigantic topological Hall effect [Neu09] and an emergence of electrodynamics was reported [Sch12b]. The authors showed that it is possible

to move the skyrmion lattice by means of small electrical current densities. In view of these effects helimagnets are very attractive for potential applications in data storage or spintronic devices.

The prototype system in the group of helimagnets is MnSi. The phase diagram and in particular the skyrmion phase of bulk MnSi has been widely studied by a variety of different spectroscopy techniques [Müh09, Ton12, Bau13]. Very recently it became also possible to grow high-quality thin film MnSi [Hig09, Kar10, Kar11, Li13], which we address in this work. From a technological perspective, the miniaturization of MnSi is one key aspect for its integration into modern device application. However, in contrast to bulk MnSi, the magnetic properties of MnSi thin films are not yet well established. Thereupon we focus in this work on the magnetic properties of MnSi thin films and investigate the magnetic anisotropy as well as the magnetic phase diagram as a function of magnetic field and temperature.

### **CrB<sub>2</sub> single crystals**

The class of transition-metal and rare-earth diborides  $MB_2$  ( $M = \text{Cr, Mn, V, Zr, Nb, Tm, Tb, ...}$ ) comprises an unusual combination of structural properties. They exhibit high mechanical and thermal stability in combination with high electrical and thermal conductivities [Bau13]. Further, these materials offer a great variety of different electronic ground states [Nag01, Bar69, Fed09, Vaj01, Gre09]. Among them,  $MgB_2$  is an outstanding compound which has recently attracted enormous attention.  $MgB_2$  is a high-temperature superconductor [Yel02, Car03, Xi08]. Of all conventional, phonon-mediated superconducting materials it exhibits the highest superconducting transition temperature at  $T_c = 39.5$  K [Xi08]. In addition, the unique electronic structure of  $MgB_2$  gives rise to two superconducting gaps having different superconducting transition temperatures [Coo03]. So far, superconductivity was not reported in any diboride compound except for  $MgB_2$ .  $CrB_2$ , another member of the diboride family, is isostructural to  $MgB_2$ . Instead of superconductivity, antiferromagnetism was reported as ground state [Fun77, Bau13]. Intuitively the question arises, why the ground state properties of both systems are totally different although, from a structural point of view, the compounds are very similar. To answer this question the knowledge of the electronic structure of  $CrB_2$  is indispensable. Concerning  $MgB_2$ , the electronic properties have been reviewed in



---

detail [Xi08]. This is not the case for  $\text{CrB}_2$  as it only recently became possible to grow high quality single crystals [Bau13]. This allows us for the first time to tackle the electronic structure and the Fermi surface properties of  $\text{CrB}_2$ . In this work we address the electronic band structure experimentally by means of the de Haas-van Alphen (dHvA) effect.

## **2DES at the interface of MgZnO/ZnO**

Research on oxide interfaces has flourished over the past years [Oht04, Man10, Hwa12]. In bulk transition metal oxides electronic correlations already play an important role and give rise to hitherto unknown, fascinating phenomena [Dag05, Tok00]. So why care about interfaces? There are two answers to this questions. First, the introduction of interfaces into semiconductors opened the avenue for novel physics and new device opportunities. "Often it may be said that the interface is the device", was said by Herbert Kroemer in his Nobel lecture. He was right as nowadays powerful transistors, lasers, etc. rely on interfacial phenomena. Along this path it was natural to search for novel effects at the interface of correlated electron systems also. Second, at the same time, sophisticated growth techniques became available. They allowed to grow atomically sharp interfaces. The breakthrough in this research field came in 2004 with the discovery of a 2DES at the interface of the two oxide materials  $\text{SrTiO}_3$  and  $\text{LaAlO}_3$  [Oht04]. Although both materials are insulating on their own, surprisingly the interface was found to be conducting. On top of that, the 2DES formed at the interface of  $\text{LaAlO}_3$  and  $\text{SrTiO}_3$  exhibits a superconducting transition [Rey07] and also magnetism at low temperatures [Ber11, Lee13]. A multitude of correlation phenomena are thus present in this multilayer system.

Another oxide heterostructure, formed by  $\text{ZnO}$  and  $\text{MgZnO}$ , also started to attract enormous attention when an interface 2DES was reported [Tsu07, Ram07, Hwa12]. In contrast to the  $\text{SrTiO}_3/\text{LaAlO}_3$  2DES, which exhibits a relatively low mobility on the order of  $1000 \text{ Vs/cm}^2$  [Man10], the  $\text{MgZnO}/\text{ZnO}$  based 2DES exhibits high mobilities on the order of  $500,000 \text{ Vs/cm}^2$  at  $\sim 1 \text{ K}$  [Tsu07, Tsu08, Tsu10] almost competing with standard semiconductor based 2DESs. The high quality of the 2DES allowed to investigate the quantum Hall effect (QHE) in an oxide heterostructure for the first time [Tsu07]. Besides, the observation of both fractional QHE [Tsu10] and quantum Hall ferromagnetism [Koz12] indicates, that field

induced correlation effects play an important role at this interface. In this work we investigate the magnetization of the 2DES at the interface of MgZnO/ZnO, which has not been addressed so far. By this means we intend to get insights into the ground state energy spectrum of the 2DES, which cannot be accessed via excitation spectroscopy.

### Outline

In this work we employ cantilever magnetometry to investigate experimentally the aforementioned material systems. This allows us

- to study the magnetic anisotropy and the magnetic phase diagram of MnSi thin films,
- to provide the Fermi surface topology and the effective masses of charge carriers in CrB<sub>2</sub> single crystals,
- to investigate equilibrium and non-equilibrium magnetization phenomena in MgZnO/ZnO based 2DESs.

The thesis is organized as follows: In Chapter 2 the basic theoretical concepts relevant for this work are introduced. This chapter is subdivided into the categories magnetic anisotropy, equilibrium magnetization phenomena and non-equilibrium magnetization phenomena. In the first part, a phenomenological approach is used to introduce the concept of magnetic anisotropy and the respective energy contributions. Following a simple energy ansatz we derive the expected torque magnetization of a MnSi thin film applying numerical model calculations. Second, the equilibrium magnetization properties of three- and two-dimensional electron systems are discussed. The derivation of the dHvA effect from a free energy approach is sketched. Furthermore we show how to include effects of finite temperature and residual disorder in the discussion. Third, we consider non-equilibrium magnetization phenomena, i.e. non-equilibrium induced currents, again using a phenomenological approach.

Chapter 3 is dedicated to the introduction of the experimental techniques. This includes the description of the cantilever magnetometer, the experimental setup as well as a consideration of the experiment sensitivity.

In Chapter 4 the investigated material systems are introduced and basic

---

properties are discussed. This is followed by a description of the preparation techniques used in this work.

The magnetization of MnSi inferred from cantilever magnetometry is discussed in Chapter 5. Our results suggest a preliminary phase diagram. Further we discuss the magnetic anisotropy of MnSi thin films.

The dHvA effect and Fermi surface properties of CrB<sub>2</sub> are presented in Chapter 6. The analysis of the dHvA data as a function of magnetic field strength, field angle and temperature allows us to provide the topology of certain parts of the Fermi surface of CrB<sub>2</sub> and to determine the effective masses of the charge carriers along with mean free paths. The experimental data is compared to band structure calculations to allow for a comprehensive interpretation of the data.

In Chapter 7 we discuss the magnetization of MgZnO/ZnO based 2DESs. We observe and analyze the dHvA effect and non-equilibrium induced currents. Thereby we get information about the ground state energy spectrum of the 2DES as well as about the underlying density-of-states (DOS).

Finally, the results are summarized in Chapter 8 and a brief outlook is given.



## 2. Fundamental theoretical concepts

In this chapter fundamental theoretical concepts relevant for this work are introduced. It divides into three main parts.

In the first part we consider ferromagnetic thin films exposed to external magnetic fields. In this regard the concept of magnetic anisotropy will be discussed. Here, we follow a phenomenological approach. Further, we introduce the contributions to the magnetic free energy of a ferromagnetic material. This allows us to model the torque magnetization of a ferromagnetic MnSi thin film in a simple approach.

Second, the equilibrium magnetization of two and three dimensional electron systems in high magnetic fields and at low temperature is discussed. In other words, we recall the Landau diamagnetism of an electron gas. Starting from a quantum mechanical point of view the quantization of electrons in high magnetic fields is revisited. In conjunction with a thermodynamic approach the dHvA effect is then derived. We show how to treat finite temperature and disorder effects either by an analytical approach, the so-called Lifshitz-Kosevich formalism, or by numerical model calculations.

Third, we introduce the effect of non-equilibrium currents (NECs) in a 2DES. Here, we give a brief overview of the phenomenological understanding of NECs before we focus on the magnetization arising from induced currents in a 2DES.

### 2.1. Magnetic Anisotropy

Below a critical temperature  $T_c$  a ferromagnetic material exhibits a spontaneous magnetization  $\mathbf{M}$  in absence of an external field  $\mathbf{B}$ . The term magnetic anisotropy is used to describe the dependence of the energy of a ferromagnet on the direction of the magnetization. In an isotropic magnetic material the magnetization has no preferential direction in absence

of a magnetic field. Conversely, in a magnetically anisotropic material the magnetization direction will preferably align along a direction corresponding to a local minimum of the energy surface. The direction pointing towards a local minimum is usually referred to as the easy axis. Directions of large energy are called hard axes [Sko08]. The origin of magnetic anisotropy can be intrinsic as well as extrinsic. Intrinsic contributions may stem from the symmetry of the host crystal. It is usually referred to as magnetocrystalline anisotropy. The shape of a sample can also induce an anisotropy. An extrinsic source of magnetic anisotropy is for instance provided by stress which causes magnetoelastic anisotropy.

In this section we introduce the magnetic anisotropy contributions relevant for the description of MnSi thin films exposed to a magnetic field. Note, that we introduce the anisotropy in a phenomenological approach following Refs. [Mor01, Chi09]. For simplicity we do not consider microscopic origins. These can be found for instance in Ref. [Sko08]. Furthermore we discuss the contributions to the magnetic energy density. Finally numerical calculations are performed which specifically model the magnetic energy and the related torque magnetization curves of ferromagnetic MnSi thin films.

### 2.1.1. Phenomenology

In a phenomenological ansatz, the anisotropy is modeled by symmetry considerations and anisotropy constants are commonly used to parametrize the dependence of the magnetic anisotropy on the magnetization angle. The simplest and most common phenomenological anisotropy model is a uniaxial anisotropy. Let us consider the coordinate system shown in Fig. 2.1. The following parametrization of the magnetization  $\mathbf{M}$  and the magnetic field  $\mathbf{B}$  in terms of polar coordinates is used:

$$\mathbf{M} = (M, \Theta, \Phi) \quad (2.1)$$

$$\mathbf{B} = (B, \vartheta, \varphi) \quad (2.2)$$

If we assume a magnet of volume  $V$  exhibiting a uniaxial anisotropy along the  $\mathbf{z}$ -direction, the corresponding uniaxial anisotropy energy density  $E_a/V$  can be expanded in a series of powers of  $\cos^2 \Phi$  [Mor01, Chi09]

$$E_a/V = K_u^1 \cos^2 \Phi + K_u^2 \cos^4 \Phi + \dots, \quad (2.3)$$

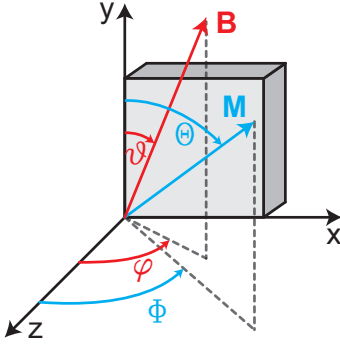


**Figure 2.1.:** Coordinate system relative to the sample.

where  $K_u^i$  denotes the  $i$ -th order anisotropy constant. In most materials, the magnitude of the individual terms decrease significantly with increasing order  $i$  [Sko08]. Since the materials investigated in this work were found to exhibit only first order anisotropies, we neglect higher order terms from now on and set  $K_u^1 = K_u$ . The energy surfaces of a first order uniaxial anisotropy along  $z$  are depicted in Fig. 2.2. For  $K_u > 0$ , the energy surface forms a prolate spheroid extended along the  $z$  direction (magnetic hard axis) with minimum energy in the  $x, y$ -plane (magnetic easy plane). For  $K_u < 0$  an oblate spheroid is recovered with a magnetic easy axis along  $z$  and a magnetic hard  $x, y$ -plane.

Apart from uniaxial anisotropies, crystals with cubic anisotropy are also quite common. Examples are the itinerant ferromagnets nickel or iron. However, the MnSi thin film studied in this work did not reveal cubic anisotropies, as will be detailed in the next section. Therefore, a discussion of cubic anisotropy is omitted here.

### 2.1.2. Contributions to the magnetic energy density

In this section the contributions to the magnetic energy density  $E/V$  will be introduced. We consider contributions from the Zeeman energy, the shape anisotropy as well as the magnetocrystalline anisotropy.

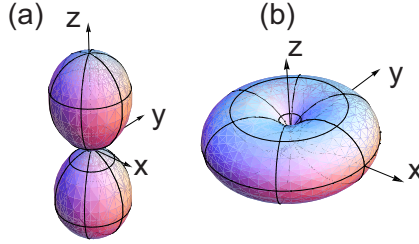


**Figure 2.2.:** First-order energy density surfaces sketched for a uniaxial anisotropy along  $\mathbf{z}$ . (a) For  $K_u > 0$ , the energy density surface forms a prolate spheroid extended along the  $\mathbf{z}$  direction (magnetic hard axis) with minimum energy in the  $x, y$ -plane (magnetic easy plane). (b)  $K_u < 0$  results in an oblate spheroid with a magnetic easy axis along  $\mathbf{z}$  and a magnetic hard  $x, y$ -plane.

### Zeeman interaction

The Zeeman energy density  $E_Z/V$  describes magnetostatic energy of the magnetization  $\mathbf{M}$  in an external field  $\mathbf{B}$ . It is given by

$$E_Z/V = -\mathbf{M} \cdot \mathbf{B}. \quad (2.4)$$

$\mathbf{M}$  preferably aligns along  $\mathbf{B}$  due to the Zeeman term. However, strictly speaking the Zeeman energy is not an anisotropy energy in the classical meaning since it vanishes at  $B = 0$ .

### Shape anisotropy

If a sample is magnetized there is in general a discontinuity of the magnetization at its surface. As a consequence, the divergence of  $\mathbf{M}$  is non-vanishing  $\nabla \cdot \mathbf{M} \neq 0$ . In order to fulfill Maxwell's equation  $\nabla \cdot \mathbf{B} = \mu_0 \nabla \cdot (\mathbf{H} + \mathbf{M}) = 0$  an equal and opposing divergence of  $\mathbf{H}$  has to be induced. This field is commonly referred to as the demagnetizing field. It arises from magnetic dipolar interactions which induce magnetic surface poles. The contribution to the energy density, the so-called shape anisotropy or demagnetization term, can be expressed as

$$E_D/V = \frac{1}{2} \mu_0 \mathbf{M} \cdot \tilde{\mathbf{N}} \cdot \mathbf{M}. \quad (2.5)$$



$\tilde{N}$  denotes the demagnetization tensor which depends on the sample shape. For a thin film, as discussed in this work, all components of  $\tilde{N}$  vanish except for the one which describes the direction perpendicular to the film surface. It is given by  $N_{\perp} = 1$  [Chi09]. Assuming a thin film with sample normal  $\mathbf{n} \parallel \mathbf{z}$  the shape anisotropy can be written as

$$E_D/V = \frac{1}{2}\mu_0 M^2 \cos^2 \Phi. \quad (2.6)$$

In this configuration the shape anisotropy turns into a uniaxial anisotropy favoring an in plane magnetization orientation. The corresponding energy surface is shown in Fig. 2.2 (a).

### Magnetocrystalline anisotropy

In most cases the symmetry of a crystal influences the direction of the spontaneous magnetization. This effect is usually referred to as magnetocrystalline anisotropy. Microscopically, the primary source of magnetocrystalline anisotropy is spin-orbit coupling [Mor01] which causes the magnetic moments to couple to the orbital motion of the electrons and thereby to the crystal axes.

In this thesis MnSi thin films grown on Si substrates were investigated (see Sec. 4.1 for material properties). Although bulk MnSi crystallizes in the cubic structure [Bau13], Ref. [Kar12] reported a strong uniaxial, easy plane type anisotropy in thin film MnSi. This is due to epitaxially induced tensile stress. In analogy to Ref. [Kar12] we treat this phenomenon as a uniaxial magnetocrystalline anisotropy density  $E_C/V$ . In first order it takes the form (c.f. Eq. 2.3)

$$E_C/V = K_u \cos^2 \Phi. \quad (2.7)$$

In helimagnets such as MnSi, the exchange interaction and the Dzyaloshinskii-Morya interaction are usually also considered [Bak80, Kar12]. These energy contributions are essential to explain the formation of the helical, conical or skyrmion phase. In this work, however, we do not have clear evidence for the existence of those phases (c.f. Chapter 5). Therefore it is questionable whether the two energy contributions play a dominant role for our data and observations. Therefore we do not regard the exchange and the Dzyaloshinskii-Morya interaction in the following

model calculations.

### 2.1.3. Torque magnetization of thin film MnSi - model calculations

In this section we present numerical model calculations of the torque magnetization of MnSi thin films. They are based on the anisotropy energy considerations shown above. The results of the calculations are instructive by themselves and further they will be helpful to analyze and interpret the experimental results shown in Chapter 5.

For the calculations the following assumptions were made: First, we neglect domain effects. Instead we model a single domain state of MnSi using a macrospin approach (c.f. Stoner-Wohlfahrt model, [Sto48]). Second, to agree with the experiment, we set  $\vartheta = 90^\circ$  such that the magnetic field rotates in the  $(x, z)$ -plane. Thus, the magnetic field orientation is fully described by the angle  $\varphi$  as depicted in Fig. 2.1. Third, by definition the torque axis points along the  $y$  direction, to comply with the experimental situation (c.f. Chapter 3). In regard of this we do not consider the  $y$  component of  $\mathbf{M}$  in the following calculations, because our torque magnetometer is not designed to be sensitive on this component in the experiment. Finally, it is convenient to introduce the anisotropy field  $B_a$  given by [Bur77]

$$B_a = 2K_u^*/M_s, \quad (2.8)$$

to compare the effect of anisotropies with the strength of the applied magnetic field  $B = \mu_0 H$ . Here,  $M_s$  denotes the saturation magnetization and  $K_u^*$  is the effective anisotropy constant as defined below in Eq. 2.11.

The anisotropy energy density of the MnSi thin film in a magnetic field is given by

$$E_a/V = (E_Z + E_C + E_D)/V, \quad (2.9)$$

with Zeeman term  $E_Z$ , anisotropy energy  $E_A$  and demagnetization term  $E_D$ . For a uniaxial anisotropy the energy can then be rewritten as

$$E_a/V = -MB \cos(\Phi - \varphi) + K_u \cos^2 \Phi + \frac{1}{2} \mu_0 M^2 \cos^2 \Phi. \quad (2.10)$$

Hence, we can summarize the anisotropy terms arising from shape and magnetocrystalline anisotropies to give an effective anisotropy constant

$$K_u^* = K_u + 1/2\mu_0 M^2. \quad (2.11)$$

For a given field strength  $B$ , field direction  $\varphi$  and magnetization magnitude  $M$ , the orientation of  $\mathbf{M}$  in equilibrium, i.e. the angle  $\Phi$ , is obtained by minimizing Eq. 2.10 with respect to  $\Phi$ :

$$\frac{1}{V} \frac{\partial E_a}{\partial \Phi} = 0 \quad (2.12)$$

The resulting torque density  $\Gamma/V = \mathbf{M} \times \mathbf{B}$  is then calculated from

$$\Gamma/V = M \cdot B \cdot \sin(\Phi - \varphi). \quad (2.13)$$

This formalism allows us to simulate the torque  $\Gamma$  as a function of  $\varphi$  for different values of  $B$ .

In a first set of model calculations, we assume that the MnSi film is saturated such that  $M = M_s$ . According to Ref. [Li13] the saturation magnetic moment per Mn atom in the cubic unit cell amounts to  $0.42 \mu_B$ . For a given sample of area  $A = 3.1 \times 3.6 \text{ mm}^2$  and film thickness  $d_{\text{MnSi}} = 30 \text{ nm}$  (c.f. sample *SI 097*, Chapter 4) the magnetization yields  $M_s = 1.64 \cdot 10^5 \text{ JT}^{-1}\text{m}^{-3}$ . The authors of Ref. [Kar12] reported values of  $K_u$  for different film thicknesses. For the given sample parameters an anisotropy constant  $K_u \approx 4 \text{ kJT}^{-1}\text{m}^{-3}$  is reported. Hence, the resulting anisotropy field yields  $B_a \approx 0.25 \text{ T}$ .

Correspondingly simulated torque curves are shown in Fig. 2.3. Following Ref. [Bur77], the shape of the  $\Gamma(\varphi)$  curve is determined by the relation between anisotropy field  $B_a$  and  $B$ . To illustrate this effect, we show  $\Gamma$  for  $B = 0.04 \text{ T}$ ,  $B = 1.5 \text{ T}$  and  $B = 10 \text{ T}$  in Fig. 2.3. For  $B < B_a$  ( $B = 0.04 \text{ T}$ ) the magnetization does not follow the external field. The uniaxial anisotropy dominates and the magnetization resides near the easy axis all the time. As a consequence,  $\Gamma(\varphi)$  shows the periodicity of a sinusoidal function with small torque amplitudes. At very large field  $B = 10 \text{ T} \gg B_a$ ,  $\mathbf{M}$  follows  $\mathbf{B}$  closely and  $\Gamma(\varphi)$  strictly reflects the periodicity of the magnetocrystalline anisotropy energy term, which in our case is a uniaxial anisotropy proportional to  $\cos^2 \varphi$ . For  $B = 1.5 \text{ T}$ , which complies well with our experimental situation, the curve periodic-

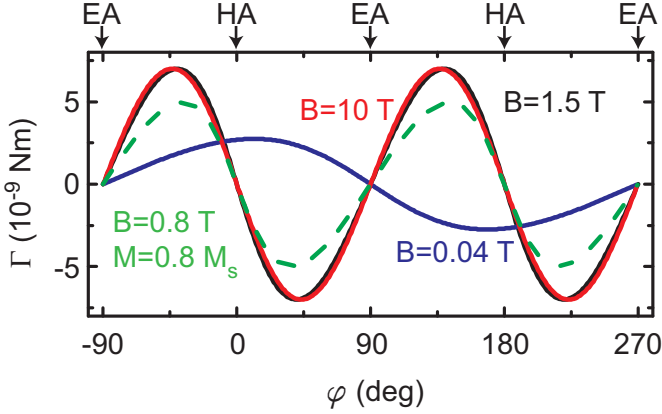


**Figure 2.3.:** Simulation of  $\Gamma(\varphi)$  for a ferromagnetic single domain MnSi thin film with  $A = 3.1 \times 3.6 \text{ nm}^2$  and  $d_{\text{MnSi}} = 30 \text{ nm}$ . The solid curves are obtained for a saturated film with  $M = M_s$ . For  $B = 0.04 \text{ T}$  ( $B < B_a$ ) the magnetization does not follow the external field as the anisotropy energy dominates and the torque is a sinusoidal function with small amplitude. For  $B = 1.5 \text{ T}$  and  $B = 10 \text{ T}$  ( $B > B_a$ ),  $M$  follows the external field more closely as the energy term is dominated by the Zeeman energy. The resulting torque exhibits the periodicity of the uniaxial anisotropy induced by the crystal and the sample shape. The torque maxima are independent of the field strength in this regime. The dashed curve is obtained for  $B = 0.8 \text{ T}$  and  $M = 0.8 M_s$ . The torque peak-to-peak variation is reduced compared to the saturated MnSi film.

ity is equal to the one at  $B \gg B_a$  and thus governed by the anisotropy term. Further, it is important to note that the amplitudes of the torque extrema are independent of the field strength  $B$  for  $B \gg B_a$ . According to Refs. [Bur77, Chi09] the maximum torque values are directly related to the anisotropy constant  $K_u^*$  in the high field regime.

From Eq. 2.10 we infer that  $E_a/V$  takes a local minimum at  $\varphi = 90^\circ$  and  $\varphi = 270^\circ$ , which corresponds to the fact that  $\mathbf{M}$  lies in the easy plane. In the simulation we find at  $\varphi = 90, 270^\circ$  a rather shallow slope for small  $B$  with  $B > B_a$ . This is an indication for the position of the easy axis (EA) [Hub98]. In contrast, near  $\varphi = 0^\circ$  and  $\varphi = 180^\circ$  the slope is steeper which indicates the hard axis (HA).

In addition, we performed calculations assuming that the external field is

too weak to saturate the MnSi film. For this case phenomenological differences to the case discussed above are identified: The resulting behavior of the angular dependent torque is shown by the dashed curve in Fig. 2.3. Here,  $B$  was set to 0.8 T and  $M = 0.8 M_s$ . Although  $B$  is larger than the anisotropy field  $B_a$ , the peak-to-peak variation is smaller compared to the case when  $M = M_s$ . In this scenario no direct conclusion about the anisotropy constant  $K_u^*$  can be inferred because the extrema depend on the value of  $M$  [Bur77, Chi09].

## **2.2. Equilibrium magnetization phenomena: De Haas-van Alphen effect**

In 1930 de Haas and van Alphen discovered the oscillatory variation of the magnetic susceptibility as a function of the magnetic field in the semimetal bismuth [Haa30]. Nowadays, these oscillations are usually referred to as the de Haas-van Alphen effect [Ash76]. Since its discovery the dHvA effect has been studied intensively in various solid state systems such as metals, heavy fermion systems, superconductors or low dimensional electron systems [Sho84, Suz93, Car03, Stö83]. The dHvA effect is a pure quantum mechanical phenomenon and hence it provides valuable information about the quantum mechanical ground state of the host system. In particular regarding three dimensional electron systems (3DESs), the dHvA effect became a powerful and well established tool to determine Fermi surface properties, scattering rates and effective masses. Reference [Sho84] provides an extensive review on the dHvA in metals. The dHvA effect in 2DESs has rarely been studied. This is due to the weaker signal strength in low dimensional systems as will be discussed in Sec. 3.4. Importantly, the dHvA effect provides a direct quantitative measure of thermodynamic ground state properties in a 2DES. It is a magnetization phenomenon occurring in thermodynamic equilibrium. Non-equilibrium phenomena, such as induced currents, will be discussed in the next section. In the following a brief review on the basic concepts of the dHvA effect is given.

### **2.2.1. Thermodynamic relations**

The magnetization  $M$  is a thermodynamic quantity and is directly related to several thermodynamic quantities of an electron system. For the deriva-

## 2. Fundamental theoretical concepts

---

tion of  $M$  it is convenient to introduce the Helmholtz free energy  $F$  and the thermodynamic potential  $\Omega$  given by

$$F = U - TS, \quad \Omega = F - \chi N, \quad (2.14)$$

with the internal energy  $U$ , the entropy  $S$  and the temperature  $T$ . The thermodynamic potential depends further also on the chemical potential  $\chi$  and the particle number  $N$ . The corresponding differentials yield:

$$dF = -SdT - MdB + \chi dN \quad (2.15)$$

$$d\Omega = -SdT - MdB + Nd\chi. \quad (2.16)$$

Please note, that we ignore the vector character of  $M$  and  $B$  for the moment. The magnetization is related to the free energy and the thermodynamic potential by

$$M = - \left( \frac{\partial F}{\partial B} \right) \Big|_{T,N}, \quad M = - \left( \frac{\partial \Omega}{\partial B} \right) \Big|_{T,\chi}. \quad (2.17)$$

Thus, one can use either  $F$  or  $\Omega$  to derive  $M$  and conceptually there is no difference in both methods. In 3D systems, it turns out that, from a mathematical point of view, it is more convenient to use  $\Omega$  instead of  $F$  [Sho84]. In 2D systems, however, we will rely on  $F$  to determine  $M$ . For the 2DES we regard a system with fixed particle number  $N$  instead of a fixed chemical potential and  $F$  is the natural quantity to derive  $M$ .

For  $T \rightarrow 0$  we may replace  $F$  by  $U$  in Eq. 2.17. In other words, in the limit of low temperatures the magnetization directly reflects the thermodynamic ground state energy  $U$ . Measuring the equilibrium magnetization  $M$  as a function of  $B$  thus provides direct information about the thermodynamic ground state energy spectrum of the system.

Moreover, from Eq. 2.15 the Maxwell relation

$$\left( \frac{\partial M}{\partial N} \right) \Big|_B = - \left( \frac{\partial \chi}{\partial B} \right) \Big|_N \quad (2.18)$$

can be deduced. It provides a link between the chemical potential  $\chi$  and the magnetization  $M$ . This will be useful to determine the thermodynamic energy gaps from the dHvA oscillations in 2DESs (c.f. Eq. 2.43).

### 2.2.2. Quantization of orbits in a magnetic field

In the classical picture, electrons exposed to an external magnetic field experience the Lorentz force. In response the electrons start to orbit around the magnetic flux lines. In this section we treat this situation by means of quantum mechanics which will finally lead to the well-known quantization of the electron orbits in response to a uniform magnetic field [Ash76]. We consider a free electron gas of non-interacting charge carriers with effective mass  $m^*$ . The Hamiltonian for noninteracting electrons in a magnetic field of the form  $\mathbf{B} = (0, 0, B_z)$  is given by

$$\hat{H} = \frac{(\hat{p} + e \cdot \mathbf{A})^2}{2m^*}, \quad (2.19)$$

where  $\hat{p} = \frac{\hbar}{i}\nabla$  denotes the momentum operator and  $\mathbf{A}$  is the vector potential. In the Landau gauge  $\mathbf{A} = (0, x \cdot B_z, 0)$  the Schrödinger equation (SE) yields

$$\left[ \frac{\partial^2}{\partial x^2} + \left( \frac{\partial}{\partial y} - \frac{ieB_z}{\hbar} \cdot x \right)^2 + \frac{\partial^2}{\partial z^2} + \frac{2m^*}{\hbar^2} \cdot E \right] \Psi(x, y, z) = 0. \quad (2.20)$$

The solution takes the form  $\Psi(x, y, z) = e^{i(\beta y + k_z z)} u(x)$  which we insert into the SE to obtain the equation of a harmonic oscillator:

$$\left[ \frac{-\hbar^2}{2m^*} \frac{\partial^2}{\partial x^2} + \frac{m^* \omega_c^2}{2} (x - x_0)^2 \right] u(x) = \left( E - \frac{\hbar^2 k_z^2}{2m^*} \right) u(x). \quad (2.21)$$

Here,

$$\omega_c = \frac{eB}{m^*} \quad (2.22)$$

denotes the cyclotron frequency,  $x_0 = -k_y l_B^2$  is the guiding center coordinate of a cyclotron orbit in real space and  $l_B = (\hbar/eB)^{1/2}$  is the magnetic length.  $k_i$  stands for the  $i$ -th component of the wavevector  $\mathbf{k}$ . The corresponding eigenenergies are given by

$$E_j = \left( j + \frac{1}{2} \right) \hbar \omega_c + \frac{\hbar^2 k_z^2}{2m^*} \quad j = 0, 1, 2, \dots \quad (2.23)$$

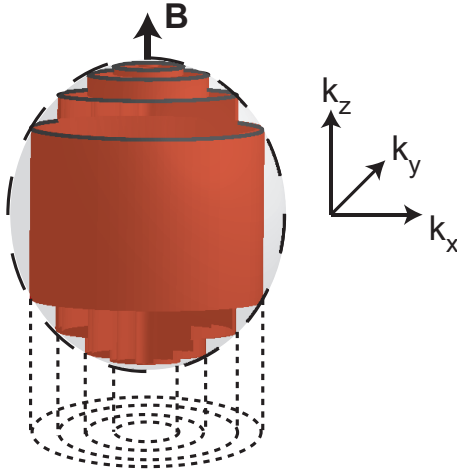


**Figure 2.4:** Schematic sketch of Landau tubes for a free electron gas whose surfaces of constant energies are spherical. The Landau tubes are cylindrical with a common axis along  $\mathbf{B}$ . A hypothetical Fermi surface is depicted by the broken curve. Only the parts of the Landau tube inside the Fermi surface are occupied at  $T = 0$ .

Let us consider the resulting eigenenergies in reciprocal space. In the plane perpendicular to the external field, i.e. the  $(k_x, k_y)$ -plane, the energy is quantized and the allowed states follow circles. The electron motion along  $k_z$  is not affected by the magnetic field and the parabolic energy term is recovered. In sum the permitted states lie on tubes in  $\mathbf{k}$ -space, the so-called Landau levels (LLs), as schematically depicted in Fig. 2.4 for a free electron gas. The Landau tubes are cylindrical in this case with a common axis parallel to the external field  $\mathbf{B}$ . Further, a hypothetical spherical Fermi surface (FS) is depicted by the broken curve. Only states inside the FS are occupied at  $T = 0$ . Note that in general, i.e. for an arbitrary energy landscape in a solid state system, there is no requirement that the tubes are cylindrical or that they run parallel to  $\mathbf{B}$  [Sho84].

For any particular value of  $k_z$  the LLs are degenerate. If the sample area perpendicular to the quantizing field is given by  $\mathcal{A} = L_x \cdot L_y$  the distance between two guiding centers is given by  $\Delta x_0 = \Delta k_y l_B^2 = \left(\frac{2\pi}{L_y}\right) (\hbar/eB)$ .



## 2.2. Equilibrium magnetization phenomena: De Haas-van Alphen effect

For a given  $k_z$  this results in the number of states with constant energy  $N = \frac{L_x}{\Delta x_0} = L_x L_y eB/h$ . Per unit area and considering spin degeneracy  $g_s$  we obtain as degeneracy of the LLs

$$N_L = \frac{eB}{h} \cdot g_s. \quad (2.24)$$

For a spin degenerate system  $g_s = 2$ . Notice, that both, the Landau energies and their degeneracy increase linearly as a function of magnetic field. The quantization of the electron motion therefore obviously affects the density-of-states (DOS) and the magnetization of solids which finally leads to the dHvA effect. In the following we sketch the derivation of the dHvA effect for the more general case of a 3D electrons system with arbitrary Fermi surface. After that we turn to the special case of a 2DES, which is intuitively easier to understand.

### 2.2.3. DHvA effect in 3DESs

In this section we discuss the dHvA effect in 3D. Its derivation involves very elaborate mathematics and because of that only the main results which are important for this thesis are shown and interpreted here. An extensive review can be found in Refs. [Sho84, Zim65]. We first consider an ideal electron gas at  $T = 0$  and include finite temperature or disorder effects at a later stage.

#### Ideal electron gas at $T = 0$

The derivation starts from the thermodynamic potential  $\Omega$  introduced in Eq. 2.14. Again, without loss of generality  $\mathbf{B} \parallel \mathbf{z}$  is assumed. At  $T = 0$  and for an electron system of volume  $V$ ,  $\Omega$  is given by

$$\Omega = -\frac{V e B}{\pi^2 \hbar} \sum_j \int_0^{k_j} (\chi - E_j) dk_z, \quad (2.25)$$

where the summation is over all possible states  $E_j$ . The upper limit of integration  $k_j$  is the value of  $k_z$  such that  $\hbar^2 k_j^2 / 2m^* = \chi - (j + 1/2)\hbar\omega_c$ . Performing the integration assuming an arbitrary shaped FS and non-interacting electrons the oscillatory part of the thermodynamic potential is

## 2. Fundamental theoretical concepts

---

obtained as a function of  $B$ :

$$\Omega_{\text{osc}} = \text{const} \times \frac{B^{5/2}}{\sqrt{P''}} \sum_{p=1}^{\infty} \frac{1}{p^{5/2}} \cos \left[ 2\pi p \left( \frac{\hbar P}{2\pi e B} - \frac{1}{2} \right) \pm \frac{\pi}{4} \right] \quad (2.26)$$

$P$  denotes the area of the extremal cross section of the Fermi surface in the plane perpendicular to the direction of  $B$ .  $P''$  is the corresponding local curvature of the Fermi surface around the extremal cross section. The formula can be interpreted with the help of Fig. 2.4. According to Eq. 2.23 the Landau tubes grow outwards as the magnetic field increases and its intersection with the Fermi surface moves up or down. In this field regime the effect on the energy, i.e. the thermodynamic potential, is negligible. At an extremal area, however, the tube leaves the Fermi surface altogether. This process has a significant effect on the energy. According to Eq. 2.23 the energy separation of Landau tubes is given by  $\hbar\omega_c$ . Thus  $\Omega_{\text{osc}}$  varies periodically. The periodicity finds its manifestation in the  $\cos$  term in Eq. 2.26. Considering only the first harmonic ( $p = 1$ ) the periodicity is given by

$$\frac{\hbar P}{eB} = 2\pi(n + \gamma), \quad (2.27)$$

where  $n$  is an integer and  $\gamma$  is a phase correction. In other words, the oscillations in the energy are periodic in  $1/B$  and the corresponding frequency  $f$  is directly related to the extremal cross section of the Fermi surface by the Onsager relation [Ons52]

$$P = \frac{2\pi e f}{\hbar}. \quad (2.28)$$

Note that a complicated Fermi surface may have several extremal cross sections perpendicular to the field direction. They all contribute with an oscillatory term of the form shown in Eq. 2.26.

$M$  can be determined by differentiating  $\Omega$  with respect to  $B$  as shown in Eq. 2.17. However, at this point we have to take the vector character of  $M$  and  $B$  into account. It is convenient to divide the oscillatory magnetization  $\mathbf{M}$  into a component parallel ( $M_{\parallel}$ ) and perpendicular ( $M_{\perp}$ ) to  $\mathbf{B}$ . At  $T = 0$

## 2.2. Equilibrium magnetization phenomena: De Haas-van Alphen effect

they are given by [Sho84]

$$M_{\parallel}^0 = \text{const} \times \frac{fB^{1/2}}{\sqrt{P''}} \sum_{p=1}^{\infty} \frac{1}{p^{3/2}} \sin \left[ 2\pi p \left( \frac{\hbar P}{2\pi eB} - \frac{1}{2} \right) \pm \frac{\pi}{4} \right] \quad (2.29)$$

$$M_{\perp}^0 = -\frac{1}{f} \frac{\partial f}{\partial \theta} M_{\parallel}. \quad (2.30)$$

As expected, the magnetization oscillates periodically with the reciprocal field. Here,  $\frac{\partial f}{\partial \theta}$  denotes the partial derivative of the dHvA frequency  $f$  with respect to  $\theta$ , specifying the direction of  $\mathbf{B}$  in the plane in which the variation of  $\Omega$  is most significant [Sho84]. Further,  $\frac{\partial f}{\partial \theta}$  is often considered as a so-called anisotropy factor because it takes the anisotropy of the Fermi surface into account. For instance, for a highly symmetric Fermi surface (e.g. a sphere)  $\frac{\partial f}{\partial \theta}$  vanishes. In this case the perpendicular magnetization component  $M_{\perp}^0$  disappears.

### Lifshitz-Kosevich formalism

So far, the idealized situation of a free electron gas at zero temperature was discussed. In reality, however, certain aspects have to be considered which all lead to a damping and phase smearing of the dHvA oscillations [Sho84]. In our discussion we include now the effects of finite relaxation time and finite temperature. This is done in the framework of the well established Lifshitz-Kosevich (LK) formalism [Lif54, Lif55, Din52, Sho84, Was96].

- Finite temperature

At finite temperature  $T$ , the Fermi distribution

$$\mathcal{F}(E, \chi, T) = \left[ 1 + \exp \left( \frac{E - \chi}{k_{\text{B}} T} \right) \right]^{-1} \quad (2.31)$$

governs the occupation of the allowed states. It can be shown that the effect of finite temperature can be included in the above schematics by introducing a reduction factor  $R_{\text{T}}$ . It takes the form

$$R_{\text{T}} = \frac{X}{\sinh X}, \quad \text{with } X = \frac{2\pi^2 k_{\text{B}} m^* T}{\hbar e B}. \quad (2.32)$$

- Finite relaxation time

## 2. Fundamental theoretical concepts

---

Electron scattering due to residual disorder leads to a broadening of the otherwise sharp Landau levels. This effect is usually described in terms of a finite relaxation time  $\tau$ . As shown by Dingle [Din52] a finite relaxation time leads to a reduction of the oscillation amplitude which can be modeled by a reduction factor of the form

$$R_D = \exp\left(-\frac{\pi m_b}{eB\tau}\right). \quad (2.33)$$

Here,  $m_b$  denotes the electronic band mass. It is in general different from the quasiparticle effective mass  $m^*$ , which can be renormalized by many-body interactions.

Including the effects of finite temperature and finite relaxation time the oscillatory part of the magnetization (see Eq. 2.29) can be rewritten to give the LK formula

$$M_{\parallel} = M_{\parallel}^0 R_T R_D \quad (2.34)$$

$$M_{\perp} = M_{\perp}^0 R_T R_D. \quad (2.35)$$

In conclusion, the LK formalism provides a valuable tool to include the effects of finite temperature and finite sample disorder in the analysis of the dHvA oscillations. It allows to quantify important material parameters such as the effective mass  $m^*$  or the relaxation time  $\tau$ .

Note that the LK formalism as derived here is strictly only true for a 3D system with constant chemical potential. The formation of well separated LLs, however, induces oscillations of the chemical potential. When a Landau tube leaves a Fermi surface as shown in Fig.2.4,  $\chi$  moves to the next Landau tube. The corresponding oscillation amplitude in  $\chi$  is negligible, because the occupancy change of one LL is much smaller than the number of charge carriers enclosed by the whole Fermi surface [Sho84, Ush09]. This justifies the assumption of a constant chemical potential.

Regarding a 2DES, this is generally not the case as will be elaborated in the next section. All the same the LK formalism has also proven to give consistent results when dealing with 2DESs [Sho84, Ush09]. Therefore, we also rely on the LK formalism when analyzing the dHvA oscillation in a 2DES as done in Chapter 7.

### 2.2.4. DHvA effect in 2DESs

Having introduced the dHvA effect for an arbitrary Fermi surface of a 3DES, we now turn to the special case of 2DESs. The 2DESs investigated in this work are realized at the interface of MgZnO/ZnO heterostructures. In the following we assume that the growth direction and thus the sample normal points along the  $z$ -axis such that the electrons are quasi-free to move in the  $(x, y)$ -plane of the interface. The confinement potential results in a quantization of the energy levels into subbands along the  $z$ -direction. It was shown in Ref. [Tsu07], that the energy separations between the two lowest subbands are very large compared to the Fermi energy. Owing to the large energy separation we can assume that only the lowest subband of energy  $E_{0,z}$  is occupied at low temperatures. The dispersion with  $k_z$  can hence be disregarded from now on. Of course this consideration simplifies the discussion of the dHvA effect compared to the 3D case significantly. The zero-field density of states is therefore given by

$$D(E) = \begin{cases} 0 & \forall E < E_{0,z} \\ \frac{m^*}{\pi\hbar^2} & \forall E \geq E_{0,z} \end{cases} \quad (2.36)$$

Further, for MgZnO/ZnO heterostructures an isotropic conduction band valley centered at the  $\Gamma$  point was reported [Tsu07]. The effective mass  $m^*$  amounts to  $0.31 \pm 0.01 m_e$  as determined from temperature dependent measurements in this work (see Chapter 7). The band structure Landé factor of ZnO is given by  $g = 1.93$  [Tam08].

In the presence of a magnetic field, which yields a component  $B_{\perp}$  perpendicular to the plane of the 2DES, the energy levels are quantized as introduced in Eq. 2.23. Instead of tubes, the energy levels follow circles in 2D. Regarding the MgZnO/ZnO based 2DES we can estimate the Landau splitting  $\hbar\omega_c$ . It scales with  $\hbar\omega_c = 0.37 \text{ meV} \cdot B_{\perp}$ . Please note, that the cyclotron frequency  $\omega_c$  depends on the magnetic field component perpendicular to the 2DES  $\omega_c = \frac{eB_{\perp}}{m^*}$ . Likewise, the Landau splitting is also dependent on  $B_{\perp}$ .

The external field interacts also with the spin degree of freedom of the charge carriers, which has not been considered so far. This effect is taken into account by the Zeeman interaction given by  $E_{\sigma} = \frac{1}{2} \sigma g \mu_B B$  with the spin projection  $\sigma = +1$  for spin up ( $\uparrow$ ) and  $\sigma = -1$  for spin down ( $\downarrow$ ). It lifts the spin degeneracy of the electrons in the 2DES. In MgZnO/ZnO, the

Zeeman splitting scales with  $E_\sigma = 0.11 \text{ meV} \cdot B$  for non-interacting electrons. It is thus on the same order of magnitude as the Landau splitting in the given MgZnO/ZnO 2DES. Note that  $E_\sigma$  depends on the total magnetic field. Taking the spin degree of freedom into account the energy spectrum of a 2DES (non-interacting electrons) in an applied magnetic field  $B$  derived from Eq. 2.23 can be expressed as:

$$E_{j,\sigma} = E_j + E_\sigma = E_{0,z} + \left(j + \frac{1}{2}\right) \hbar\omega_c + \frac{1}{2}\sigma g\mu_B B. \quad (2.37)$$

Due to the limited number of electrons, not all energy levels are occupied. The filling factor  $\nu$  defines the number of occupied energy levels. It depends on the electron density  $n_s$  and the degeneracy  $N_\nu$  defined in Eq. 2.24 at  $g_s = 1$  and can be expressed as

$$\nu = \frac{n_s}{N_\nu} = \frac{\hbar n_s}{eB_\perp}. \quad (2.38)$$

In order to discuss and quantitatively analyze the dHvA effect in a 2DES we apply numerical model calculations following Refs. [Sch02, Wil08, Wil04a]. The starting point of the calculation is the free energy  $F$  which enables us to derive  $M$  according to Eq. 2.17. Thereby we assume that the particle number  $N$  remains constant, which is realistic for a non-contacted 2DES. In the following an idealized 2DES at  $T = 0$  will be discussed before we approach a more realistic situation including finite temperature, disorder and finally electron-electron interactions.

## Ideal 2DES

Considering an ideal 2DES at  $T = 0$  the energy spectrum is composed of discrete energy levels  $E_{j,\sigma}$  and the corresponding DOS is a series of delta peaks given by

$$D(E) = N_\nu \sum_{j=0}^{\infty} \delta(E - E_{j,\sigma}). \quad (2.39)$$

## 2.2. Equilibrium magnetization phenomena: De Haas-van Alphen effect

The chemical potential  $\chi$  and the free energy can then be determined in a self consistent way from the number of electrons  $N = \mathcal{A}n_s$  per area  $\mathcal{A}$  via

$$N = \mathcal{A} \int_0^\chi D(E) dE, \quad (2.40)$$

$$F_{T=0} = U = \int_0^\chi ED(E) dE. \quad (2.41)$$

Using  $M = -\partial F / \partial B|_{T, n_s}$  from Eq. 2.17 we calculate the magnetization of an ideal 2DES. This allows us to model the evolution of  $\chi$  and  $M$  as a function of  $B_\perp$  as shown in Fig. 2.5 (a) and (b) (solid line), respectively.  $M$  is presented in units of the effective Bohr magneton  $\mu_B^* = \mu_B (m_e/m^*)$ . For an ideal 2DES at  $T = 0$  K  $\chi$  jumps discontinuously between two adjacent energy levels at integer  $\nu$ . The periodicity of the oscillations in the reciprocal field is directly related to the carrier density  $n_s$  by

$$\Delta \left( \frac{1}{B_\perp} \right) = \frac{e}{\hbar n_s}. \quad (2.42)$$

So the carrier density can be measured from the oscillation period  $\Delta \left( \frac{1}{B_\perp} \right)$ . The amplitude of the oscillations in  $\chi$  corresponds to the energy gap  $\Delta E$  between the spin-split LLs. Thus this energy gap reflects directly the discrete energy spectrum of the 2DES.

Let us consider the magnitude of  $\Delta E$  separately for even and odd  $\nu$  for small Zeeman splitting  $g\mu_B B < \hbar\omega_c$ :

- At even  $\nu$  spin polarization is not relevant. The energy gap is reduced by the spin splitting. From Eq. 2.37 we can infer that  $\Delta E_L = E_{j+1, \downarrow} - E_{j, \uparrow} = \hbar\omega_c - g\mu_B B$ . We will refer to the energy gap at even  $\nu$  as Landau gaps in the following.
- At odd  $\nu$  spin polarization is present in the 2DES. The degree depends on  $\nu$ . The energy gap is given by  $\Delta E_Z = E_{j, \uparrow} - E_{j, \downarrow} = g\mu_B B$ , which we denote the Zeeman gap.

Please notice, that the above considerations are strictly only true as long as spin splitting is smaller than the Landau splitting  $g\mu_B B < \hbar\omega_c$ . In our experiments on the MgZnO/ZnO based 2DES, this condition is always fulfilled as will be detailed in Sec. 7.3.3.

Via Maxwell's relation introduced in Eq. 2.18 the jumps in the chemical potential in Fig. 2.5 (a) are directly related to the jumps in the magnetization shown in Fig. 2.5 (b) or vice versa. For an ideal 2DES the relation can be simplified [Wie97] to give

$$\frac{\Delta M}{N} = \frac{\Delta \chi}{B}. \quad (2.43)$$

### Real 2DES

In analogy to the 3D case, we have to take finite temperature effects and residual sample disorder into account to provide a more realistic scenario of the real 2DES.

- Level broadening

Disorder and scattering effects result primarily from electron-impurity scattering at low  $T$  [Ush09] and lead to a broadening of the delta-shaped energy levels. The deviation of the DOS from the ideal behavior provides thus important information about the sample disorder and the equilibrium ground state properties of the 2DES. Several phenomenological approaches have been proposed to model the DOS [Wil08, Ush09] in 2DESs, but no comprehensive microscopic theory has been presented yet. Following Refs. [Sch02, Wil04a, Zhu03, Wil08] we employ model calculations assuming Gaussian broadened LLs. Along this line the DOS can be written as

$$D(E) = \frac{eB_{\perp}}{h} \sum_{j=0}^{\infty} \frac{1}{\sqrt{2\pi}\Lambda} \exp\left[-\frac{(E - E_{j,\sigma})^2}{2\Lambda^2}\right] \quad (2.44)$$

where  $\Lambda$  denotes the broadening parameter. Ando and Uemura [And74b] derived an analytical expression for  $\Lambda$  assuming short range scattering. It is given by  $\Lambda = \frac{e\hbar}{m^*} \sqrt{2/\pi} \mu \sqrt{B_{\perp}}$ . Inserting  $\mu = 3.8 \times 10^5 \text{ cm}^2/\text{Vs}$  (sample zn0259, c.f. Sec. 4.3) we obtain  $\Lambda = 5 \times 10^{-2} \sqrt{B_{\perp}} \text{ meV} T^{-1/2}$ . Figure 2.5 (a) displays a gray scale plot of the corresponding DOS for a 2DES in MgZnO/ZnO with  $n_s = 1.7 \times 10^{11} \text{ cm}^{-2}$  as a function of  $B_{\perp}$ . Dark (white) color



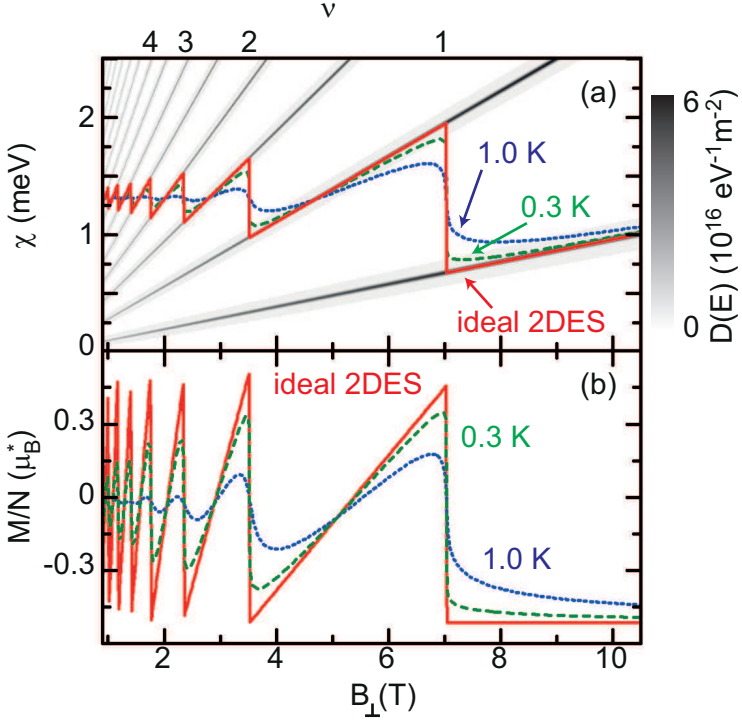


**Figure 2.5.:** (a) Calculated DOS (gray scale plot) for a 2DES in MgZnO/ZnO with  $n_s = 1.7 \times 10^{11} \text{ cm}^{-2}$  and Gaussian broadened energy levels. The broadening parameter  $\Lambda$  is given by  $0.05 \times \sqrt{B} \text{ meV}/\sqrt{\text{T}}$ . Dark (white) color corresponds to a high (low) value of the DOS. The evolution of the chemical potential  $\chi$  is shown for an ideal 2DES at  $T = 0$  (solid line) and for a real 2DES at  $T = 0.3$  K (dashed line) and at  $T = 1.0$  K (dotted line), respectively. Note that the spin splitting is included in the calculations. (b) Corresponding magnetization  $M$  of the 2DES. For an ideal 2DES the predicted sawtooth is recovered. In reality, finite temperature and disorder reduce the dHvA amplitudes.

corresponds to a high (low) value of the DOS.

- Finite temperature

Finite temperature effects become important in a real 2DES. The occupation of the states in equilibrium at temperature  $T$  is governed by the Fermi distribution

$$\mathcal{F}(E, \chi, T) = \left[ 1 + \exp\left(\frac{E - \chi}{k_B T}\right) \right]^{-1}. \quad (2.45)$$

In accordance to the ideal 2DES, we can determine  $\chi$  and  $F$  self consistently by solving

$$N = \mathcal{A} \int \mathcal{F}(E, \chi, T) D(E) dE, \quad (2.46)$$

$$F = \chi N - k_B T \mathcal{A} \int D(E) \ln \left[ 1 + \exp\left(\frac{\chi - E}{k_B T}\right) \right] dE. \quad (2.47)$$

The chemical potential and the corresponding magnetization at  $T = 0.3$  K (dashed line) and  $T = 1.0$  K (dotted line) taking Gaussian level broadening into account are shown in Fig. 2.5 (a) and (b), respectively. Compared to the ideal 2DES, the discontinuities in  $\chi$  and  $M$  are smoothed out. Further, the oscillation amplitudes and thus the single-particle energy gaps are reduced.

When the level broadening is small compared to the energy gaps, Eq. 2.43 is nonetheless a good approximation to determine the oscillation amplitudes of  $\chi$  from the peak-to-peak dHvA amplitudes  $\Delta M$ . They are a manifestation of the energy spectrum with energy gaps  $\Delta E$  and the underlying DOS of the 2DES. In this work we will refer to them as thermodynamic energy gaps  $\Delta E$  which are determined via

$$\Delta E = \frac{\Delta M B}{N} \quad (2.48)$$

They directly reflect the ground state energy spectrum of the 2DES.

### Many-body effects in 2DES: Exchange interaction

So-called many-body effects are present in a 2DES if the electrons do not behave independently of each other. The dimensionless Wigner-Seitz parameter  $r_s$  is an important parameter to estimate the relevance of many-body effects. It is given by [Ful12]

$$r_s = \frac{1}{a_B^* \sqrt{\pi n_s}}, \quad (2.49)$$

where  $a_B^* = 4\pi\epsilon_0\epsilon_r\hbar^2/m^*e^2$  denotes the effective Bohr radius. For ZnO, the dielectric constant  $\epsilon_r$  amounts to 8.5 [Tsu08]. Inserting  $m^* = 0.31 m_e$  and  $n_s = 1.7 \cdot 10^{11} \text{ cm}^{-2}$  (c.f. sample *zn0259*) we obtain the effective Bohr radius  $a_B^* = 14.5 \text{ \AA}$  and  $r_s = 9.0$ . For comparison, a non-interacting electron system usually yields  $r_s \lesssim 2$ , e.g.  $r_s \approx 0.5$  in GaAs based 2DESs [Tsu08]. The large  $r_s$ -parameter thus indicates, that electron-electron interactions play an important role in the MgZnO/ZnO 2DES.

It is well known that in high magnetic fields electron-electron interaction effects can enhance the dHvA amplitude  $\Delta M$  over the value predicted in the single particle picture [Jan69, Mac86, And74a]. This phenomenon has been observed in many different experiments [Eng82, Nic88, Wie97, Mei01].

A well established tool to describe many-body interactions theoretically is the Hartree-Fock approximation (HFA). It considers the so-called exchange interaction effects. These are interaction effects that can be well described by a mean field theory. However, the HFA neglects contributions that go beyond a simple mean field approach. Those contributions are usually referred to as correlation effects. Correlation effects can be only included by perturbations to the SE. A quantitative treatment of the correlation effects will not be discussed here.

In the following we consider the exchange interaction. Physically, the exchange interaction is a consequence of the Pauli exclusion principle. The average spatial separation between electrons of the same spin direction is larger compared to one of electrons with opposite spins. In view of the Coulomb repulsion, the first situation is energetically favorable. This leads to a renormalization of the energy gap between spin-up and spin-down states whenever the population of the two spin split levels is not balanced. This provokes (partial) spin polarization. In addition, the change of the

## 2. Fundamental theoretical concepts

---

relative occupation of the two spin states by changing the magnetic field induces an oscillatory variation of the energy gap between the different spin states [And74a].

We will briefly outline the major results of the HFA in the following. Detailed reviews can be found in Refs. [And74a, Mac86, Man97, Mei01]. In the HFA the exchange interaction is given by

$$E_{j,\sigma}^{(\text{int})} = -\frac{e^2}{4\pi\epsilon_0\epsilon_r l_B} \sum_{j'} c_{j,j'} (\nu_{j',\uparrow} - \nu_{j',\downarrow}). \quad (2.50)$$

The term  $(\nu_{j',\uparrow} - \nu_{j',\downarrow})$  denotes the partial filling factor and the coefficients  $c_{j,j'}$  are the Fourier transformations of the integrated matrix elements of the Coulomb potential [Mac86, Mei01, Man95]. For low lying LLs the values for  $c_{j,j'}$  are calculated in Ref. [Mac86]. At  $T = 0$  the internal energy  $U$  is obtained by a summation over single particle energies and exchange interaction terms

$$U = \frac{N}{\nu} \sum_{j,\sigma} (\nu_{j,\uparrow} - \nu_{j,\downarrow}) \left( E_{j,\sigma} + E_{j,\sigma}^{(\text{int})} \right). \quad (2.51)$$

This approach was first used by MacDonald *et al.* [Mac86] to calculate the chemical potential and the magnetization of an interacting 2DES. The authors pointed out that the Maxwell equation derived in Eq. 2.18 still holds true in the framework of the HFA. Therefore the discontinuity in  $\chi$  is still directly related to the one in  $M$ . Along this line they predicted significant enhancements of the energy gaps at even and odd filling factors.

It was found theoretically and was also substantiated in experiments that the exchange enhancement is especially pronounced at odd filling factors, where spin splitting occurs. This enhancement is often described in terms of the enhanced effective Landé factor  $g^*$  [And74a]. In the HFA the Zeeman gap  $\Delta E_Z$  is expressed as

$$\Delta E_Z = |g| \mu_B B + \frac{e^2}{4\pi\epsilon_0\epsilon_r l_B} \sum_{j'} c_{j,j'} (\nu_{j',\uparrow} - \nu_{j',\downarrow}) = g^* \mu_B B. \quad (2.52)$$

Fully self consistent model calculations of the magnetization properties of a MgZnO/ZnO 2DES using a HFA approach are beyond the scope of this

thesis. In the analysis of the experimental data in Chapter 7 we therefore refrain ourselves to a phenomenological description of the exchange enhancement using the methodology of the enhanced effective  $g^*$  factor.

In conclusion, the dHvA effect monitors the groundstate thermodynamic properties. The Zeeman and the Landau splitting are directly reflected by the dHvA amplitudes. In addition, many-body interactions are included in the quantum oscillatory magnetization of a 2DES. Thereby important information about the interactions in the 2DES and the underlying DOS can be gained.

## 2.3. Non-equilibrium induced currents

The dHvA effect introduced above is an equilibrium phenomenon and well related to other thermodynamic equilibrium quantities. Besides, 2DESs exposed to high magnetic fields exhibit further effects. The most prominent example is the quantum Hall effect (QHE) discovered in 1980 [Kli80]. It is characterized by a Hall resistance exhibiting plateaus at integer filling factors. The plateaus are quantized in units of  $h/e^2$ . In addition, the longitudinal resistance vanishes at integer filling factors at low temperatures. In this regime the currents are assumed to flow dissipationless in quasi-one dimensional edge channels.

Non-equilibrium currents (NECs) have been observed near integer filling factors in the QHE regime. They are a manifestation of the QHE and can be measured in a contact free configuration exploiting the induced magnetic moment. This will be detailed in the following where we revisit the phenomenology of NECs. After that the so-called charge redistribution model will be introduced. The model is helpful to explain the temperature dependent properties of the NECs.

### 2.3.1. Phenomenology

The situation of a 2DES exposed to an external magnetic field is schematically depicted in Fig. 2.6. A sweeping magnetic field  $\frac{\partial B}{\partial t}$  induces an electromotive force  $\varepsilon$  around the perimeter of the sample. As a result, a current  $I$  is induced which circulates around the sample enclosing the area  $A$ . The current is usually referred to as a non-equilibrium current

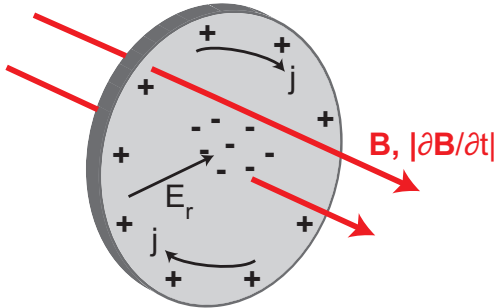


**Figure 2.6.:** Schematic sketch of non-equilibrium currents (NECs) in a disc-shaped 2DES induced by a time varying magnetic field  $\partial B/\partial t$  in the QHE regime. The current  $\mathbf{j}$  flows around the perimeter of the sample. Due to the Lorentz force the charge carriers are redistributed as indicated. A radial Hall electric field  $E_r$  builds up which is perpendicular to the induced current.

(NEC). Obviously, a magnetic moment  $M = IA$  follows from a NEC. Away from integer filling factors, the currents dissipate very rapidly due to the residual resistivity of the 2DES. Near integer filling factors and at sufficiently low temperature, the resistivity vanishes in the QHE regime such that NECs percolate quasi-dissipationless. In this regime the associated magnetic moment has been detected. The direction of the currents and thereby the direction of the associated magnetic moment changes polarity upon changing the sweep direction. For this reason the non-equilibrium magnetization signal is easily distinguished from the dHvA effect, which does not depend on the direction of the magnetic field sweep. As a further consequence of the magnetic field, the charge carriers of the induced current are subject to the Lorentz force. The charge carriers are redistributed from the edge to the center of the 2DES or vice versa as indicated in Fig. 2.6. This results in a radial Hall electric field  $E_r$ . Note, that NECs can also be induced by varying the carrier density rather than the magnetic field [Ruh09, Fau05], but this will not be employed in this thesis.

### 2.3.2. Charge redistribution model

In this section the charge redistribution model will be briefly outlined. It is helpful to understand basic properties of the NECs which includes their

temperature dependence as well as asymmetries in the NECs between different sweep directions. A detailed derivation is given in Refs. [Mat04a, Kav05, Ush09, Dya91].

We assume a disc-shaped 2DES which is subject to a time varying magnetic field as depicted in Fig. 2.6. The magnetic moment  $M$  is induced by the tangentially circulating current distribution  $j_\phi(r)$ . In the QHE regime the Hall angle is  $90^\circ$  and hence  $j_\phi(r) = \sigma_{xy} E_r$ , where  $\sigma_{xy}$  denotes the transversal conductivity. Thus  $M$  is given by

$$M = \pi \int_0^R j_\phi(r) r^2 dr = \pi \int_0^R \sigma_{xy} E_r(r) r^2 dr. \quad (2.53)$$

We pointed out above that charges in the 2DES are redistributed in presence of a sweeping magnetic field. However, they do not solely accumulate at the edge but they are distributed over the disc [Dya91]. In some regions of the 2DES there is an additional electron density  $\Delta n$  which raises the chemical potential above its equilibrium value. In other sample regions the electron density is depleted by  $\Delta n$  causing a decrease of the local chemical potential. This scenario is schematically depicted in Fig. 2.7. As a first approximation, the authors of Refs. [Mat04a, Kav05, Ush09] assumed a uniform excess charge density  $+e\Delta n$  for  $r < R/\sqrt{2}$  and a uniform charge depletion  $-e\Delta n$  for  $R/\sqrt{2} \leq r \leq R$ . Using this charge distribution the Hall electric field  $E_r$  is calculated and inserted into Eq. 2.53 to give

$$M = \text{const} \times \sigma_{xy} \Delta n(T) R^3. \quad (2.54)$$

From this outcome we conclude that  $M$  exhibits the same temperature dependence as  $\Delta n$ .

Regarding  $\Delta n$  the following functional form was found [Ush09, Kav05]:

$$\Delta n = \int_{E_0/2}^{E_0/2 + k_B T \ln C} D(E) dE \quad (2.55)$$

where  $C$  is a constant smaller than unity and  $E_0$  is the energy of the equilibrium position of  $\chi$  as defined in Fig. 2.7. The temperature dependence of  $\Delta n$  is therefore governed by the form of the DOS in the localized-state region between the highest occupied and the lowest unoccupied LL.

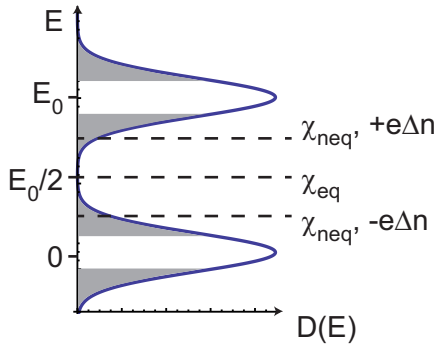


**Figure 2.7.:** DOS of a real 2DES. Disorder broadened LLs with localized (shaded region) and extended (unshaded region) states. The position of the chemical potential  $\chi_{\text{eq}}$  in equilibrium at integer  $\nu$  is indicated. In a non-equilibrium situation, charges accumulate in or deplete from different regions within the 2DES. In regions of accumulation ( $+e\Delta n$ ) the chemical potential  $\chi_{\text{neq}}$  increases, in regions of depletion ( $-e\Delta n$ ) it decreases locally (after Ref. [Ush09]).



### 3. Micromechanical cantilever magnetometer

A variety of methods are available for magnetization measurements. However, if high sensitivity in combination with low measurement temperatures are desired, superconducting quantum interference device (SQUID) magnetometers or torque magnetometers are commonly used [Wil10]. The performance of commercial SQUID magnetometers is typically very good at low magnetic fields where a magnetic moment sensitivity of  $\sim 10^{-10}$  J/T [Stö83] is reached. The dHvA effect in 2DESs was first observed with SQUID magnetometers [Stö83]. Later, Meinel *et al.* [Mei97] developed a more sophisticated ac SQUID technique reaching a magnetic moment sensitivity of  $\sim 10^{-14}$  J/T at 10 T. This allowed them to investigate the fractional QHE in the magnetization of a 2DES [Mei99]. However, the performance of a SQUID magnetometer is usually severely degraded in high magnetic fields. The detection of magnetic quantum oscillations, at the same time, relies on the application of high magnetic fields. Only at relatively high magnetic fields, the Landau level separation is large enough to be traced in a typical dHvA experiment. Therefore, torque magnetometers became the tool of choice to study magnetization phenomena at high magnetic fields requiring high magnetic moment sensitivity.

Torque magnetometers divide into two categories, torsion balance magnetometers and cantilever magnetometers. Many concepts of the former have been proposed so far [Eis85b, Haa84, Eis85a, Tem88, Wie98, Mat04b]. Its working principle is as follows. A sample is attached to a wire or a fiber and subject to a magnetic field. If the sample exhibits a non-vanishing magnetic moment, it exerts a torque being proportional to the magnetic moment. In consequence, the torque twists the wire or fiber. The sensitivity relies on the torsional modulus of the used wire. Indeed, the first measurement of the dHvA effect in metals in 1930 [Haa30] was carried out by a torsion balance magnetometer.

The alternative approach is the use of cantilever magnetometers, which

has been applied throughout this thesis. Its working principle as well as the respective readout scheme will be introduced in the following. Further the experimental setup will be described and the sensitivity of the magnetometer will be discussed.

## 3.1. Principle of operation

The working principle of a micromechanical cantilever magnetometer (MCM) is depicted in Fig. 3.1. The sample is attached to the free end of a flexible, singly clamped beam or paddle. In a uniform magnetic field  $\mathbf{B}$  a torque  $\Gamma$  acts on the magnetic moment  $\mathbf{M}^1$  of the sample. It is given by

$$\Gamma = \mathbf{M} \times \mathbf{B}. \quad (3.1)$$

The torque deflects the free end of the cantilever beam by an angle  $\eta$  away from its equilibrium position. In our considerations we neglect magnetic field gradients which would induce an additional force  $F = \nabla(\mathbf{M} \cdot \mathbf{B})$  onto the cantilever. The high field homogeneity of our magnets (c.f. Sec. 3.3) justifies this assumption.

A key ingredient for the measurement technique to work is that the sample exhibits an anisotropic magnetic moment  $\mathbf{M}$ , which has to be tilted with respect to  $\mathbf{B}$ , i.e.  $\mathbf{M} \nparallel \mathbf{B}$ . Otherwise  $\Gamma$  in Eq. 3.1 vanishes. We will briefly discuss this implication for the materials and physics discussed in the course of this thesis.

- MnSi thin films

MnSi thin films, which are expected to be paramagnetic or ferromagnetic at low temperatures, possess an intrinsic anisotropy as discussed in Sec. 2.1. Thus, on the one hand the requirement of an anisotropic moment  $\mathbf{M}$  is usually fulfilled. On the other hand, however, the interpretation of the torque signal is not always straightforward, because the exact orientation of  $\mathbf{M}$  is usually unknown.

- dHvA effect in 3DESs

For the investigation of the quantum oscillatory magnetization via

---

<sup>1</sup>Please note that we often refer to  $\mathbf{M}$  as the magnetization instead of magnetic moment. Since we usually know the volume  $V$  (or the area  $\mathcal{A}$ ) of the electron system, these two terms are interchangeable.

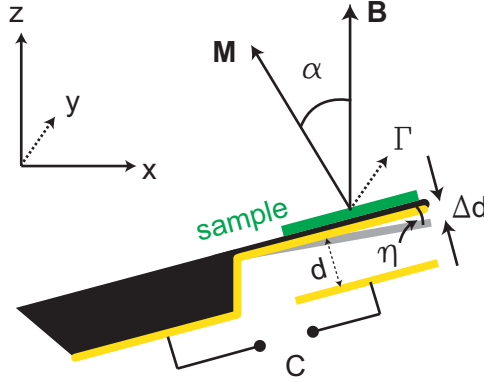


**Figure 3.1.:** Schematic side view of a cantilever magnetometer. A torque  $\Gamma = \mathbf{M} \times \mathbf{B}$  is exerted onto the free-standing cantilever paddle which is deflected by  $\Delta d$ . In the capacitive readout scheme the deflection is monitored by a capacitance change.

torque magnetometry we also rely on the anisotropy of the oscillatory magnetic moment. In Eq. 2.29 an expression for the oscillatory magnetization components  $M_{\parallel}$  and  $M_{\perp}$  was derived. In combination with Eq. 3.1 the oscillatory torque yields:

$$\Gamma = M_{\perp} B = -\frac{1}{f} \frac{\partial f}{\partial \theta} M_{\parallel} B \quad (3.2)$$

Thus, an anisotropic Fermi surface, i.e.  $\frac{\partial f}{\partial \theta} \neq 0$ , is required, otherwise the torque vanishes. For instance, when we regarded a hypothetical ideal 3D electron gas with a spherical Fermi surface the torque signal was argued to be zero.

- dHvA effect and NECs in 2DESs

In 2DES, the Fermi surface is naturally anisotropic, because it is confined to two dimensions. In other words, the orbital motion of the electrons is restricted to the two-dimensional electron system. Thus, the resulting orbital moment  $\mathbf{M}$  is perpendicular to the 2DES

plane. In order to observe a torque, the 2DES normal has to be tilted by an angle  $\alpha$  with respect to the direction of the magnetic field. For known  $\alpha$ , the magnetic moment can be inferred straightforward from the torque signal via

$$|\mathbf{M}| = \frac{\Gamma}{B \sin \alpha}. \quad (3.3)$$

Owing to this relation cantilever magnetometry allows to directly determine the orbital magnetic moment in 2DESs. The same consideration holds true for NECs. As discussed in Sec. 2.3, NECs induce an orbital moment which is perpendicular to the 2DES plane.

In addition to the bending of the cantilever beam as depicted in Fig. 3.1, torsion of the cantilever beam is in principle also possible according to Eq. 3.1. Without any loss of generality, we set  $\mathbf{B} = (0, 0, B)$  in the following considerations. Then, if  $M_y \neq 0$ , the  $x$ -component of the torque does not vanish. Consequently, the MCM beam would experience a torsional moment. The torsional modulus  $G$  of the cantilever beam, which determines the torsional deflection, is, however, typically smaller than the Young's modulus  $Y$  of the spring, which governs the bending of the beam (e.g. for GaAs  $Y = 8.3 \times 10^{10}$  N/m<sup>2</sup> and  $G = 3.2 \times 10^{10}$  N/m<sup>2</sup> [Gar62]). Moreover, torsional deflections are suppressed in the experiment by the application of MCMs with two beams as detailed in Sec. 3.3. Therefore, we neglect torsional moments and consider only deflections of the cantilever as indicated in Fig. 3.1.

For small deflection angles  $\eta$  Hook's law holds true and we can rewrite Eq. 3.1 by

$$\Gamma = k\eta = k \frac{\Delta d}{L}, \quad (3.4)$$

where  $k$  denotes the spring constant and  $L$  the length of the cantilever beam. The deflection of the cantilever  $\Delta d$  is thus proportional to the exerted torque  $\Gamma$ .

## 3.2. Capacitive readout

The deflection of the cantilever in response to a torque can be measured by various methods. A well established technique is the fiber optical readout

of the MCM deflection detailed in Ref. [Spr06]. Here, a glass fiber is positioned close to the cantilever surface and the deflection of the cantilever beam can be detected via a Fabry-Perot type interference pattern. Further, methods relying on piezo-resistive MCMs [Wi198] or on a resonant readout scheme [Har99] were applied. For the data reported in this thesis we use the capacitive readout scheme. It is advantageous compared to other techniques because the wiring is easily integrated into an existing cryostat and it can be used with any MCM design.

The working principle is schematically depicted in Fig. 3.1. In case of a non-metallic MCM, its backside has to be metalized. This step can obviously be omitted for a MCM made of a conducting material. In combination with a counter electrode placed on the substrate the beam forms a plate capacitor. In equilibrium, the capacitance  $C_0$  is given by

$$C_0 = \frac{\epsilon_0 A}{d}, \quad (3.5)$$

where  $A$  denotes the area of the electrodes and  $d$  is the distance between the electrodes which are assumed to be parallel. A cantilever deflection  $\Delta d$  causes a change in the capacitance. For small deflections  $\frac{\Delta d}{d} \ll 1$  we can write

$$C(d + \Delta d) = \frac{\epsilon_0 A}{d + \Delta d} = \frac{\epsilon_0 A}{d} \left(1 + \frac{\Delta d}{d}\right)^{-1} \quad (3.6)$$

$$\approx C_0 \left(1 - \frac{\Delta d}{d} + \dots\right). \quad (3.7)$$

Thus the capacitance change  $\Delta C$  is proportional to the deflection  $\Delta d$ . Taking Eq. 3.4 into consideration we find that the relation between torque and capacitance change is linear:

$$\Gamma = K \Delta C \quad (3.8)$$

Here,  $K$  denotes a constant of proportionality which is determined via an *in situ* calibration of the MCM. Throughout this thesis an electrostatic calibration routine was used [Sch00]. A dc voltage  $U$  was applied between the cantilever and the ground plane. The resulting attractive force between

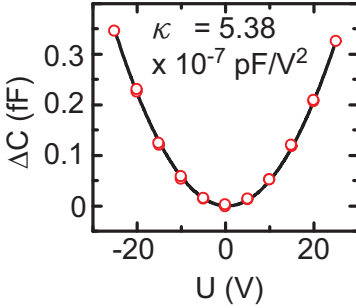


**Figure 3.2.:** Electrostatic calibration of a CuBe based MCM.  $\Delta C$  as a function of applied dc voltage  $U$  (datapoints). A quadratic fit (line) yields  $\kappa$ .

the capacitor plates is expressed as

$$|F| = \frac{CU^2}{2d}. \quad (3.9)$$

The effective torque introduced by the electrostatic force is given by

$$\Gamma = \beta |F| L = \frac{\beta CLU^2}{2d}. \quad (3.10)$$

The factor  $\beta$  characterizes the reduced mechanical response of a cantilever to a force applied to the end of the beam as compared to a torque [Sch00, Tim72, Wil04a]. It depends on the cantilever material as well as its dimensions. In this work we designed and used two different MCMs, which will be introduced in Sec. 3.3. For MCMs based on GaAs  $\beta$  amounts to  $\sim 0.73$ , for CuBe based MCMs  $\beta \approx 1$ . Combining Eq. 3.8 and Eq. 3.10 we obtain

$$\Delta C = \kappa U^2 \quad \text{with} \quad \kappa = \frac{\beta C_0 L}{2dK}. \quad (3.11)$$

Here,  $C_0$  is the capacitance at zero applied voltage. Measuring the capacitance as a function of applied voltage allows to determine  $\kappa$ . A calibration curve of a CuBe based MCM (see Sec. 3.4) is shown in Fig. 3.2.  $\kappa$  is obtained from a quadratic fit routine. Replacing  $d$  in Eq. 3.11 we express  $K$  as

$$K = \frac{\beta C_0^2 L}{2\epsilon_0 A \kappa}. \quad (3.12)$$

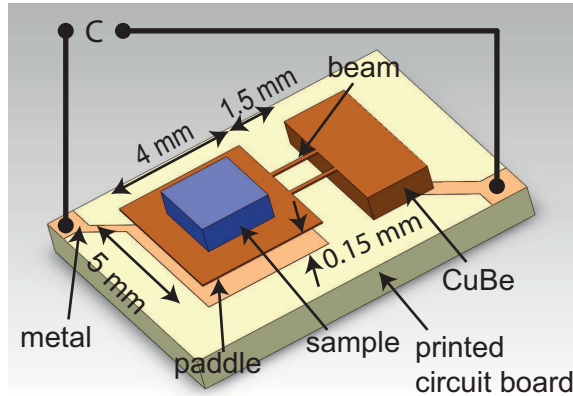


**Figure 3.3.:** Sketch of a CuBe based sensor machined out of a  $50\ \mu\text{m}$  thick CuBe foil. The dimensions of the cantilever paddle are  $4 \times 5\ \text{mm}^2$  and the length of the beam is given by  $1.5\ \text{mm}$ .

### 3.3. Experimental setup

For the experiments conducted in this work two types of MCMs were used. They either consisted of copper beryllium (CuBe) or of gallium arsenide (GaAs). Therefore we refer to them as CuBe or GaAs based MCMs in the following. The usage of different cantilever materials and designs became necessary because the experiments required different sensitivities. This will be discussed in Sec. 3.4.

Figure 3.3 depicts the design of the MCMs based on CuBe. They were machined out of a  $50\ \mu\text{m}$  thick CuBe foil [Chr94] which defined the thickness of cantilever beam and paddle. The dimensions of the cantilever paddle, which accommodated the sample, were  $4 \times 5\ \text{mm}^2$ . The MCM consisted of two beams. This feature increased its stability and helped to prevent torsion of the cantilever paddle. Their lengths were given by  $1.5\ \text{mm}$  and they were  $200\ \mu\text{m}$  wide. The gap between the counter electrode and the cantilever paddle was set to  $d \approx 150\ \mu\text{m}$ . The MCM was attached to a printed circuit board, which provided the adequate electrode design.

The schematics of GaAs based MCMs are sketched in Fig. 3.4. Length and width of the MCM paddle were given by  $1.2\ \text{mm}$  and  $2.0\ \text{mm}$ , respectively. The beam length was  $1\ \text{mm}$  and its width yielded  $150\ \mu\text{m}$ .  $d$

amounted to  $\sim 150 \mu\text{m}$ . The thickness of the beam and paddle was set to  $\sim 4.5 \mu\text{m}$ . Such a small, well-defined thickness was achieved by using specially designed GaAs heterostructures and optimized etching techniques (c.f. Chapter 4). The cantilever was attached to a sapphire substrate. Comparing both cantilever designs, the CuBe based MCMs are quite robust and can accommodate rather large and heavy samples. In contrast, GaAs based MCMs are fragile and require thin and light samples. For the experiment, both MCMs were contacted with coaxial cables providing accurate shielding. A highly-sensitive capacitance bridge<sup>1</sup> was used to measure the capacitance via a three-terminal method.

The MCMs were mounted into a  $^3\text{He}$  cryostat reaching temperatures down to  $\sim 0.27 \text{ K}$ . They allowed a precise temperature control in the regime  $0.27 \text{ K} \leq T \lesssim 60 \text{ K}$ .

The magnetic field was provided by superconducting magnet systems. Two magnet systems have been used throughout this thesis. First, an axial magnet providing fields up to 14.5 T with a relative homogeneity better than  $10^{-4}$  in a spherical volume of  $1 \text{ cm}^3$  around the field center was used. Second, a vector magnet system<sup>2</sup> was set up and used in the framework of this work. It provided fields up to 9 T along the axial direction and a maximum rotatable field of 4.5 T. Its field homogeneity was specified to be better than  $10^{-3}$  in a spherical volume of  $1 \text{ cm}^3$  around the field center.

## 3.4. Sensitivity

In this section we discuss the choice and design of the MCM for our experiments, which depended in particular on the physics of the material to be investigated. In the course of this thesis three different material systems were studied: MnSi thin films, CrB<sub>2</sub> bulk crystals and MgZnO/ZnO heterostructures. Regarding MnSi thin films the focus of the discussion was its magnetic phase diagram and anisotropy properties. Concerning the latter material systems we were interested in the quantum oscillatory behavior of the magnetization. The expected signal amplitudes vary significantly between the different material systems as will be estimated in the following.

---

<sup>1</sup>Andeen Hagerling, models AH2500A and AH2700A.

<sup>2</sup>American Magnetics, 9.0 Tesla / 4.5 Tesla 2-Axis, superconducting magnet system.



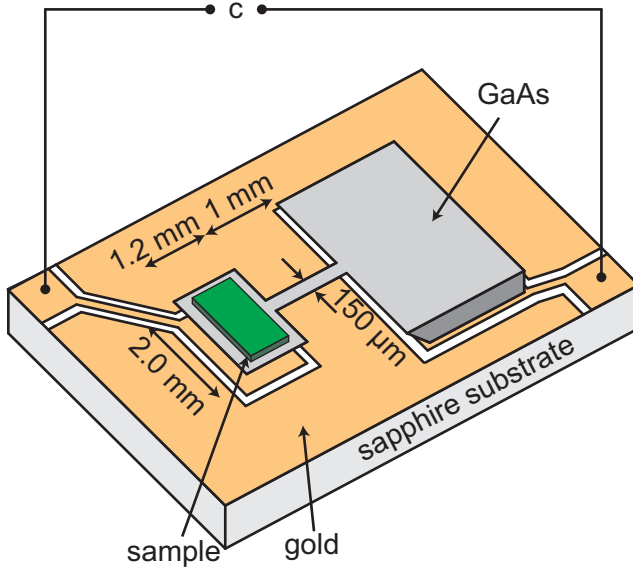


**Figure 3.4.:** Sketch of a GaAs based MCM. The thickness of paddle and beam is  $\sim 4.5 \mu\text{m}$ . The dimensions of the cantilever paddle are  $4 \times 5 \text{ mm}^2$  and the length and width of the beam is given by  $1.5 \text{ mm}$  and  $150 \mu\text{m}$ , respectively.

For ferromagnetic materials the signal strength depends primarily on the magnetic moment per unit cell and the volume of the sample. In MnSi, the magnetic moment per unit cell is given by  $1.68 \mu_B$  [Li13]. Thus, if we assume a film thickness of  $10 \text{ nm}$  and a typical sample area of  $3 \times 3 \text{ mm}^2$  we obtain a maximum signal amplitude on the order of  $\Delta M = 10^{-9} \text{ J/T}$ . Measurements of the dHvA effect represent a considerably larger challenge, especially in the case of a 2DES. The signal amplitude of the dHvA effect depends crucially on the number of free charge carriers. In a 3D metal, there are typically  $10^{20}$  electrons in a volume of  $1 \text{ mm}^3$ . However, as reported in Sec. 2.2, the torque signal, i.e. the amplitude of the quantum oscillatory magnetization, depends in particular on the shape of the Fermi surface. For metals, typical amplitudes of  $\Delta M$  are on the order of  $10^{-9} \text{ J/T}$  at  $B = 1 \text{ T}$  for a sample volume of  $1 \text{ mm}^3$  [Sho84].

### 3. Micromechanical cantilever magnetometer

In a 2DES there are typically  $10^{10}$  electrons per  $\text{mm}^2$ . For an isotropic 2DES the Fermi surface reduces to a circle. As detailed in Sec. 2.2.4 each electron of an ideal 2DES without spin splitting contributes two effective Bohr magnetons  $\mu_B^*$  to the magnetic moment in an applied field at  $T = 0$  K. For a sample with an area of  $1 \text{ mm}^2$  we thus expect a signal amplitude of  $\sim 10^{-13}$  J/T or smaller. Taking these numbers into consideration we designed the MCMs in such a way as to meet these sensitivity requirements. For MnSi thin films and the CrB<sub>2</sub> single crystal we designed and used a MCM as depicted in Fig. 3.3. Experimentally we obtained calibration constants  $K$  on the order of  $\sim 2 \times 10^{-5}$  Nm/pF. For a typical measurement with averaging times of  $\sim 0.4$  s the rms noise of the capacitance bridges yields 5 aF, which results in  $\delta C \approx 4$  aF. Thus the torque resolution  $\delta\Gamma$  is given by  $\delta\Gamma = K\delta C$  and the magnetic moment sensitivity can be expressed as  $\delta M = \frac{\delta\Gamma}{B}$ . At  $B = 10$  T we obtain  $\delta M \sim 1 \times 10^{-11}$  J/T.

The investigation of the dHvA effect in 2DESs required a higher sensitivity. Therefore we chose GaAs based MCMs as shown in Fig. 3.4 to study the 2DES confined in MgZnO/ZnO heterostructures. Here, a magnetic moment sensitivity of  $\delta M \sim 4 \times 10^{-14}$  J/T was achieved experimentally. The sensitivity can of course be further improved by increasing the average time or by software based averaging. An overview of the used MCMs and their respective, experimentally determined sensitivities is given in Table 3.1.

| Sample                         | MnSi                     | CrB <sub>2</sub>         | MgZnO/ZnO                |
|--------------------------------|--------------------------|--------------------------|--------------------------|
| Sensor type                    | CuBe                     | CuBe                     | GaAs                     |
| $K$ (Nm/pF)                    | $2.49 \times 10^{-5}$    | $1.96 \times 10^{-5}$    | $1.07 \times 10^{-7}$    |
| $\delta M$ (J/T) at $B = 10$ T | $\sim 1 \times 10^{-11}$ | $\sim 1 \times 10^{-11}$ | $\sim 4 \times 10^{-14}$ |

**Table 3.1.:** Experimentally determined sensitivities of the MCMs used in this work at  $T \approx 0.28$  K.

## 4. Materials, sample details and preparation

In this chapter we introduce the material systems relevant for this thesis. Three different material systems were investigated: MnSi thin films, CrB<sub>2</sub> single crystals and MgZnO/ZnO heterostructures. In the following, fundamental properties of these materials are reviewed and details of the specific samples used in this work are given. Further, the preparation process of the cantilever sensors is shown in Sec. 4.4.

### 4.1. MnSi thin films

Compounds that crystallize in the B20-type structure have attracted enormous attention during the last years [Müh09, Yu10a, Yu10b, Sek12, Rit13]. Their crystal structure is cubic, but non-centrosymmetric. The type of magnetic order present in these bulk materials is mainly due to the interplay of three contributions to the free energy. Those are ferromagnetic exchange energy, spin orbit coupling and the Dzyaloshinskii-Moriya interaction. The latter is an antisymmetric spin exchange interaction characteristic for the given crystal structure. The combination of these energy terms results in a variety of potential magnetic configurations [Bau12]. The perhaps most intriguing example is the so-called skyrmion phase, which is composed of a regular array of spin vortices with non-zero topological winding number [Müh09]. Further, helical spin structures, conical spin structures as well as field induced collinear spin structures are possible.

Bulk MnSi is the most prominent example of this material class [Müh09, Yu10a, Rit13]. It undergoes a phase transition from a paramagnetic state to a helimagnetic state at  $T_c \approx 29.5$  K. At  $B > B_{c1} \approx 0.1$  T the conical phase appears and at  $B > B_{c2} \approx 0.6$  T the system turns into a field-polarized state. Close to  $T_c$  and at moderate fields  $B \approx 0.4$  T a phase pocket exists that hosts the skyrmion phase as was discovered recently [Müh09, Yu10a].

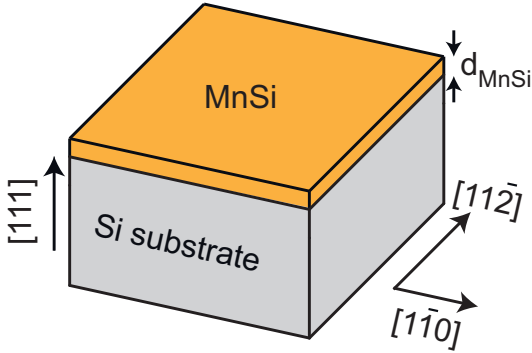


**Figure 4.1.:** Schematic of MnSi thin films grown onto Si (111) substrates.

Apart from being very interesting from a fundamental research viewpoint this material system might also be a promising candidate for spintronic applications since the skyrmion motion can be driven by very low current densities [Jon10, Sch12b]. However, the integration of bulk crystals into state of the art nanometer-scale chip technology might be challenging. Along this line, MnSi in the form of micro- or nanostructures would be more favorable. Therefore, the fabrication of epitaxial thin film MnSi has become interesting and intensive efforts have been dedicated to this goal [Hig09, Kar10, Kar11, Li13].

The samples used in this thesis were fabricated in the group of Prof. Thorsten Hesjedal at the University of Oxford. They used molecular beam epitaxy to grow the MnSi thin films onto Si (111) substrates. Mn, evaporated in an effusion cell, and Si, evaporated by an electron beam, were co-deposited on the Si substrate to form the MnSi thin film. Good crystalline quality of the thin films was established by X-ray diffraction of several reference samples [Wie].

To allow for cantilever magnetometry the samples were cut using a wire-saw and oriented along the  $[11\bar{2}]$ - and the  $[\bar{1}\bar{1}0]$ -direction, respectively, as denoted in Fig. 4.1. Two samples have been investigated in this work. Sample areas along with the respective thickness of the MnSi film  $d_{\text{MnSi}}$  are summarized in Table 4.1.

| Sample        | $d_{\text{MnSi}}$ (nm) | $\mathcal{A}$ (mm <sup>2</sup> ) |
|---------------|------------------------|----------------------------------|
| <i>SI 078</i> | 10                     | $3.5 \times 4$                   |
| <i>SI 097</i> | 30                     | $3.1 \times 3.6$                 |

**Table 4.1.:** Overview of MnSi samples.

## 4.2. $\text{CrB}_2$ single crystals

$\text{CrB}_2$  is an itinerant antiferromagnet below  $T_N = 88$  K. Although itinerant antiferromagnetism was observed long ago in the resistivity, magnetic susceptibility and specific heat [Bar69, Vaj01, Bal05], relatively little is known about this material. Its C32 crystal structure, which is characteristic for all diborides, is shown in Fig. 4.2. Closest-packed Cr layers and honeycomb B layers alternate along the [001] direction. The crystal has thus a rather two-dimensional character. The intralayer bonding forces in the boron layer, resulting from  $\pi$  and  $\sigma$  bonds, are much stronger than the interlayer bonding forces to the Cr layers. NMR studies of  $\text{CrB}_2$  powder samples [Kit78, Kit80] provided the first microscopic evidence for itinerant antiferromagnetism suggesting that  $\text{CrB}_2$  is located in the middle of the local moment and the weakly antiferromagnetic limits. Cycloidal magnetic order was inferred from neutron scattering experiments [Fun77]. An ordering wave vector  $\mathbf{q} = 0.285 \mathbf{q}_{110}$  and  $q_{110} = 2\pi/\frac{a}{2}$  was stated and a reduced ordered magnetic moment of  $0.5 \mu_B \text{ f.u.}^{-1}$  was found, which is characteristic of itinerant magnetism.

In this thesis the properties of a single crystal prepared by optical float-zoning [Bau13] were investigated. The crystal along with its structural and electrical pre-characterization data were provided by the group of Prof. Pfeleiderer at the Technische Universität München. For the growth, 99% isotopically enriched  $^{11}\text{B}$  was used to make neutron scattering experiments possible ( $^{10}\text{B}$  is a strong neutron absorber [Ama36]). Further details of the growth process are reported in Ref. [Bau13].

The sample was oriented by means of Laue x-ray scattering [Bau13]. To allow for cantilever magnetometry, it was cut by a wiresaw to give a cuboid of  $2.45 \times 2.2 \times 0.8 \text{ mm}^3$  parallel to  $[001] \times [100] \times [120]$ , respectively. Reference samples from the same ingot were pre-characterized and an excellent sample quality was established [Bau13]. The electrical resistivity of the samples decreases monotonically with decreasing temperature and dis-

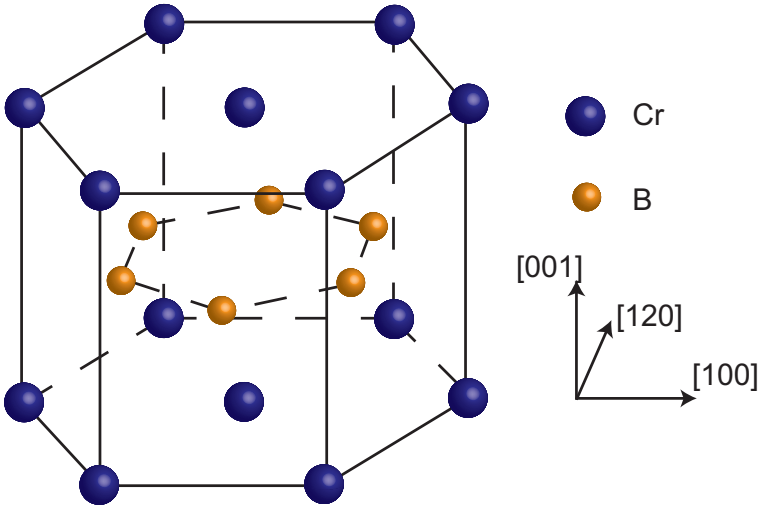


**Figure 4.2.:** C32 Crystal structure of  $\text{CrB}_2$ . Boron and chromium layers alternate along the  $[001]$  direction.

plays a distinct cusp at  $T_N$  followed by a temperature dependence consistent with a spin-gap of  $\sim 220$  K. The resistivity is moderately anisotropic by a factor of 1.5 to 4.5 at all temperatures (the resistivity for current along  $[100]$  is larger). At zero temperature the resistivity drops to a small sample-dependent value of a few  $\mu\Omega\text{cm}$  [Bau13]. The residual resistivity ratio is 11 for current along  $[100]$  and 31 for current along  $[001]$ . These values are the highest ones reported in literature. Finally, no contributions from Fe impurities have been observed which is in contrast to crystals used in earlier works [Bal05, Cas72].

### 4.3. MgZnO/ZnO heterostructures

Zinc oxide (ZnO) is a wide-band gap semiconductor. Its large direct band gap of 3.37 eV makes ZnO promising for advanced electronics. Possible applications include light-emitting diodes and lasers [Bag97], transparent conducting oxide layers for flat-panel displays and for field effect transistors [Nom03, Tsu07]. Recent progress in epitaxial growth of ZnO

has led to the realization of high-quality MgZnO/ZnO heterostructures [Aka10, Fal11]. The discovery that a 2DES forms at the interface of both materials without any intentional doping paved the way for an immense boost of this research field and meanwhile the QHE as well as the fractional QHE in this material system has been reported [Tsu07, Tsu10].

The samples investigated in this work have been grown and kindly provided by Y. Kozuka from the group of Prof. M. Kawaski, QPEC, University of Tokyo. They were fabricated using molecular beam epitaxy as described in detail in Ref. [Aka10, Fal11]. The sample schematics are depicted in Fig. 4.3 (a) and (b) in bird's eye and side view, respectively. On top of a 0.35 mm thick Zn-polar ZnO substrate, a ZnO buffer layer followed by a  $\text{Mg}_x\text{Zn}_{1-x}\text{O}$  layer was grown. The growth direction was the [0001] direction and a Mg content of  $x \sim 0.01$  was used [Fal11].

The formation of the 2DES at the interface is strongly related to the polar crystal structure of ZnO. It crystallizes in the wurtzite structure and therefore polarization effects along the [0001] direction have to be considered [Kob80]. Both, the buffer ZnO as well as the MgZnO layer exhibit a spontaneous polarization  $P_{\text{sp}}$  as denoted in Fig. 4.3 (b). While the ZnO buffer layer grows relaxed onto the ZnO substrate, there is a lattice mismatch between the ZnO and the  $\text{Mg}_x\text{Zn}_{1-x}\text{O}$  layer. This mismatch results in a compressive strain in the MgZnO layer along [0001] inducing a piezoelectric polarization  $P_{\text{pe}}$  [Yan07]. At the abrupt interface of ZnO and MgZnO the contributions from piezoelectric and spontaneous polarization induce an interface charge  $\sigma$  expressed as follows [Amb00, Tam08]:

$$\sigma = P_{\text{ZnO}} - P_{\text{MgZnO}} = P_{\text{sp}}^{\text{ZnO}} + P_{\text{pe}} - P_{\text{sp}}^{\text{MgZnO}} \quad (4.1)$$

The interface charge gives rise to an electric field inside the whole structure. Finally, the electric field induces a band bending as depicted in Fig. 4.3 which confines free charge carriers at the interface. For positive  $\sigma$  free electrons accumulate at the interface, which is the case for the samples investigated in this thesis [Fal11, Tsu07]. An analogous mechanism causes the formation of the 2DES in AlGaIn/GaN heterostructures [Amb00]. Following Ref. [Tsu07, Tam09] a schematic potential diagram can be constructed as depicted in Fig. 4.3 (c). A triangular quantum well at the interface drops below the Fermi level. The authors of Ref. [Tsu07] reported further, that at low temperatures only the lowest subband is occupied.

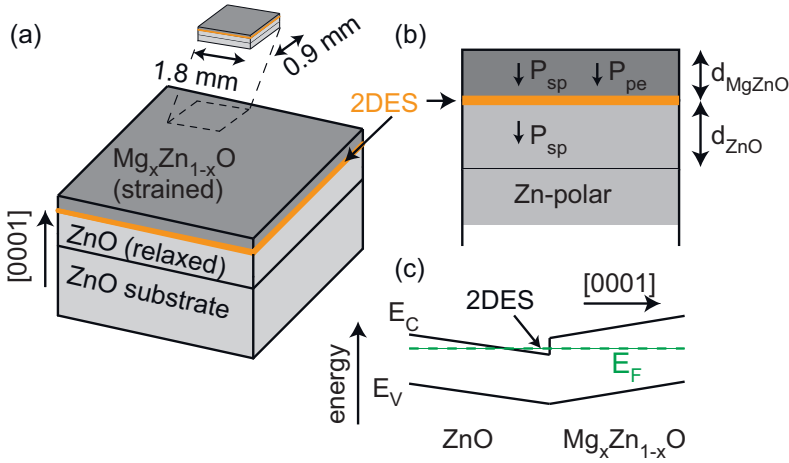


**Figure 4.3.:** Schematic of a MgZnO/ZnO heterostructure in bird's eye (a) and side view (b). The  $\text{Mg}_x\text{Zn}_{1-x}\text{O}$  layer is grown onto a relaxed ZnO layer. Both, ZnO and MgZnO, exhibit a spontaneous polarization  $P_{\text{sp}}$  because they crystallize in the wurtzite structure. Due to the lattice mismatch between both materials  $\text{Mg}_x\text{Zn}_{1-x}\text{O}$  is strained compressively and a piezoelectric polarization  $P_{\text{pe}}$  is induced additionally. At the interface a polarization discontinuity results which finally leads to an accumulation of free charge carriers. (c) Schematic potential diagram near the interface following Ref. [Tsu07].  $E_C$  and  $E_V$  denote the conduction- and valence-band, respectively. A triangular quantum well at the interface drops below the Fermi level  $E_F$  and confines a 2DES.

Transport measurements on a reference 2DES from the same batch have been performed by our Japanese collaborators. From Shubnikov-de Haas oscillations and Hall effect measurements the electron density  $n_s$  and the mobility  $\mu$  were inferred. Further details about the two samples investigated in this work are summarized in Table 4.2.

The as-grown heterostructures were machined to get a flip chip sample suitable for the cantilever sensors. Hence, the heterostructures were cut by a wire-saw and thinned from the backside. The resulting sample (and 2DES) area was  $0.9 \times 1.8 \text{ mm}^2$  and the thickness approximately  $30 \mu\text{m}$  as schematically depicted in Fig. 4.3 (a).



| Sample        | $d_{\text{ZnO}}$ (nm) | $d_{\text{MgZnO}}$ (nm) | $n_s$ ( $\text{cm}^{-2}$ ) | $\mu$ ( $\text{cm}^2/\text{Vs}$ ) |
|---------------|-----------------------|-------------------------|----------------------------|-----------------------------------|
| <i>zn0257</i> | 400                   | 220                     | $4.1 \times 10^{11}$       | $2.9 \times 10^5$                 |
| <i>zn0259</i> | 690                   | 380                     | $1.7 \times 10^{11}$       | $3.8 \times 10^5$                 |

**Table 4.2.:** Overview of MgZnO/ZnO samples.  $d_{\text{ZnO}}$  and  $d_{\text{MgZnO}}$  denote the thickness of the ZnO buffer layer and of the strained MgZnO layer, respectively.  $n_s$  and  $\mu$  are the electron density and the mobility, respectively.

## 4.4. Sensor preparation

Micromechanical cantilever sensors based on GaAs and on CuBe were used in this work as reported in Chapter 3. In the following the respective preparation techniques will be outlined.

### 4.4.1. GaAs based sensors

GaAs/AlAs heterostructures grown by molecular beam epitaxy were used for the fabrication of MCMs. The wafers incorporating the heterostructures were provided by Dr. Ch. Heyn in the group of Prof. W. Hansen from the University of Hamburg. Figure 4.4 (a) depicts the layer sequence of the heterostructure that was used for the cantilever preparation in this work. Onto a GaAs bulk substrate a GaAs/AlAs superlattice was grown, which serves as etch stop layer in the preparation process. This is followed by a 4400 nm thick GaAs layer. On top of the heterostructure, there are InGaAs self-assembled dots. They were removed in the preparation process and they are not relevant for this work.

The preparation of the sensor comprised the following steps [Sch00], which are illustrated in Figs. 4.4 (b-f).

1. The InGaAs dots were removed by a short, non-selective chemical etching process using a phosphoric acid/hydrogen peroxide etching solution.
2. The cantilever contour was defined by optical lithography on the front side of the GaAs heterostructure. Subsequently the heterostructure was etched laterally as depicted in (c) using the phosphoric acid/hydrogen peroxide etching solution. This process defines the cantilever contour. Note that the etching was performed

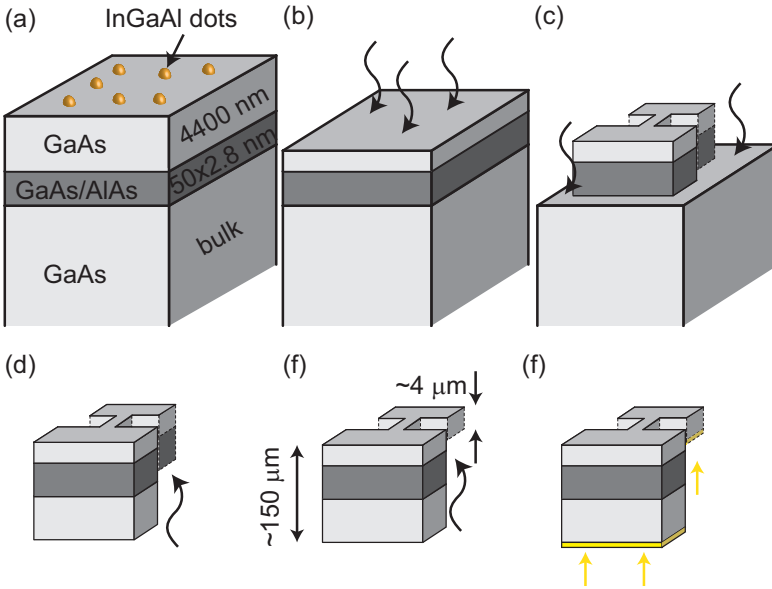


**Figure 4.4.:** Preparation process of the GaAs based sensors. (a) Layer sequence of the GaAs/AlAs heterostructure. (b) Removal of the InGaAs dots by non-selective chemical etching. (c) Definition of the cantilever contour by optical lithography and subsequent chemical etching. (d) Polishing the heterostructure from the backside to reduce overall thickness followed by lithography step to define the back-contact of the sensor. Subsequently a selective etching process from the backside removes the GaAs up to the etch stop layer. (e) Removal of the etch stop layer. (f) Evaporation of AuPd to metallize the backside of the cantilever.

to a depth  $\gtrsim 5 \mu\text{m}$  such that the AlAs/GaAs layer surrounding the contour was removed.

3. The heterostructure was then mechanically polished from the backside to reach a total thickness of  $\sim 150 \mu\text{m}$ . This procedure defined the distance  $d$  between cantilever backside and the counterelectrode as will become clear in the following.
4. The heterostructure was processed further from the polished backside in order to obtain a free standing cantilever. The contact

area at the backside, which is the cantilever foot at the same time, was defined by a resist contour via optical lithography. Then the heterostructure was etched from the backside using a citric acid/hydrogen peroxide etching solution, which is highly selective as shown in (d) . Thereby the GaAs at the backside of the heterostructure was removed until the GaAs/AlAs superlattice was reached. At this point the GaAs/AlAs superlattice served as etch stop layer and guaranteed a uniform thickness of the cantilever beam and paddle.

5. The GaAs/AlAs etch stop layer was removed by a non selective etching process as displayed in (e). The final thickness of cantilever beam and paddle was approximately  $4 \mu\text{m}$ .
6. Finally the cantilever was metalized from the backside to allow for capacitance measurements. For this a 17 nm thick AuPd layer was evaporated as depicted in (f).

A sapphire plate was used as substrate material. It was structured via optical lithography and subsequent Cr/Au evaporation and lift-off to provide the counter electrode, the electrode for the cantilever backside as well as a guard ring. The cantilever contact area was then attached to the respective electrode on the sapphire substrate using conducting silver paste. For this process a micro-manipulator setup was used. In the final step, the sample was attached to the free standing cantilever paddle using high vacuum grease. The cantilever glued to the sapphire substrate and accommodating the sample is schematically depicted in Fig. 3.4.

#### 4.4.2. CuBe based sensors

For larger samples and larger expected torque signals we chose the alloy copper beryllium (CuBe) as cantilever material. This material is characterized by a high strength (Young's modulus  $Y = 12 - 16 \times 10^{10} \text{ N/m}^2$ ) and is therefore often chosen for the fabrication of springs. In this work, CuBe foils with a thickness of  $50 \mu\text{m}$  were used for the cantilever preparation. The preparation procedure was as follows:

1. Photoresist was applied to cover one side of the CuBe foil uniformly. This will be denoted the backside of the foil in the following.

#### 4. Materials, sample details and preparation

---

2. On the front side of the foil the contour of the cantilever was defined by optical lithography.
3. The CuBe was removed via a wet chemical etching process using a  $\text{FeCl}_3$  solution.
4. In order to remove the resist from front- and backside of the cantilever the structure was rinsed in acetone.

The process provides the cantilever spring. In addition, we machined three,  $50 \mu\text{m}$  thick spacers out of the CuBe foil. They were used to define the distance  $d \approx 150 \mu\text{m}$  between the backside of the cantilever and the counter electrode. A printed circuit board was designed to fit our cantilevers and to provide a counter electrode and the relevant cantilever contact. Finally the spacers along with the cantilever were mounted onto the printed circuit board as schematically depicted in Fig. 3.3. The sample was glued to the free standing cantilever paddle. The dimensions of the cantilever paddle were  $4 \times 5 \text{ mm}^2$  and the length of the beam was given by 1.5 mm.

# 5. Magnetization of MnSi thin films

In this chapter we report results from cantilever torque magnetometry experiments on MnSi thin films. Regarding bulk MnSi, crystal growth is well established and the phase diagram has been studied intensively during the last years [Müh09, Yu10a, Bau12]. In contrast, the growth of high quality MnSi thin films has only recently become possible [Kar11, Li13]. During the course of this thesis, the phase diagram of thin film MnSi was still under debate and controversial results were published [Kar11, Kar12, Ton12]. Meanwhile, Lorentz transmission electron microscopy studies have been reported [Li13] which locally resolved the magnetic structure of thin film MnSi. However, the behavior on the macroscopic scale has not been refined yet, since there are no publications in line with the microscopic picture so far [Li13]. For this purpose torque magnetometry was applied in order to investigate the magnetic long-range order. The intention was to gain further insights into the phase diagram of thin film MnSi. The chapter is organized as follows: Sec. 5.1 briefly recapitulates the experimental methods applied in this specific experiment. In Sec. 5.2 cantilever magnetometry results as a function of magnetic field  $\mathbf{B}$ , temperature  $T$  and field orientation are shown. The phase diagram inferred from the torque magnetometry experiments is discussed in Sec. 5.3. Finally the magnetic anisotropy of thin film MnSi is addressed in Sec. 5.4.

## 5.1. Methods

Two samples of different MnSi thickness  $d_{\text{MnSi}}$  have been investigated: *SI 097* ( $d_{\text{MnSi}} = 30$  nm) and *SI 078* ( $d_{\text{MnSi}} = 10$  nm). Details of the sample structure and further sample properties can be found in Sec. 4.1. Both samples yielded qualitatively the same results. Thus, if not marked differently, results obtained with sample *SI 097* are shown in the following.

This sample showed a better signal to noise characteristic due to the larger  $d_{\text{MnSi}}$  compared to *SI 078*. The experiments have been performed using CuBe based cantilever sensors as described in Chapter 3. Samples were glued to the free standing cantilever plate, as depicted schematically in Fig. 5.1. The orientation of the  $[\bar{1}\bar{1}0]$  crystal axis was parallel to the cantilever axis. The cantilever deflection was read out using the capacitive technique shown in Chapter 3. We performed the experiments in the vector magnet system (c.f. Sec. 3.3). Thereby the magnetic field was rotated in the  $[\bar{1}\bar{1}0] - [111]$  crystal plane as shown in Fig. 5.1.  $\varphi$  denotes the angle between  $\mathbf{B}$  and the  $[111]$  direction. Measurements were performed in a  $^3\text{He}$  cryostat allowing temperatures from 0.28 – 60 K. The temperature was recorded by a calibrated *Cernox* temperature sensor mounted on the sample stage. Prior to all experiments, the samples were zero-field cooled. We note, that the in-plane superconducting magnet coil exhibited large flux jumps in the experiment. As a consequence readout overshoots and jumps in the capacitance occurred. These problems persisted at relatively large angles  $\varphi > 50^\circ$  and large magnetic fields  $B > 1.5$  T. Owing to the technical limitations measurements in this regime were not regarded for the discussion.

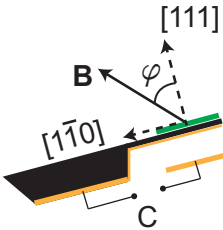


**Figure 5.1.:** Side view of the cantilever sensor including the MnSi thin film sample.  $\varphi$  denotes the angle between  $\mathbf{B}$  and the  $[111]$  crystal direction. The field is applied in the  $[111]$ - $[\bar{1}\bar{1}0]$  plane.

## 5.2. Experimental results

### Torque as a function of $B$

Figure 5.2 (a) shows the torque  $\Gamma$  as a function of  $B$  for various angles.  $T$  was set to 29 K. In all measurements we applied the following field sweep procedure at constant angle  $\varphi$ :  $B = 0 \text{ T} \rightarrow 3 \text{ T} \rightarrow -3 \text{ T} \rightarrow 3 \text{ T} \rightarrow 0 \text{ T}$ . Comparing the curves at different angles, we note that the variation of  $|\Gamma|$

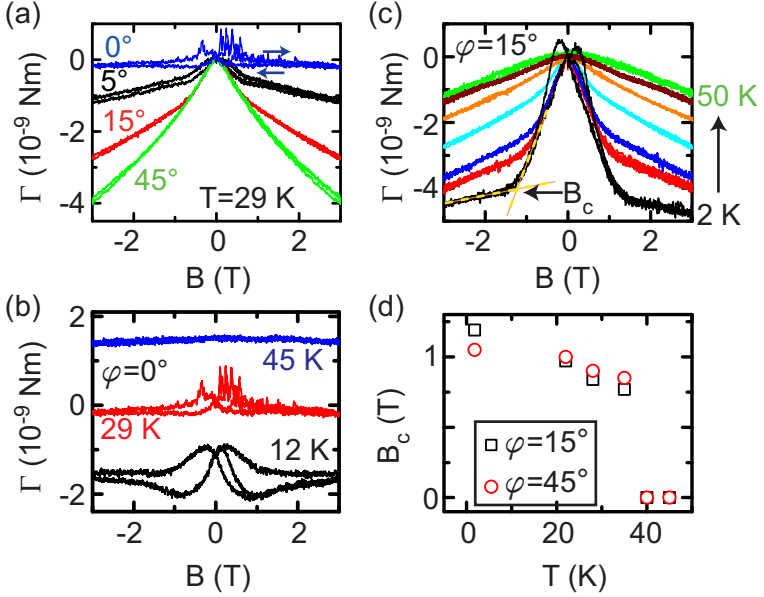


**Figure 5.2.:** (a)  $\Gamma(B)$  for different  $\varphi$  at  $T = 29$  K. The field sweep procedure was  $B = 0 \text{ T} \rightarrow 3 \text{ T} \rightarrow -3 \text{ T} \rightarrow 3 \text{ T} \rightarrow 0 \text{ T}$ . At small  $\varphi$  we observe a hysteresis. For  $\varphi = 0^\circ$  spike-like features are found near  $B \approx 0.4$  T. They are reminiscent of Barkhausen jumps. (b)  $\Gamma(B)$  at  $\varphi = 0^\circ$  for different temperatures. From bottom to top the temperature was set to  $T = 12$  K,  $T = 29$  K,  $T = 45$  K and the curves are shifted vertically for clarity. At  $T = 12$  K the torque is hysteric, but the curve is smooth near  $B \approx 0.4$  T. No hysteric or spike-like signature is found at  $T = 45$  K. (c)  $\Gamma(B)$  at  $\varphi = 15^\circ$ . From bottom to top  $T$  was set to: 2 K, 22 K, 29 K, 35 K, 40 K, 45 K, 50 K. For temperatures up to  $T = 35$  K a characteristic transition field  $B_c$  is identified.  $B_c$  is extracted as marked by the dashed lines. (d)  $B_c$  as a function of  $T$  for  $\varphi = 15^\circ$  (squares) and  $\varphi = 45^\circ$  (circles). For  $T \leq 35$  K,  $B_c$  decreases from  $B \approx 1.2$  T to  $B \approx 0.75$  T with increasing  $T$ .  $B_c$  drops to 0 between  $T = 35$  K and  $T = 40$  K. The angular variation of  $B_c$  is weak.

as a function of  $B$  is strong for large  $\varphi$ . For  $\varphi = 0^\circ$  and  $\varphi = 5^\circ$ , the curves of up- and downsweeps are not identical but hysteretic in  $B$ . For larger  $\varphi$  no hysteresis is resolved. At  $\varphi = 0^\circ$  the curve is, except for the hysteresis, almost flat. However, around  $B \approx 0.4$  T, spike-like structures are seen. They occur after sweeping  $B$  from one field direction through zero to the opposite direction. The systematics are comparable to switching processes (Barkhausen jumps) of a conventional ferromagnet near the coercive field. Note that at larger angles the spike-like features are absent. Instead, at  $|B| \approx 0.8$  T all curves exhibit a change in the slope which we attribute to a magnetic transition as discussed later.

In Fig. 5.2 (b) we reconsider the behavior of  $\Gamma(B)$  at  $\varphi = 0^\circ$  for different temperatures. From bottom to top the temperature was set to  $T = 12$  K,  $T = 29$  K,  $T = 45$  K and the curves are shifted vertically for clarity. At both,  $T = 12$  K and  $T = 45$  K, spike-like features are absent. At  $T = 12$  K and  $T = 29$  K  $\Gamma(B)$  is hysteretic while it is flat at  $T = 45$  K.

Figure 5.2 (c) shows  $\Gamma(B)$  at  $\varphi = 15^\circ$ . From bottom to top the temperature was set to: 2 K, 22 K, 29 K, 35 K, 40 K, 45 K, 50 K. At low  $T$  the variation of  $|\Gamma|$  as function of  $B$  is more pronounced. The curve at  $T = 2$  K exhibits a hysteresis, which is absent at elevated  $T$ . For  $T < 40$  K, the shapes of  $\Gamma(B)$  differ qualitatively from the ones at higher  $T$ . Starting from  $B = 0$  T  $|\Gamma(B)|$  increases significantly up to  $B_c \approx 1$  T. At  $B_c$  the slope changes abruptly. This is followed by a smooth increase of  $|\Gamma(B)|$  with a small slope at large  $B$ . In order to extract  $B_c$  we fit two linear functions as denoted by the dashed lines. Hence,  $B_c$  is the interception point of both fits. For  $T \geq 40$  K the data exhibit a uniform slope and a transition field is not resolved.

We summarize the obtained values for  $B_c$  at  $\varphi = 15^\circ$  and  $\varphi = 45^\circ$  as a function of  $T$  in Fig. 5.2 (d). At both angles, the temperature dependence of  $B_c$  is similar. For  $T \leq 35$  K,  $B_c$  decreases from  $B \approx 1.2$  T to  $B \approx 0.75$  T with increasing  $T$ . For  $T \geq 40$  K  $B_c$  is zero since no change of slope in  $\Gamma(B)$  was observed.

### Torque as a function of $T$

The temperature dependence of  $\Gamma$  is shown in Fig. 5.3. The experiment was conducted as follows: First,  $T$  was set to 55 K. Second,  $B = 0.4$  T was applied at  $\varphi = 90^\circ$ . Third,  $T$  was ramped down to 15 K and the torque was recorded simultaneously. With decreasing  $T$ ,  $\Gamma$  decreased smoothly. At



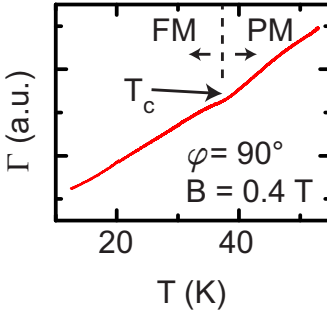


**Figure 5.3.:**  $\Gamma$  as function of  $T$  at  $B = 0.4$  T and  $\varphi = 90^\circ$ . Starting from  $T = 55$  K, the temperature is swept down to 15 K. Near  $T_c \approx 39$  K the curve exhibits a deflection point. We attribute this feature to the transition temperature of MnSi between the paramagnetic (PM) and the ferromagnetic (FM) state.

$T_c \approx 39$  K the curve displays a deflection point. Apart from this signature, no further significant variation was found. This experiment was repeated for various field strengths and angles. However, the deflection point was only resolved at  $\varphi = 90^\circ$ .

### Torque as a function of $\varphi$

The angular dependence of  $\Gamma$  is shown in Fig. 5.4. At fixed absolute value, the field orientation was varied from  $\varphi = -105^\circ$  to  $\alpha = 105^\circ$  and vice versa. Figure 5.4 (a) shows the results for  $T = 4$  K. The four curves correspond to  $B = 0.3$  T,  $B = 0.5$  T,  $B = 0.7$  T,  $B = 1.5$  T. All curves exhibit one torque maxima and one minima in the angular regime studied. This behavior corresponds to a twofold magnetic symmetry over a  $360^\circ$  range. The torque maxima (minima) increase (decrease) with increasing field strength. A rotational hysteresis is present in all curves. The hysteresis loop at  $B = 1.5$  T does not close due to a drift over time for  $\varphi \leq 140^\circ$ . Different temperatures are addressed in Fig. 5.4 (b).  $B$  was set to 0.8 T for all measurements and  $T$  was varied from 4 K to 50 K. The torque maxima (minima) show a strong  $T$  dependence. The peak-to-peak variation of  $\Gamma(\varphi)$  decreases significantly with increasing  $T$ . At  $T = 4$  K and  $T = 35$  K, a rotational hysteresis can be found. In contrast, there is no hysteresis for  $T = 50$  K.

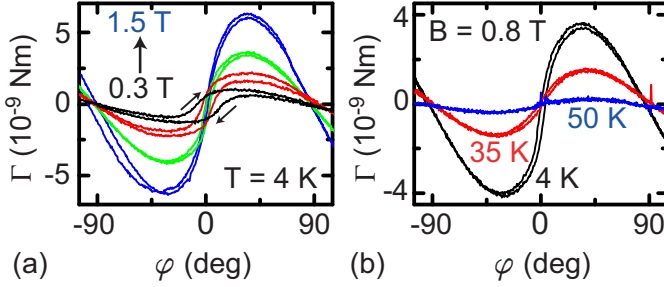


**Figure 5.4.:** (a)  $\Gamma(\varphi)$  at  $T = 4$  K. The field sweep direction is depicted by arrows.  $B$  was set to 0.3 T, 0.5 T, 0.8 T and 1.5 T. All curves exhibit a rotational hysteresis. The torque extrema increase with increasing  $B$ . At  $B = 1.5$  T drifts over time occurred. (b)  $\Gamma(\varphi)$  at  $B = 0.8$  T for various  $T$ . Torque extrema and rotational hysteresis decrease with increasing  $T$ . At  $T = 50$  K no hysteresis is observed.

### 5.3. Phase diagram inferred from torque magnetometry

In this section we discuss the torque magnetometry results focusing on the classification and assignment of magnetic phases in thin film MnSi. The results will be interpreted in the context of other recent works on the phase diagram of thin film MnSi [Li13, Kar12].

From the observations presented in Sec. 5.2 we derive the following statements:

- The hysteresis observed in the  $\Gamma(B)$  and  $\Gamma(\varphi)$  data is a clear indication for the existence of collective magnetism in the MnSi sample. The hysteresis in  $\Gamma(B)$  was observed only at low  $T$ , whereas the rotational hysteresis persisted up to  $T \leq 35$  K. At larger  $T$ , the hysteresis was absent. We conclude that collective magnetism is present for  $T \leq 35$  K.
- The temperature dependence shown in Fig. 5.3 revealed a deflection point at  $T \approx 39$  K. In combination with the conclusions drawn above this observation supports the notion that a phase transition into a magnetically ordered phase took place at  $T_c \approx 39$  K when  $T$  was varied from high to low temperatures. Above  $T_c \approx 39$  K, the

MnSi thin film is presumably paramagnetic. This statement is supported by the measurement results for  $\Gamma(\varphi)$  at  $T = 50$  K. Here no rotational hysteresis was found which points towards a paramagnetic state of MnSi.

- Next we consider the change of the slopes in  $\Gamma(B)$  at  $B_c$  for  $T \leq 35$ . In this temperature regime  $B_c$  ranged from  $\sim 1.2$  T to  $\sim 0.75$  T. For  $T > 35$  K we observed no change in the slope of  $\Gamma(B)$ . In addition, the  $\Gamma(\varphi)$  data suggests collective magnetism below *and* above  $B_c$  for  $T < T_c$  which is manifested by the rotational hysteresis. Thus we attribute the change of slopes at  $B_c$  occurring at  $T < T_c$  to a transition between two magnetically ordered states. For  $T > T_c$ , MnSi is paramagnetic and no transition at  $B_c$  is expected, which is consistent with our observations. In the context of the results reported in Ref. [Li13], we interpret the behavior at  $B_c$  as a transition from an ordered, but non-collinear, spin state into a field polarized state.
- For  $B$  aligned along the sample normal spike-like features in  $\Gamma(B)$  near  $B \approx 0.4$  T have been found at  $T = 29$  K. They are reminiscent of the well-known Barkhausen jumps in ferromagnets. On account of this resemblance we attribute these features to domain nucleation, domain wall movement as well as domain reorientation processes in the MnSi thin film. Li *et. al.* [Li13] reported a skyrmion phase in MnSi thin films in this temperature and field region. Interestingly, the spike features are not present at low temperatures, e.g. at  $T = 12$  K, although we identified a magnetically ordered phase in this temperature regime. Thus one could speculate that the observed structures are caused by the formation of the skyrmion phase.

From these consideration we extract a preliminary phase diagram which is shown in Fig. 5.5. At high  $T$ , the MnSi thin film is paramagnetic. At  $T_c \approx 39$  K and  $B < B_c$  a transition into a ferromagnetic, non-collinear spin state takes place. For  $T < T_c$  MnSi turns into a field-polarized state at  $B_c \approx 1$  T.  $B_c$  and  $T_c$  are found to be rather insensitive to the direction of the applied field.

The phase diagram and the extracted values for  $B_c$  and  $T_c$  are in reasonable agreement with the findings reported in Refs. [Kar12, Li13]. On top of that these works report a helical, a conical and a skyrmion phase in the regime  $B < B_c$  and  $T < T_c$ . In particular, Li. *et al.* [Li13] found

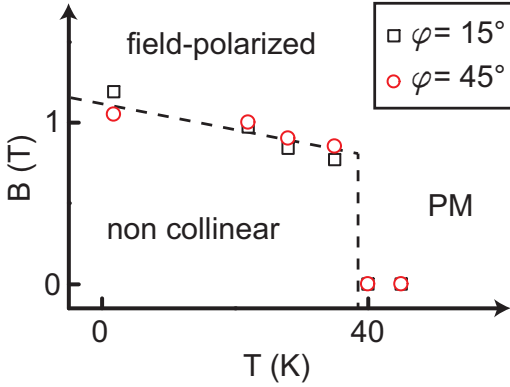


**Figure 5.5.:** Phase diagram of thin film MnSi inferred from torque magnetometry. Data points are adopted from Fig. 5.2 (d). At  $T \lesssim 39$  K and  $B \lesssim 1$  T, the MnSi thin film exhibits collective magnetism. We denote this regime as non-collinear spin state which possibly comprises a skyrmion phase (see text). At  $B \approx 1$  T a transition to a field-polarized state takes place. For  $T \geq 39$  K the MnSi thin film is paramagnetic.

a pronounced skyrmion phase pocket below  $B_c$  and in the temperature range  $15 \text{ K} < T < T_c$ . Our experiments, however, do not hint at the existence of further phase boundaries in the phase diagram in this regime. Nevertheless, in the light of the work of Li. *et al.* we assume that an extended skyrmion phase could be present in our samples as well. An indication, that supports this notion is the observation of spike-like features at  $T = 29$  K. Above, we speculated that the well known domain processes cause the spikes. In addition, the spikes may as well correspond to the formation or destruction of different skyrmion domain phases. As was speculated in Ref. [Li13] magnetic long range order might be suppressed in MnSi thin films but instead a domain-like skyrmion structure might exist. In our opinion the torque magnetometry experiments corroborate the speculations about missing long-range order in the skyrmion phase. At  $T = 12$  K, we did not observe spike-like features. In this temperature regime the skyrmion phase is suppressed according to Ref. [Li13]. Thus, the observation is in accordance with the line of argumentation above.

Finally, let us tackle the question why there are no further phase boundaries observed below  $T_c$  and  $B_c$ . It is supposed [Kar12, Li13] that phases of

conical or helical spin structures are also stable in this regime. However, if the magnetic configuration and thus the magnetic torque between two states is very similar, the corresponding transition might not be resolved by our measurement technique. This may explain the absence of further phase boundaries.

## 5.4. Magnetic anisotropy

We now focus on the discussion of the magnetic anisotropy properties of thin film MnSi as inferred from  $\Gamma(\varphi)$  measurements shown in Fig. 5.4. Comparing the data with the numerical model calculations introduced in Sec. 2.1.3 the following conclusions can be drawn:

- The MnSi thin film exhibits a predominantly uniaxial anisotropy. The twofold symmetry of the  $\Gamma(\varphi)$  curves is a clear indication of the presence of one easy axis. The direction of the easy axis is inferred from the slopes of the torque vs. angle curves. At  $\varphi = -90^\circ$  and  $\varphi = 90^\circ$  the curves exhibit a smaller slope than at  $\varphi = 0^\circ$ . Thus, the easy axis is aligned along the  $[1\bar{1}0]$  direction giving rise to an easy plane. The hard axis points along the  $[111]$  direction. In addition, the occurrence of a rotational hysteresis around  $\varphi = 0^\circ$  also indicates the existence and orientation of the hard axis. These results are in accordance with Ref. [Kar12].
- The observation of a rotational hysteresis can be traced back to two phenomena. Below  $B_c$ , the spins are not ordered collinear such that  $M$  is below  $M_s$ . In this regime the hysteresis can be attributed to the presence of domain wall displacements as well as irreversible magnetization rotation [Chi09]. At  $B = 1.5$  T, which is above  $B_c$ , the hysteresis still persists. In this regime, irreversible magnetization rotation causes the rotational hysteresis.
- The maxima (minima) of  $\Gamma(\varphi)$  increase (decrease) with increasing  $B$ . From the comparison with the calculations presented in Sec. 2.1.3 this behavior is expected for torque measurements on a specimen which is not magnetically saturated, so that  $M < M_s$ . The conclusions drawn in Sec. 5.3 yield a  $B_c$  of approximately 1.1 T at 4 K. Thus for  $B < B_c$  the MnSi thin film is not saturated. In this

regime, methods to determine the magnetic anisotropy usually fail [Bur77, Chi09].

- The shape of the  $\Gamma(\varphi)$  curves suggest that  $B > B_a$ , where  $B_a$  denotes the anisotropy field as introduced in Sec. 2.1.3. Further, we assume that we can set  $M = M_s$  at the highest applied field  $B = 1.5$  T. Hence, the usual procedure to determine the anisotropy constants from torque curves [Bur77, Chi09, Hub98] can be applied. However, we have to bear in mind that the CuBe cantilever and the Si substrate also have to be taken into account. Both, CuBe and Si, are rather weak diamagnets [Can77, Cor11] and thus contribute weakly to the acquired torque signal. Therefore, for the matter of simplification their contribution will be neglected in the following analysis. Following Refs. [Bur77, Hub98], the method of torque correction was applied. For known  $\mathbf{B}$  and  $\mathbf{M}_s$ , the angle between them, denoted by  $\varphi - \Phi$ , is calculated via  $\varphi - \Phi = \arcsin[\Gamma_m/BM_s]$ .  $\Gamma_m$  denotes the measured torque. This allows us to determine  $\Phi$ , i.e. the angle between  $\mathbf{M}$  and the [111] direction (c.f. Fig. 2.1 and Fig. 5.1). Moreover, the torque  $\Gamma_{\text{int}}$  plotted as function of the angle  $\Phi$  represents the so-called intrinsic torque. Both,  $\Gamma_m(\varphi)$  and  $\Gamma_{\text{int}}(\Phi)$  normalized by the volume of the MnSi film, are plotted in Fig. 5.6. Obviously, the transformation of  $\Gamma_m(\varphi)$  into  $\Gamma_{\text{int}}(\Phi)$  is analogous to a shearing of the curve. If the extrema stay invariant under this torque correction operation, the desired information, namely the anisotropy constant  $K_u^*$ , can directly be determined from the plot [Bur77, Hub98]. It is given by the torque extrema as denoted in Fig. 5.6. Via

$$K_u^* = K_u + 1/2\mu_0 M^2 \quad (5.1)$$

we can evaluate  $K_u$ . For *SI 097* ( $d_{\text{MnSi}} = 30$  nm),  $K_u$  yields  $1.2 \text{ kJm}^{-3}$  and agrees within the error bar with the value reported in Ref. [Kar12]. Regarding *SI 078* ( $d_{\text{MnSi}} = 10$  nm), we obtain  $K_u = 7.9 \text{ kJm}^{-3}$ , which is about a factor of 4 smaller than the  $K_u$  reported by Karhu *et al.* [Kar12]. Further they found a strong dependence of  $K_u$  on growth related parameters and annealing times which might also be the reason for the observed discrepancy of  $K_u$  at  $d_{\text{MnSi}} = 10$  nm.

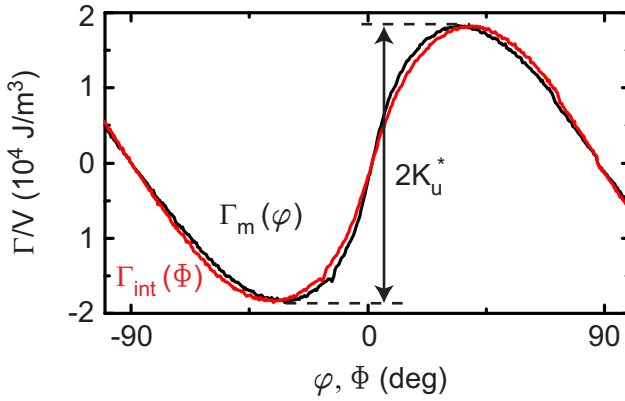


**Figure 5.6:**  $\Gamma_m(\varphi)$  denotes the measured torque density of 30 nm thick MnSi.  $\Gamma_{\text{int}}(\Phi)$  is the derivative of the anisotropy energy density. The peak-to-peak variation yields  $2K_u^*$ . Assuming a simple uniaxial anisotropy, the anisotropy constant  $K_u$  amounts to  $1.2 \times 10^3 \text{ J/m}^{-3}$ .





# 6. De Haas-van Alphen effect and Fermi surface properties of CrB<sub>2</sub>

In this chapter the de Haas-van Alphen (dHvA) effect in single crystal CrB<sub>2</sub> inferred from the quantum oscillatory components of the torque magnetization is investigated. Parts of the results presented here have been submitted for publication [Bra13a].

The chapter is organized as follows: First, the experimental methods are presented in Sec. 6.1. Then experimental results of angular and temperature dependent cantilever magnetometry measurements are shown and analyzed in Sec. 6.2. This is followed by a description and analysis of band structure calculations in Sec. 6.3. Finally experimental findings and calculations are compared and discussed in Sec. 6.4 before a brief comparison with the isostructural compound MgB<sub>2</sub> is outlined in Sec. 6.5.

## 6.1. Experimental methods

For the experiment we employed cantilevers based on CuBe foils (c.f. Sec. 3.3). The capacitive readout scheme was applied to measure the cantilever deflection. A <sup>3</sup>He cryostat was used to measure at temperatures between 0.3 K and 3.5 K. The temperature was monitored with a calibrated *Cernox* temperature sensor. The measurements were conducted in an axial magnet allowing magnetic fields up to 14 T. The sample stage was equipped with a mechanical rotator to change the angle of the cantilever and attached sample with respect to the magnetic field in situ with a resolution better than 0.2° [Rup13]. Details of the CrB<sub>2</sub> sample have been described in Chapter 4. In our magnetometry experiments we address the antiferromagnetic phase of CrB<sub>2</sub> since we are well below  $T_N = 88$  K [Bar69, Vaj01]. The dHvA effect was investigated in two principal planes

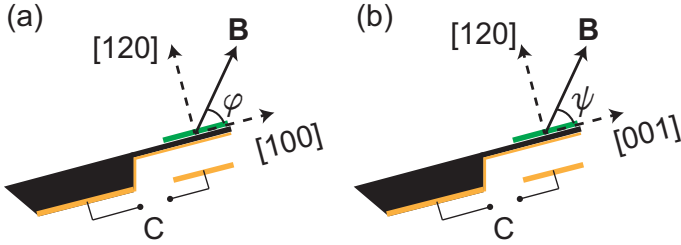
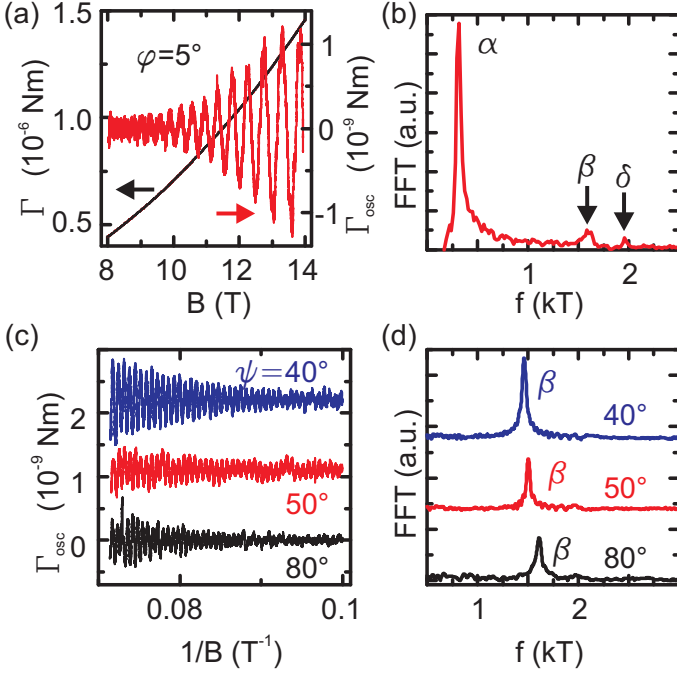


**Figure 6.1.:** Side view of the cantilever with attached sample to illustrate the orientation of the applied field with respect to the crystal axes. (a) Rotation of  $\mathbf{B}$  in the hexagonal basal plane denoted by angle  $\varphi$ . (b) Rotation of  $\mathbf{B}$  in the  $[001] - [120]$  plane denoted by angle  $\psi$ .

of the hexagonal crystal structure as illustrated in Fig. 6.1. In a first set of experiments, the magnetic field was rotated in the hexagonal basal plane ( $[100] - [120]$  plane) described by the angle  $\varphi$  with respect to the  $[100]$  direction (see Fig. 6.1 (a)). After that, the sample was rotated by  $90^\circ$  on the cantilever. In a consecutive cooldown cycle the field was applied in the  $[001] - [120]$  plane as shown in Fig. 6.1 (b). Here,  $\psi$  denotes the angle between  $\mathbf{B}$  and the  $[001]$  axis.

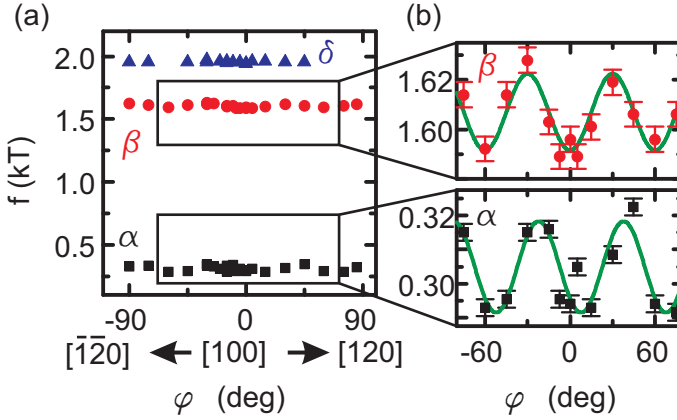
## 6.2. Experimental results

Figure 6.2 (a) shows the raw torque data versus magnetic field  $B$  (black line) in the hexagonal plane (c.f. Fig. 6.1 (a)) for  $\varphi = 5^\circ$  and at  $T = 0.3$  K. The quantum oscillations are superimposed on a monotonic background signal. In order to extract the oscillatory signal component  $\Gamma_{\text{osc}}$  a high-order polynomial was fitted in  $1/B$ . This fit was then subtracted from the data to dispose of the background signal leaving the pure dHvA signal.  $\Gamma_{\text{osc}}$  is shown in Fig. 6.2 (a) as a red line. The dHvA frequencies  $f$  were determined by Fast-Fourier-Transforms (FFT) of  $\Gamma_{\text{osc}}(1/B)$ . For a consistency check, another method, the so-called Maximum Entropy Method (MEM) [Sig92], was also applied to extract the dHvA frequencies. Both, FFT and MEM, gave the same results. Therefore only FFT spectra will be considered in the following. Figure 6.2 (b) depicts the corresponding FFT spectrum for  $\varphi = 5^\circ$ . We can identify three distinct maxima which we



**Figure 6.2.:** (a) The torque  $\Gamma$  (black line) and the oscillatory torque  $\Gamma_{\text{osc}}$  (light line) as a function of magnetic field  $B$  for  $\varphi = 5^\circ$  at  $T = 0.3$  K. (b) Fourier Transform of  $\Gamma_{\text{osc}}(1/B)$  revealing three distinct orbits  $\alpha$ ,  $\beta$  and  $\delta$ . (c)  $\Gamma_{\text{osc}}$  for three different angles  $\psi$  at  $T = 0.3$  K. (d) Corresponding FFTs showing one dHvA orbit that shifts in frequency as function of  $\psi$ .

assign to the frequencies  $f_\alpha$ ,  $f_\beta$  and  $f_\delta$ . According to the Lifshitz-Onsager relation  $P_i = 2\pi e f_i / \hbar$  derived in Eq. 2.28, the dHvA frequencies  $f_i$  are directly connected to extremal orbits with cross sectional area  $P_i$ . In Fig. 6.2 (c) we present  $\Gamma_{\text{osc}}$  for three different angles  $\psi$  with the magnetic field applied in the  $[001] - [120]$  plane (c.f. Fig. 6.1 (b)). The curves are shifted in vertical direction for clarity. The corresponding FFTs are shown in Fig. 6.2 (d). Here, only one frequency  $f_\beta$  is clearly resolved.



**Figure 6.3.:** (a) Angular dependence of the dHvA frequencies for a rotation of the magnetic field in the  $[100] - [120]$  plane showing three orbits  $\alpha$ ,  $\beta$  and  $\delta$  (b) Expanded view of the angular dependence of  $\alpha$  and  $\beta$ . Both orbits exhibit a  $60^\circ$  periodicity. Lines are  $60^\circ$  periodic sinusoidal fits to illustrate the periodicity.

### 6.2.1. Angular dependence

The angular dependence of the dHvA effect was studied in both principal planes. A map of the  $[100] - [120]$  plane is shown in Fig. 6.3. The orbits  $\alpha$ ,  $\beta$  and  $\delta$  are recovered at frequencies  $f_\alpha \approx 300$  T,  $f_\beta \approx 1600$  T and  $f_\delta \approx 1950$  T, respectively. They were traced over an angular regime  $\Delta\varphi > 90^\circ$ , indicating that they belong to closed Fermi surface sheets. Further, the orbits  $\alpha$ ,  $\beta$  and  $\delta$  show only a small variation in frequency. This characteristic indicates that the cross sectional area perpendicular to the basal plane varies only slightly as a function of  $\varphi$ . Figure 6.3 (b) shows an expanded view of the frequency branches  $\alpha$  and  $\beta$ . The variation in frequency corresponds to a peak-to-peak change in extremal area of about 10 % for orbit  $\alpha$  and 2 % for orbit  $\beta$ . Besides, the data exhibit a small but clear  $60^\circ$  periodicity. The underlying lines are  $60^\circ$  periodic sinusoidal fits to the data to illustrate this behavior. The periodicity is consistent with the hexagonal symmetry of the  $\text{CrB}_2$  crystal. Concerning orbit  $\delta$  no definite statement can be made about its periodicity since it was not resolved over the whole frequency regime. Whether this is an intrinsic effect or due to experimental limitations is unclear at present.

The angular dependence of the dHvA frequencies in the  $[001] - [120]$  plane is shown in Fig. 6.4. Only the orbit  $\beta$  in the range  $1380 \text{ T} \leq f_\beta \leq 1620 \text{ T}$  is present. The orbits  $\alpha$  and  $\delta$  are not resolved. The orbit  $\beta$  can therefore be traced in both symmetry planes again identifying the Fermi surface corresponding to  $\beta$  as a closed surface. In a first approach, we describe this Fermi surface as an elongated ellipsoid. This is schematically depicted in the inset of Fig. 6.4. The orbit of the extremal area  $P_\beta$  is then the intersection of a plane with an ellipsoid [Sch12a], given by

$$P_\beta = \pi v w / \sqrt{\sin^2 \psi + (v^2/w^2) \cos^2 \psi}, \quad (6.1)$$

where  $v$  and  $w$  denote the semi-major and semi-minor axes of the ellipse in reciprocal space. The resulting fit shown in Fig. 6.4 is in good agreement with the data points and yields  $v = (2.38 \pm 0.01) \cdot 10^9 \text{ m}^{-1}$  and  $w = (2.05 \pm 0.01) \cdot 10^9 \text{ m}^{-1}$ . Here,  $v$  is the reciprocal-space extent of the ellipsoid along the  $[001]$  direction. We thus deal with a FS sheet that is well described as an ellipsoid elongated in the  $[001]$  direction. In the basal plane the FS pocket exhibits a very small six-fold modulation of its surface.

The absence of orbits  $\alpha$  and  $\delta$  for  $B$  applied in the  $[001] - [120]$  plane cannot be explained by open FS sheets as already inferred above. In addition, when we compare both data sets (Fig. 6.3 and Fig. 6.4) for  $B$  aligned along the symmetry direction  $[\overline{1}20]$ , the frequencies are visible in the experiment for one direction of the torque while they are absent for the other. If an orbit turns into an open orbit in a certain field direction, this will cause its disappearance regardless of the torque direction. Thus, the disappearance of this orbit in only one torque direction cannot be caused by the orbit turning into an open orbit, but must be caused by another mechanism. As introduced in Eq. 2.29 the torque for  $B$  applied in the  $[001] - [120]$  plane can be written as  $\Gamma_{\text{osc}} = -\frac{1}{f} \frac{\partial f}{\partial \psi} M_{\parallel} B$ , where  $f$  denotes the dHvA frequency and  $M_{\parallel}$  the magnetization component parallel to the magnetic field. For a Fermi surface with low anisotropy  $\frac{\partial f}{\partial \psi}$  can go to zero [Sho84], causing the oscillatory torque signal to vanish in specific symmetry planes. This effect could account for the absence of the frequency branches  $\alpha$  and  $\delta$  in Fig. 6.4.

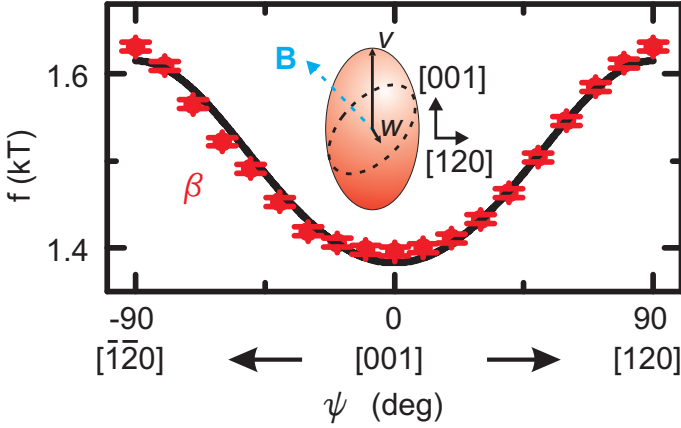


**Figure 6.4.:** Angular dependence of orbit  $\beta$  for rotation of the magnetic field in the  $[001] - [120]$  plane. Orbits  $\alpha$  and  $\delta$  are missing. The data is fitted by a curve (solid line) expected for an ellipsoidal Fermi surface sheet. The inset shows a schematic sketch of an ellipsoidal Fermi surface sheet where the dashed lines enclose the area  $P_\beta$  for an arbitrary angle  $\psi$ .

## 6.2.2. Temperature dependence

The temperature dependence of the dHvA effect for orbit  $\beta$  is shown in Fig. 6.5 (a). The magnetic field was applied along  $\psi = 80^\circ$ . It was oriented at small angles off the symmetry axis ( $\psi = 90^\circ$ ) because the torque signal vanishes for the field aligned parallel to the symmetry axis. The temperature was varied from  $T = 0.3$  K up to  $T = 3.5$  K. The dHvA amplitudes clearly decrease with increasing temperature.

In order to analyze the dHvA data we applied the Lifshitz-Kosevich (LK) formalism (c.f. Sec. 2.2.3). From the FFTs of the dHvA data we extracted the amplitudes of the FFT peaks as a function of  $T$ . The normalized FFT peak amplitudes of orbits  $\alpha$  and  $\beta$  are shown in Fig. 6.5 (b) (data points). The expression

$$R_T = X / \sinh X, \quad \text{with } X = \left( \frac{2\pi^2 k_B m^* T}{\hbar e B} \right) \quad (6.2)$$

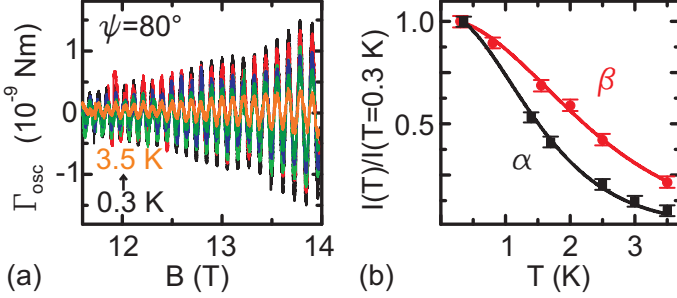


**Figure 6.5.:** (a) Temperature dependence of orbit  $\beta$  at  $\psi = 80^\circ$ . Going from largest to smallest dHvA amplitudes the temperature was set to  $T = 0.3$  K,  $T = 0.8$  K,  $T = 1.5$  K,  $T = 2.0$  K,  $T = 2.5$  K,  $T = 3.5$  K. (b) Normalized FFT amplitudes  $I(T)$  (symbols) and LK fit (solid line) as a function of temperature. The FFT amplitudes were obtained using a fixed-field window as depicted e.g. in (a). In the expression for  $R_T$  the average field of this window  $\bar{B} = (B_{\min} + B_{\max})/2$  was used. The fits yield the effective masses  $m_\alpha^*/m_e = 1.22 \pm 0.12$  and  $m_\beta^*/m_e = 0.86 \pm 0.07$ .

was fitted to the data (line). Here, the average field of the FFT window  $\bar{B} = (B_{\min} + B_{\max})/2$  was inserted.  $m^*$  was used as free fit parameter. The LK fit yields  $m_\alpha^*/m_e = 1.22 \pm 0.12$  and  $m_\beta^*/m_e = 0.86 \pm 0.07$ . The error bars were determined from the standard deviation of the LK fit. For orbit  $\delta$ , the LK formalism was only applied at temperatures  $T \leq 1.5$  K due to the small signal-to-noise ratio at larger  $T$ . We obtain an effective mass  $m_\delta^*/m_e = 1.07 \pm 0.06$  for this orbit. This value might contain a systematic error, since only few data points could be collected.

Provided with the effective mass the mean free paths can be determined. Therefore the LK formula (c.f. Eq. 2.34)

$$\Gamma_{\text{osc}} \propto \sum_{\text{orbits}} B^{3/2} R_D R_T \sin\left(\frac{2\pi f}{B} + \gamma\right) \quad (6.3)$$

is fitted to our data. Here,  $\gamma$  accounts for the phase. We inserted  $m^*$  as determined above. This analysis yields the Dingle factor  $R_D = \exp[-\pi m_b/eB\tau]$ , which is used as free fit parameter. The results for orbit  $\alpha$  and  $\beta$  are shown in Fig. 6.6 (a) and Fig. 6.6 (b), respectively. The fits agree reasonably well with the experimental data.

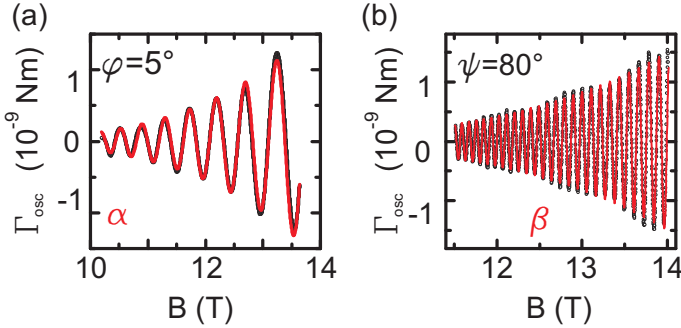


**Figure 6.6.:** Experimental data  $\Gamma_{\text{osc}}$  vs.  $B$  at  $T = 0.3$  K (symbols) for orbit (a)  $\alpha$  at  $\varphi = 5^\circ$  and (b)  $\beta$  at  $\psi = 80^\circ$ . The LK formula (Eq. 6.3) is fitted (solid line) using  $m_\alpha^*/m_e = 1.22$  and  $m_\beta^*/m_e = 0.86$  as determined above. The fits yield the mean free paths  $l_\alpha = 26$  nm and  $l_\beta = 69$  nm.

Following Refs. [Yel02, Arn11], we obtain a good estimation for the mean free paths as follows: Considering free electrons we can replace  $m_b/\tau$  by  $\hbar k_F/l$  in the expression for  $R_D$ . Here,  $k_F$  denotes the Fermi wave vector and  $l$  is the mean free path. If we approximate that the frequency  $f$  arises from a circular area in reciprocal space we can write  $\pi k_F^2 = 2\pi e f/\hbar$ . This procedure allows us to determine  $l$  from the LK fit. Values for the mean free path extracted this way are 26 nm, 69 nm and 67 nm for orbits  $\alpha$ ,  $\beta$  and  $\delta$ , respectively.

### 6.3. Electronic structure of CrB<sub>2</sub>

In order to further analyze and interpret our experimental findings, electronic structure calculations have been performed. These calculations were done by our collaboration partners J. Kuneš and L. Chioncel and they were published in Ref. [Bra13a]. First, the theoretical methods will be briefly explained in Sec. 6.3.1. Second, results from the electronic structure calculations for spin polarized CrB<sub>2</sub> are presented in Sec. 6.3.2. This is followed by an analysis of the expected angular dependence of the dHvA frequencies and band masses in Sec. 6.3.3.



### 6.3.1. Theoretical methods

J. Kuneš and L. Chioncel applied the local spin density approximation (LSDA) method of density functional theory by using the full-potential linearized augmented plane-wave method implemented in the WIEN2k package [Bla12, Las04, Kun04]. In the calculations they used the experimental values for the lattice parameters  $a = 2.969 \text{ \AA}$  and  $c = 3.066 \text{ \AA}$ . The results were compared to calculations in the Generalized Gradient Approximation (GGA) of the exchange and correlation functionals and were found to be consistent. Cycloidal magnetic order with ordering vector  $\mathbf{q}$  was treated using the generalized Bloch theorem [San98]. Comparing the total energies for several  $\mathbf{q}$ -vectors along the [110] and [100] directions the lowest energy was found for  $\mathbf{q} = 0.3 \pm 0.05 \mathbf{q}_{110}$  in good agreement with  $\mathbf{q} = 0.285 \mathbf{q}_{110}$  found in Ref. [Fun77] and substantiated by neutron scattering experiments performed in the groups of Prof. Pfeleiderer and Prof. Böni at the Technische Universität München [Reg]. Additional calculations for the collinear ferromagnetic state and the nonmagnetic state were performed in order to find out how sensitive different parts of the Fermi surface are to the magnetic order. Results of the calculations for the nonmagnetic state are presented in Appendix A.

Further, we evaluated the results of the band structure calculations using the SKEAF (Supercell K-space Extremal Area Finder) [Rou12] tool. This numerical algorithm allows to extract the dHvA frequencies as well as the band masses  $m_b$  for an arbitrary orientation of field with respect to the crystal axes.

### 6.3.2. Results from band structure calculations

The electronic structure calculations suggest that mainly B- $p$  and Cr- $d$  states are present at the Fermi level (c.f. Appendix A). The band structure of CrB<sub>2</sub> assuming cycloidal magnetic order is depicted in Fig. 6.7. In total, three bands (denoted in blue, black and orange color) cross the Fermi level. The corresponding Fermi surfaces are shown in Figs. 6.8 (a-c). We plot the Fermi surface sheets originating from different bands separately for clarity. The Fermi surface shown in Fig. 6.8 (a) corresponds to the band depicted in blue and consists of a singly connected trunk-like structure with multiple extrusions centered around the  $L$  points at the Brillouin zone boundary. It has dominantly Cr- $d$  character and is hole-like.

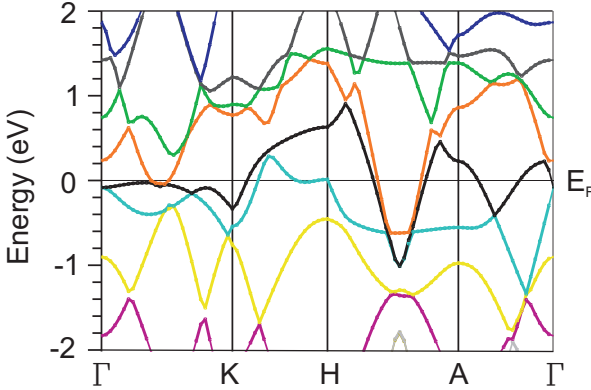


**Figure 6.7.:** Calculated band structure of CrB<sub>2</sub> with a cycloidal magnetic ordering wave vector  $\mathbf{q} = 0.3 \mathbf{q}_{110}$  using the WIEN2k package. In total, three bands (blue, orange, black) cross  $E_F$ .

In Fig. 6.8 (b) the Fermi surface sheets corresponding to the black band in Fig. 6.7 are depicted. Here a complicated multiply connected structure centered around  $\Gamma$  is present. In addition we find multiple copies of two different singly connected pockets. It is important to note that among these FS sheets only the two copies of the pocket located between the A- and H-point have a ball-like closed surface of high symmetry, like that observed in the experiment. Except for this electron pocket, which is derived from B-*p* states, the Fermi surface sheets of this band can be traced to Cr-*d* orbitals. In Fig. 6.8 (c) we show the Fermi surface pockets arising from the band depicted in orange. Here, two copies of a ball-shaped pocket located between A and H and two copies of a dumbbell-shaped pocket are present. They are closed and electron-like. The spherical pocket is due to B-*p* orbitals whereas the dumbbell-shaped sheet has dominantly Cr-*d* character. We note that the ball-shaped pockets in (b) and (c) also occur in the non-magnetic calculation, which is presented in the Appendix A. There, they are single copies centered around the A point. The doubling of the pockets and the shift along the A-H direction in the magnetic calculation is a direct consequence of the lifting of the spin degeneracy and the direction of the magnetic ordering wave vector, respectively.

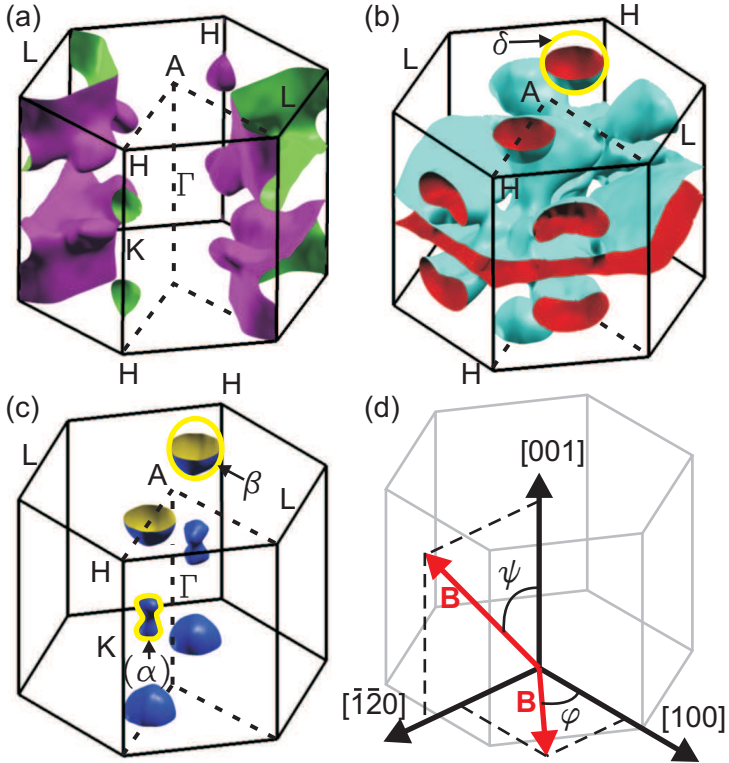


**Figure 6.8.:** (a-c) Fermi surface sheets of  $\text{CrB}_2$  corresponding to the three bands that cross  $E_F$  shown in Fig. 6.7. For clarity, they are plotted separately. (a) The Fermi surface sheet corresponding to the blue band consists of a singly connected structure centered around the L point. It has predominantly Cr- $d$  character. (b) Fermi surface corresponding to the black band. Two ball-shaped, B- $p$  derived Fermi surface pockets are present between the A- and H-points. The extremal orbit  $\delta$  assigned to the experimentally observed dHvA frequency is shown in yellow. The remaining Fermi surface sheets of this band are of Cr- $d$  character. (c) Two ball-shaped and two dumbbell-shaped Fermi surface pockets originate from the orange band in Fig. 6.7. The orbit  $\beta$  is allocated to the ball-shaped pocket as indicated. This pocket is also predominantly B- $p$ -like. The dumbbell-shaped pockets have Cr- $d$  orbital character. The frequency of the  $\alpha$  orbit seen in the experiment matches reasonably well to this pocket (see Table 6.1). In light of the fact that the pocket is of Cr- $d$  orbital character we refrain from a clear assignment (see text). (d) Real-space coordinate system with respect to the orientation of the 1. Brillouin zone.

The calculations suggest an ordered magnetic moment of  $1.3 \mu_B \text{ f.u.}^{-1}$ , while early experiments [Fun77] reported  $0.5 \mu_B$ . Besides, neutron scattering data [Reg] as well as NMR experiments in Ref. [Mic07] show hints of further ordering vectors. The resolution of this discrepancy between experiment and theory is not the topic of this work. However, since this uncertainty could potentially influence the interpretation of our dHvA data, J. Kuneš and L. Chioncel performed additional band structure calculations. Thereby we want to assess to what extent the Fermi surface sheets, which we associate with the experimental orbits, are sensitive to the magnetic order. In particular calculations for the collinear spin state and for nonmagnetic CrB<sub>2</sub> were done (c.f. Appendix A). The general outcome is, that the two different ball-shaped Fermi surface sheets with B-*p* orbital character are quite insensitive to the magnetic order. The main effect in going from the nonmagnetic to the cycloidal order is the lifting of the spin degeneracy and the corresponding shift of the pockets away from the A point along the A-H direction. The changes in shape and size are only minor. In contrast, the remaining Fermi surfaces sheets, which are dominantly of Cr-*d* orbital character, change radically between the cycloidal magnetic, collinear magnetic and non-magnetic calculations, i.e., they are highly sensitive to the type and magnitude of the magnetic order parameter.

### 6.3.3. Extraction of dHvA frequencies and band masses

The SKEAF [Rou12] tool allows us to analyze the Fermi surface of CrB<sub>2</sub> shown in Fig. 6.8 and to extract the dHvA frequencies as well as the band masses from the calculations. In analogy to the experiment, *B*-field orientations within the [100] – [120] plane and within the [001] – [120] plane were considered. In account of that, Fig. 6.8 (d) illustrates the orientation of the real space crystal axes with respect to the orientation of the first Brillouin zone. The SKEAF results are depicted in Fig. 6.9. For clarity, we plot the dHvA frequencies corresponding to the different bands separately, as done in Fig. 6.8. Figure 6.9 (a) and (b) show the dHvA frequencies extracted from the FS sheet depicted in Fig. 6.8 (a). The calculated frequencies range between 13 kT and 25 kT and thus well above the experimentally observed frequencies. The angular dependence of the dHvA frequencies corresponding to the FS sheets derived from the black band (c.f. Fig. 6.8 (b)) is illustrated in Figs. 6.9 (c-d). Only frequencies below 5 kT are shown. Still, a large number of extremal orbits is found due to the

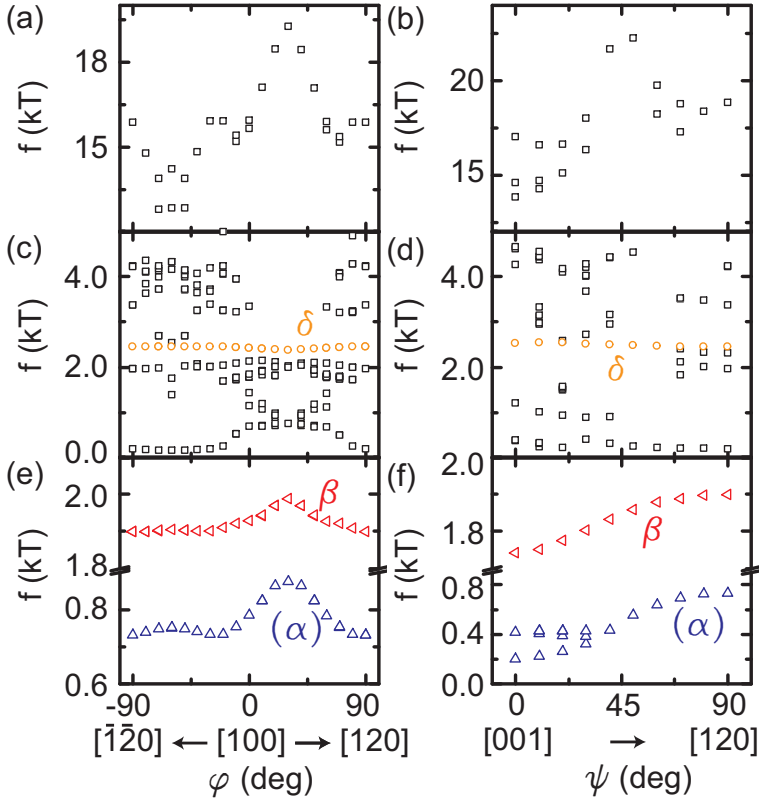


**Figure 6.9.:** Angular dependence of the dHvA frequencies extracted from the band structure calculations using the SKEAF [Rou12] tool. The results of the different FS sheets are plotted separately for clarity (c.f. Fig. 6.8) (a) In plane and (b) out-of-hexagonal plane dHvA frequencies extracted from the calculated FS shown in Fig. 6.8 (a). (c) In plane and (d) out-of-hexagonal plane dHvA frequencies corresponding to the calculated FS shown in Fig. 6.8 (b). Only frequencies below  $f = 5$  kT are shown. Many frequency branches are present. Orbit  $\delta$  is indicated by circular data points. (e) In plane and (f) out-of-hexagonal plane dHvA frequencies corresponding to the calculated FS sheets shown in Fig. 6.8 (c). Two frequency branches are recovered corresponding to the ball-shaped pocket (orbit  $\beta$ , indicated by  $\triangleleft$ ) and to the dumbbell-shaped pocket (indicated by  $\triangle$ ).

complicated structure of the Fermi surface. The frequency branch which corresponds to the B- $p$  derived, ball-like, pockets is highlighted. The frequency is approximately 2.5 kT and its variation is very small for field orientations in both, the  $[100] - [120]$  plane and the  $[001] - [120]$  plane. Further, the topology suggests that it is a closed orbit. Figure 6.9 (e) and (f) show the dHvA frequencies extracted from the FS sheet in Fig. 6.8 (c). Two frequency branches are present. One of them belongs to the ball-shaped pocket ( $\triangleleft$ ) in the range  $1.7 \text{ kT} < f < 2.0 \text{ kT}$ , the other corresponds to the dumbbell-like pocket ( $\triangle$ ) at  $0.2 < f < 0.9 \text{ kT}$ . For field orientations in the hexagonal basal plane (c.f. Fig. 6.9 (e)) we observe a dominating twofold symmetry. Further, a very weak six-fold modulation is present. For magnetic fields oriented in the  $[001] - [120]$  plane (c.f. Fig. 6.9 (f)), both orbits exhibit a single, twofold symmetry. At  $\psi \lesssim 30^\circ$  the frequency branch corresponding to the dumbbell-like pocket ( $\triangle$ ) splits into several branches. This behavior is expected because the dumbbell-like FS sheet exhibits two to three different extremal areas normal to the orientation of the magnetic field at small  $\psi$ .

Further, the SKEAF tool allows to extract the band masses from the DFT calculations for any extremal Fermi surface area. To compare with the experiment, the band masses at  $\varphi = 5^\circ$  were calculated. For the orbits highlighted in Fig. 6.9 (which correspond to the orbits  $\alpha$ ,  $\beta$  and  $\delta$  as shown in the following Sec. 6.4) the frequencies and the effective masses are summarized in Table 6.1. Our experimental results ( $f_{\text{exp}}$ ,  $m^*$  and  $l$ ) are also included therein.

| Orbit                 | $\alpha$        | $\beta$         | $\delta$        |
|-----------------------|-----------------|-----------------|-----------------|
| Band                  | Cr- $d$         | B- $p_{x,y}$    | B- $p_{x,y}$    |
| $f_{\text{calc}}$ (T) | (734)           | 1899            | 2452            |
| $f_{\text{exp}}$ (T)  | 308             | 1608            | 1951            |
| $m^*/m_e$             | $1.22 \pm 0.12$ | $0.86 \pm 0.07$ | $1.07 \pm 0.06$ |
| $m_b/m_e$             | (0.93)          | 0.37            | 0.53            |
| $l$ (nm)              | 26              | 69              | 67              |
| $\lambda$             | (0.3)           | 1.3             | 1.0             |

**Table 6.1.:** Experimental and calculated dHvA frequencies, effective masses  $m^*$ , band masses  $m_b$ , mean free paths  $l$  and electron-phonon coupling constants  $\lambda$ . The calculated values for orbit  $\alpha$  are given in brackets because they refer to the dumbbell-shaped pocket that cannot be assigned unambiguously.

## 6.4. Comparison of experiment and theory

To allocate the three experimentally observed orbits  $\alpha$ ,  $\beta$  and  $\delta$ , we compared them with the calculated FS considering the following criteria: the dHvA frequency and its angular dependence (giving information about size, shape and topology), the charge carrier masses and the exclusiveness (i.e., are there other candidates that might also match, or is the assignment unique?) [Bra13a].

Following these criteria, the experimentally observed orbits  $\beta$  and  $\delta$  were assigned to the two ball-shaped sheets between A and H formed by B- $p$  electrons as listed in Table 6.1 and illustrated in Fig. 6.8 (b-c). This assignment can be made due to

- the good frequency (FS cross section) match,
- the closed-surface topology,
- the nearly spherical shape of the FS sheets in both experiment and calculation,
- the sufficiently light band masses and
- the fact that there are no other Fermi surface sheets that are anywhere close to match these criteria.

In particular, the Cr- $d$  derived sheets look very different, such that even moderate changes in the magnetic order are unlikely to produce similar pockets. In addition, the charge carriers of most Cr- $d$  derived sheets are much too heavy to be resolved under the applied experimental condition. The measured frequencies differ by 300 – 500 T from the calculations. This corresponds to a remaining discrepancy in  $k$ -space extent of only 0.2 to 0.3 % of the Brillouin zone cross sectional area, which represents a good agreement. Rigid band shifts on the order of 100 meV can bring the calculated frequencies of  $\beta$  and  $\delta$  into coincidence with the experimental results. However, the shape of the remaining, Cr- $d$  derived, FS sheets, is heavily affected by the band shift. Besides, we do not have a clear physical picture of the underlying mechanisms and thus the information gained by the band shift is rather limited. In account of these reasons we did not follow such an analysis further.

Details of the Fermi surface shape are also qualitatively reproduced: The nearly ball-shaped pocket giving rise to the  $\beta$  orbit is slightly elongated in the [001] direction in both, experiment and calculation. The very small

sixfold modulation of the  $\beta$  orbit for rotation in the basal plane seen in the experiment (Fig. 6.3 (b)) is already present in the nonmagnetic calculation (c.f. Appendix A). In the cycloidal magnetic calculation, performed for one single domain of the ordering vector, the weak modulation is also present, but a twofold symmetry dominates. However, if we assume that the different domains corresponding to the symmetry related  $\mathbf{q}$ -vectors are equally populated, an apparent sixfold symmetry will be restored, provided that the overlapping frequency branches from the different domains are not spectrally resolved in the FFT. For the observed frequency modulation amplitude of 15 T this condition is fulfilled in the experiment [Bra13a].

The measured frequency and topology of orbit  $\alpha$  match best with the dumbbell-shaped electron pocket along  $\Gamma$ - $K$  shown in Fig. 6.8 (c). It is therefore tempting to tentatively assign  $\alpha$  to this Fermi surface sheet as indicated with ( $\alpha$ ) in Fig. 6.8 (c) and Table 6.1. It is a closed surface and there is no other sheet providing similarly small cross sections on a closed surface. The frequency match is satisfactory. The measured effective mass  $m^*/m_e = 1.22 \pm 0.12$  and the band mass  $m_b/m_e = 0.93$  are in good agreement. However, the observation that the dHvA frequency vanishes in the experiment upon field rotation in the  $\psi$ -direction is not expected for the dumbbell structure. On the contrary, a signal from the neck orbit of the dumbbell would be expected to appear upon rotation about  $\psi$  (c.f. Fig. 6.9 (f)). As noted above, the dumbbell electron pocket has dominantly Cr- $d$  character and its cross section and topology is thus significantly affected by the magnetic order. In account of these arguments we refrain from a definite assignment of the  $\alpha$  orbit to the dumbbell pocket. The calculated values for the  $\alpha$  orbit are given in brackets in Table 6.1 as they refer to the dumbbell pocket that does not support all experimental observations unambiguously.

The calculated Fermi surface of CrB<sub>2</sub> suggests many more possible extremal orbits as seen in Fig. 6.9. All of them arise from Cr- $d$  dominated Fermi surface parts. In most cases, these are either large orbits or orbits with heavy effective mass. Thus, going to lower experiment temperatures and higher magnetic fields might enable their observation.

Comparing the calculated band masses of the charge carriers with the experiment, we find that the quasiparticle masses  $m^*$  are strongly enhanced over the band masses  $m_b$  for the B- $p$  pockets (Table 6.1). We attribute this finding to many-body interactions that are not included in the band structure calculations [Was96]. Assuming that electron-phonon interac-



tion is the dominant source of these interactions in the B- $p$  derived Fermi surface sheets as it is in the isostructural compound  $\text{MgB}_2$ , we calculate an upper bound for the electron-phonon coupling constant  $\lambda$  defined by  $m^* = (1 + \lambda)m_b$  [Car03]. For the orbits  $\beta$  and  $\delta$  the values of  $\lambda$  are relatively large and amounted to 1.3 and 1.0, respectively (Table 6.1). The  $\sigma$ -bonds formed by the  $p_{x,y}$  orbitals in the boron layer (c.f. Fig. 4.2) are very strong and thereby they are probably very sensitive to the B-B bond length. Owing to this characteristics strong electron-phonon coupling in the B- $p$  sheets of  $\text{CrB}_2$  is likely.

## 6.5. Comparison with $\text{MgB}_2$

The comparison of our dHvA experiments with the results from density functional theory proves that parts of the Fermi surface in the itinerant antiferromagnet  $\text{CrB}_2$  derive from bands with clear B- $p$  electron character. More precisely, the B- $p$  states at the Fermi level are dominantly  $p_{x,y}$  states as seen in Fig. A.2. In view of this characteristic it is instructive to compare Fermi surface properties of  $\text{CrB}_2$  with those of the isostructural compound  $\text{MgB}_2$  as detailed in Ref. [Bra13a].  $\text{MgB}_2$  is a conventional high temperature superconductor with  $T_c = 39$  K [Nag01, Cav01, Bud01, Hin01, Pic02]. Band structure calculations and studies of the quantum oscillatory magnetization suggested consistently the existence of two superconducting gaps [Yel02, Car03, Maz02]. The two band superconductivity arises from the  $\sigma$  and  $\pi$  bands formed by the B- $p_{x,y}$  and by the B- $p_z$  electrons, respectively. Interband impurity scattering between both bands is almost absent [Kor01, Maz02]. The B- $p_{x,y}$  derived bands in  $\text{MgB}_2$  exhibit relatively large electron-phonon coupling constants of  $\lambda = 0.96 - 1.2$  [Yel02, Liu01]. The strength of the electron-phonon coupling is thereby directly related to having partially filled  $\sigma$ -bonding B- $p_{x,y}$  states at the Fermi level. Since  $\sigma$  bonds are strong and the B- $p_{x,y}$  states are sensitive to the B-B bond length this leads to a large electron-phonon coupling especially for the cylindrical hole sheets around  $\Gamma$ -A present in the FS of  $\text{MgB}_2$  [Car03, Car07].

Thus, comparing both,  $\text{CrB}_2$  and  $\text{MgB}_2$ , the B- $p$  states at the Fermi level are dominantly B- $p_{x,y}$  states. We determined an upper bound of the electron-phonon coupling constants  $\lambda = 1 - 1.3$  in  $\text{CrB}_2$  which compares well with  $\text{MgB}_2$ . Interestingly, the overall mass enhancements observed in  $\text{CrB}_2$  are comparable to those of  $\text{MgB}_2$ . In addition, the mean free paths extracted

## 6. De Haas-van Alphen effect and Fermi surface properties of $\text{CrB}_2$

---

for  $\text{CrB}_2$  are in good agreement with the corresponding values in  $\text{MgB}_2$  ( $l_{\text{MgB}_2} = 38 - 68 \text{ nm}$  [Car03]). The shape of the  $B$ - $p_{x,y}$  derived Fermi surface sheets in  $\text{CrB}_2$  is, however, in contrast to  $\text{MgB}_2$ . In  $\text{CrB}_2$  closed three-dimensional sheets have been identified (Fig. A.2(c-d)), whereas in  $\text{MgB}_2$  they are cylindrical and open [Car03, Car07].

## 7. Magnetization of a 2DES in a MgZnO/ZnO heterostructure

Having studied the magnetization of a magnetic thin film and of a bulk system in the previous chapters we now turn to the magnetization of a 2DES confined in a MgZnO/ZnO heterostructure. 2DESs formed in GaAs or Si based heterostructures have been intensively studied in the last decades and a profound understanding of their orbital and spin magnetism has been gained. In recent years also oxide heterostructures have attracted tremendous interest [Oht04, Hwa12] because they exhibit remarkable properties such as superconductivity [Rey07], magnetism [Ber11] or the fractional quantum Hall effect (QHE) [Tsu07, Tsu10]. Among them, MgZnO/ZnO based heterostructures are outstanding. The 2DES with small carrier density  $n_s$  formed at MgZnO/ZnO interfaces exhibit extremely high mobilities  $\mu$  at low temperature  $T$  [Tsu07, Tsu10]. At the same time, the electron-electron interaction parameter  $r_s \propto n_s^{-0.5}$  (c.f. Eq. 2.49) is large allowing for electron correlation effects in an applied magnetic field  $B$  [Tsu08, Tsu10, Koz12]. The magnetic properties of oxide heterostructures at high magnetic fields, i.e. the de Haas-van Alphen effect and non-equilibrium currents, have not been investigated so far. This work reports the first experimental observation of the dHvA effect and NECs by means of cantilever magnetometry measurements. The results will be presented in this Chapter. Parts of the results have also been submitted for publication [Bra13b].

The chapter is organized as follows: First, the experimental methods are introduced in Sec. 7.1 before a brief overview of the experimental results is given in Sec. 7.2. In Sec. 7.3 the dHvA effect in MgZnO/ZnO heterostructures is discussed as a function of magnetic field orientation and as a function of temperature. Further, the results are compared with model calculations. Section 7.4 is dedicated to the non-equilibrium phenomena observed in MgZnO/ZnO 2DESs. The magnetic field sweep dependence as well as the temperature dependence of the NECs are discussed. Particu-

lar results of the dHvA effect and of the non-equilibrium effects suggest the existence of an asymmetric density of states (DOS) caused by the presence of repulsive scatterers. This phenomenon will be discussed in Sec. 7.5. Finally we analyze overshoot effects in the magnetization. In the light of the presence of repulsive scatterers we interpret this finding as magnetic thaw down of electrons in Sec. 7.6.

### 7.1. Experimental methods

In this work two samples from different MgZnO/ZnO heterostructures, *zn0257* and *zn0259*, were investigated. Sample *zn0257* was characterized by a high electron density  $n_s = 4.1 \cdot 10^{11} \text{ cm}^{-2}$  and lower mobility  $\mu = 2.9 \cdot 10^5 \text{ cm}^2/\text{Vs}$  in comparison to *zn0259* with  $n_s = 1.7 \cdot 10^{11} \text{ cm}^{-2}$  and  $\mu = 3.8 \cdot 10^5 \text{ cm}^2/\text{Vs}$ . In both cases, the active area  $\mathcal{A}$  of the investigated 2DESs was  $0.9 \times 1.8 \text{ mm}^2$ . Further sample details were introduced in Chapter 4.

For the magnetization studies on sample *zn0257* we used a fiber-optical readout technique, which is described in Refs. [Spr06, Ruh06]. The experiment was performed with GaAs based cantilevers in a  $^3\text{He}$  cryostat allowing magnetic fields up to 14 T and temperatures down to 0.28 K. The angle between  $\mathbf{M}$  and  $\mathbf{B}$ , which is denoted in the inset of Fig. 7.1 (a), was set to  $\alpha = 15^\circ$ .

The experiments on the *zn0259* sample were performed with the capacitive readout technique, which was presented in detail in Chapter 3. GaAs based cantilevers were used. The experimental geometry is sketched in the inset of Fig. 7.1 (a). The measurements were performed in a  $^3\text{He}$  cryostat that allows temperatures down to 0.28 K. Two sets of experiments were done. First, the measurements were conducted in a vector magnet system as described in Chapter 3. Within one cooldown cycle we investigated the 2DES in the angular regime  $36.8^\circ \leq \alpha \leq 67.0^\circ$ . Second, in order to investigate the behavior also at high magnetic fields, we inserted the sample into an axial magnet system allowing 14 T in a subsequent cooldown. Here, data was acquired at two fixed angles  $\alpha = 36.8^\circ$  and  $\alpha = 52^\circ$ .

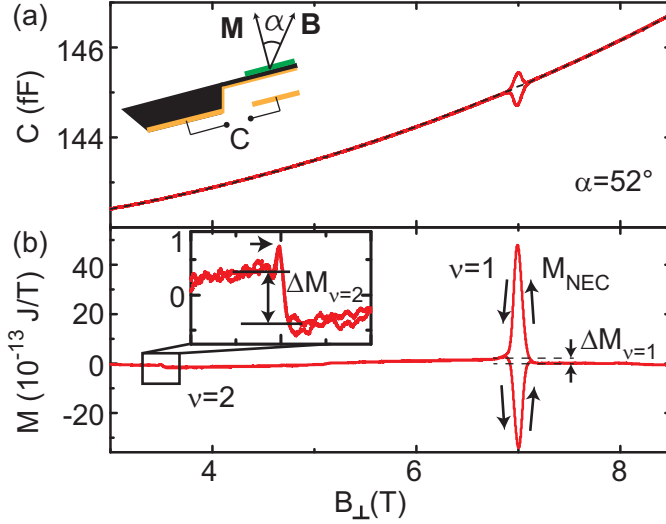


**Figure 7.1:** (a) Capacitance raw data as a function of  $B_{\perp}$  of the MgZnO/ZnO heterostructure sample *zn0259*, at  $T = 0.28$  K and  $\alpha = 52^{\circ}$ . The inset displays a sideview of the experimental geometry. The magnetic background signal (dashed line) is subtracted to give the oscillatory magnetization shown in (b). At  $\nu = 1$ , the data exhibits the dHvA effect as well as NECs, which change sign upon changing the sweep direction (arrows). The inset shows a blow-up of the dHvA effect at  $\nu = 2$  for the field range  $3.0 \text{ T} < B < 4.0 \text{ T}$ . An overshoot of the dHvA signal is observed (marked by the horizontal arrow). NECs are absent at  $\nu = 2$ .

## 7.2. Experimental results: Overview

We first focus on the experimental results of sample *zn0259* obtained in the 14 T magnet system. The raw capacitance data as a function of  $B_{\perp} = B \cos \alpha$  at  $T = 0.28$  K and  $\alpha = 52^{\circ}$  is depicted in Fig.7.1 (a). The magnetic quantum oscillations are superimposed on a smoothly varying magnetic background. A low-order polynomial was fitted in  $B$  (denoted by the dashed line) and subtracted from the raw data. Applying the calibration routine described in Sec. 3.2 the oscillatory magnetic signal is obtained as shown in Fig. 7.1 (b). The data clearly exhibits the dHvA effect, as jumps  $\Delta M$  in the magnetization occur at  $\nu = 1$  and  $\nu = 2$ . In addition we ob-

serve signatures arising from NECs at  $\nu = 1$ . They can be distinguished from the dHvA effect since there is a sign change in  $M_{\text{NEC}}$  upon changing the magnetic field sweep direction [Ush09, Sch03]. Finally, there are spike-like overshoots of the dHvA effect present at  $\nu = 2$  (denoted by the horizontal arrow in the inset of Fig. 7.1 (b)). They can be neither described by the NECs nor can they be understood in terms of the dHvA effect. In the following sections, these three observations of sample *zn0259* will be analyzed and discussed.

In sample *zn0257*, neither the dHvA effect nor NECs were observed, irrespective of the measurement temperature. Reasons for their absence are unclear. However, one may speculate about possible origins: First, the size of the respective signal may be much smaller compared to *zn0259*, due to the different heterostructure characteristics. Second, we applied the optical readout technique for the investigation of sample *zn0257*. It might be possible that the application of laser light during the measurements, which is necessary for the optical readout, obscures the dHvA effect or the non-equilibrium currents in the MgZnO/ZnO heterostructure. Further clarification via reference experiments is necessary. The measurement results of sample *zn0257* will not be discussed further in the following.

### 7.3. De Haas-van Alphen effect

In this section the dHvA effect in MgZnO/ZnO is discussed. First, results from angular dependent and temperature dependent measurements are presented in Sec. 7.3.1 and Sec. 7.3.2, respectively. The experimental data is compared with model calculations. This analysis is followed by a discussion of the angular dependent behavior of the dHvA effect and of the observed enhancements of the dHvA oscillations amplitudes at even and odd filling factors in Sec. 7.3.3.

#### 7.3.1. Angular dependence

In Fig. 7.2 (a) and (b)  $M$  is plotted as a function of  $B_{\perp}$  near  $\nu = 3$  and near  $\nu = 2$ , respectively. Datasets for different tilt angles as denoted in the figures were obtained at  $T = 0.28$  K. For clarity, only one sweep direction is shown and the curves are shifted in vertical direction. The jumps in  $M$

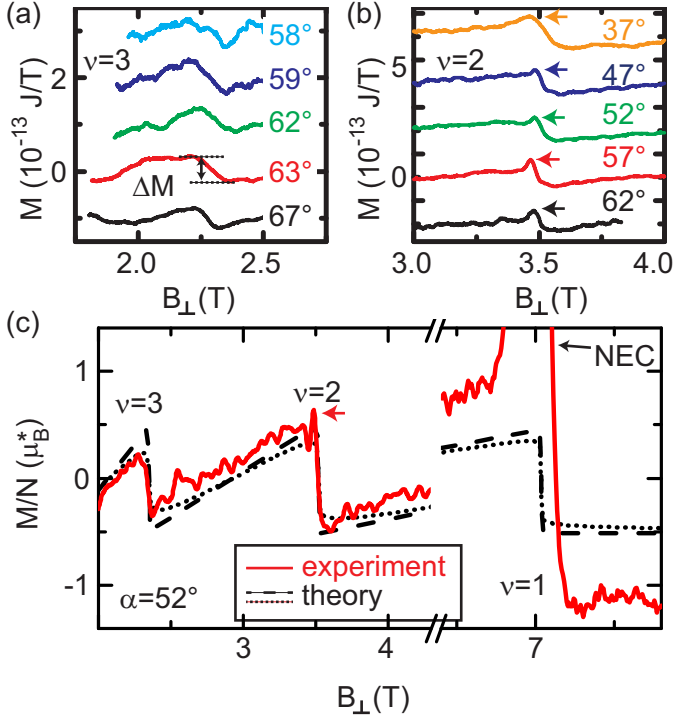


**Figure 7.2.:** Angular dependence of  $M(B_{\perp})$  near (a)  $\nu = 3$  and (b)  $\nu = 2$ . Curves are shifted in vertical direction for clarity. The peak-to-peak dHvA amplitude  $\Delta M$  is denoted. At  $\nu = 2$  we observe an overshoot of  $\Delta M$  for all measured angles marked by the horizontal arrows. This overshoot is not considered in the evaluation of  $\Delta M$ . (c) Experimental data (line) at  $\alpha = 52^\circ$  and  $T = 0.28 \text{ K}$  along with model calculations (dashed and dotted line) normalized per electron via  $M_e = M/(n_s A)$ . The behavior of an ideal 2DES ( $T = 0$ ,  $\Lambda = 0$ ) is depicted by the dashed line. The calculation for a real 2DES at  $T = 0.28 \text{ K}$  and  $\Lambda = 0.05 \text{ meV}/\sqrt{T} \times \sqrt{B_{\perp}}$  is represented by the dotted line. At  $\nu = 3$ , experimental data and calculations for a real 2DES match well. At  $\nu = 2$ , the dHvA amplitude  $\Delta M$  is approximated very well by an ideal 2DES.  $\Delta M$  is enhanced over the expected dHvA amplitude at  $\nu = 1$ , where large NECs are superimposed on the experimental data.

at  $\nu = 3$  appear at  $B_{\perp} \approx 2.3$  T, the position of  $\nu = 2$  is at  $B_{\perp} \approx 3.5$  T. Thus, according to  $\nu = \hbar n_s / (eB_{\perp})$ ,  $n_s$  amounts to  $1.7 \times 10^{11} \text{ cm}^{-2}$ , which is in perfect agreement with the value determined by prior transport characterization on a reference 2DES. The data enables us to determine the peak-to-peak dHvA amplitude  $\Delta M$  as denoted in Fig. 7.2 (a). Non-equilibrium phenomena are absent at  $\nu = 3$  and  $\nu = 2$ . Instead we observe an overshoot of the dHvA effect at  $\nu = 2$  for all angles. Please note that the overshoot is not dependent on the field sweep direction.

Measurement results obtained in the high field magnet at  $\alpha = 52^\circ$  are shown in Fig. 7.2 (c). Here we plot the magnetization per electron given by  $M_e = M / (n_s A)$ . The data is presented in units of the effective Bohr magneton  $\mu_B^* = \mu_B (m_e / m^*)$  considering an effective mass of  $m^* = 0.31 m_e$  (see Sec. 7.3.2). Apart from  $\nu = 2, 3$  we also observe the dHvA effect at  $\nu = 1$  at  $B_{\perp} \approx 7$  T in the high field magnet. However, a large signal arising from NECs is superimposed on the dHvA oscillation.

From the angular dependencies of the dHvA amplitudes shown in Fig. 7.2 we extract the normalized dHvA amplitude per electron  $\Delta M_{e,\nu} = \Delta M_{\nu} / (n_s A)$ . Fig. 7.3 (a) summarizes  $\Delta M_{e,\nu}$  in units of  $\mu_B^*$  for  $\nu = 1$  to 3. Analyzing  $\nu = 2$ , where spin polarization is absent, we find that  $\Delta M_{e,\nu=2}$  varies from 1.3 to  $0.78 \mu_B^*$  in the angular regime from  $\alpha = 36.8^\circ$  to  $62.0^\circ$  (triangles).  $\Delta M_{e,\nu=2}$  seems to decrease with increasing  $\alpha$ . The corresponding thermodynamic energy gaps  $\Delta E_{\nu=2} = \Delta M_{e,\nu=2} \cdot B$  are depicted in Fig. 7.3 (b).  $\Delta E_{\nu=2}$  ranges from 0.82 to 0.61 meV in the angular regime studied. For an ideal (disorder-free), non-interacting 2DES the energy gap at  $\nu = 2$  should amount to  $\Delta E_{\nu=2} = \hbar\omega_c - g\mu_B B$  (c.f. Sec. 2.2.4). The line in Fig. 7.3 (b) denotes the calculated energy gap for the ideal 2DES. The band structure Landé factor  $g = 1.93$  for ZnO [Tam08] was considered here. The experimentally determined values for  $\Delta E_{\nu=2}$  are in good quantitative agreement with the predicted values.

Turning towards the spin filling factors,  $\Delta M_{e,\nu=3}$  is in the range of 0.45 to  $0.80 \mu_B^*$  in the angular regime from  $\alpha = 52.0^\circ$  to  $67.0^\circ$ . The corresponding energy gaps displayed in Fig. 7.3 (b) (squares) take values from 0.20 to 0.34 meV. Regarding  $\nu = 1$ ,  $\Delta M_{e,\nu=1}$  amounts to  $2.0 \mu_B^*$  at  $\alpha = 36.8^\circ$  and  $2.3 \mu_B^*$  at  $\alpha = 52.0^\circ$ . The energy gaps are 2.5 meV and 2.9 meV, respectively.

From the energy gaps at odd filling factors, we extract the Zeeman splitting  $\Delta E_Z = |g^*| \mu_B B$ . The effective Landé factor  $g^*$  is used to parametrize the magnetism of the spin splitting. From the data shown in Fig. 7.3 (b) we



extract a maximum  $g^* = 1.1$  for  $\nu = 3$ . This value is reduced compared to the band structure  $g$  factor of ZnO. For  $\nu = 1$ , we find a maximum  $g^*$  of 5.1 at  $\alpha = 36.8^\circ$ . This value is significantly enhanced over  $g = 1.93$ . It is well known that  $g^*$  can be enhanced when approaching the quantum limit, i.e. in large fields  $B$  (see Sec. 2.2.4).

Model calculations, which were introduced in Sec. 2.2.4, were applied to compare the experimental magnetization curves with theory and to illustrate the respective discrepancies. Further they are helpful to perform a more detailed and quantitative analysis regarding the curve shape and the dHvA amplitudes  $\Delta M_\nu$ . A single-particle DOS with Gaussian-broadened Landau levels

$$D(E) = \frac{eB_\perp}{h} \sum_{j=0}^{\infty} \frac{1}{\sqrt{2\pi}\Lambda} \exp\left[-\frac{(E - E_{j,s})^2}{2\Lambda^2}\right] \quad (7.1)$$

was assumed [Wil08].  $\Lambda$  accounts for the level broadening. According to Ref. [And74a]  $\Lambda$  can be expressed as  $\Lambda = \frac{e\hbar}{m^*} \sqrt{2/\pi\mu} \sqrt{B_\perp}$ . It amounts to  $5 \times 10^{-2} \sqrt{B_\perp}$  meV/ $\sqrt{T}$  for the investigated heterostructure.

Along with the experimental data, Fig. 7.2 (c) shows simulated magnetization traces (dashed and dotted line). In the calculations the band structure Landé factor  $g = 1.93$  [Tam08] was used. The dashed curve depicts the magnetization trace of an ideal, disorder-free 2DES, i.e. at  $T = 0$  and considering delta-like Landau levels. A real 2DES, taking finite temperature ( $T = 0.28$  K) and finite level broadening ( $\Lambda = 5 \times 10^{-2} \sqrt{B_\perp}$  meV/ $\sqrt{T}$ ) into account, is given by the dotted curve.

The shape of the experimental  $M_e(B_\perp)$  curve does not resemble the sawtooth predicted for an ideal, i.e., disorder-free 2DES at  $T = 0$  K. Instead we observe a finite slope in  $M_e(B_\perp)$  at  $\nu = 2$  and  $\nu = 3$ , which is reproduced satisfactorily in the model calculations with finite  $\Lambda$  and  $T$ . Regarding the dHvA amplitudes, neither the calculation assuming an ideal 2DES nor the one for the real 2DES is able to model the experimental data in its entirety. At  $\nu = 3$ ,  $\Delta M_e$  is in good agreement with the simulation for the real 2DES. Going to  $\nu = 2$ , the dHvA amplitude is in better quantitative agreement with the model calculations assuming an ideal 2DES. The calculations for the real 2DES, however, underestimates the gap. At  $\nu = 1$ , the experimental value  $\Delta M_e$  is obviously enhanced over the simulated dHvA amplitudes.

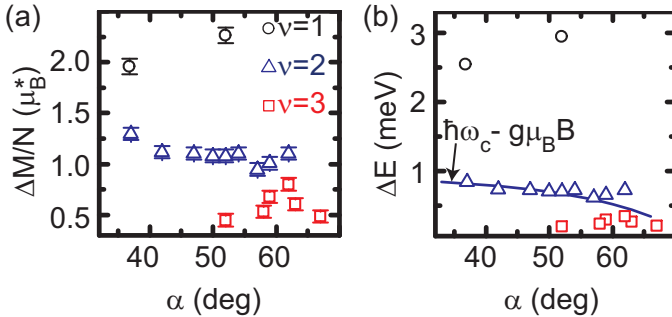


**Figure 7.3.:** (a) DHvA amplitudes per electron  $\Delta M_{e,\nu} = \Delta M_\nu / (n_s \mathcal{A})$  as a function of  $\alpha$ . (b) Thermodynamic energy gaps  $\Delta E_\nu$  as a function of  $\alpha$ . The solid line denotes the energy gap expected for  $\nu = 2$  in a disorder-free 2DES at  $T = 0$ .

### 7.3.2. Temperature dependence of energy gaps

In this section we show results from temperature dependent measurements. During the experiments, the temperature was monitored with a calibrated *Cernox* temperature sensor which was attached to the sample stage. The temperature dependence of  $\Delta M_{\nu=2}$  and  $\Delta M_{\nu=3}$  was investigated at  $\alpha = 62.0^\circ$ , the one of  $\Delta M_{\nu=1}$  at  $\alpha = 36.8^\circ$ .

In Fig. 7.4 (a)  $M(B_\perp)$  near  $\nu = 2$  is shown for temperatures ranging from 0.28 K (top curve) to 1.6 K (bottom curve). The curves are shifted in vertical direction for clarity.  $\Delta M_{\nu=2}$  decreases with increasing temperature and the curvature becomes smoother. Going from higher to lower temperatures, the field position of  $\nu = 2$ , i.e. the position of the steepest slope, moves towards higher fields. The position of the steepest slope at  $T = 0.28$  K and at  $T = 1.6$  K are indicated by the dashed line.  $\Delta B_{\text{eq}}$  denotes the shift. Further, we observe an anomalous overshoot of the dHvA amplitude at  $T = 0.28$  K as denoted by the horizontal arrow. At elevated temperatures, the overshoot is absent. The latter two observations will be discussed in Sec. 7.5.

The corresponding normalized dHvA amplitudes, i.e.  $\Delta M_{\nu=2}(T) / \Delta M_{\nu=2}(T = 0.28 \text{ K})$ , are plotted in Fig. 7.4 (b). A smooth decrease of  $\Delta M_\nu$  is found as the temperature increases. The respective uncertainties in reading off  $\Delta M_\nu$  are denoted by the error bars.

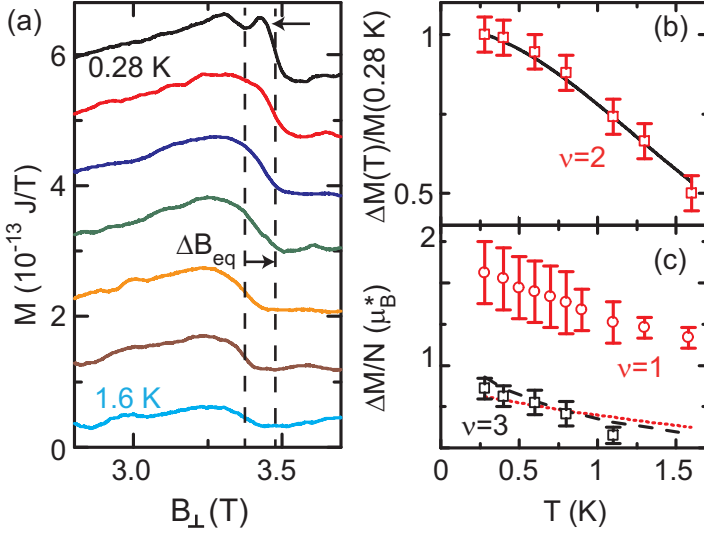


**Figure 7.4.:** (a) Temperature dependence of  $M(B_{\perp})$  at  $\nu = 2$  and  $\alpha = 62.0^{\circ}$ . From top to bottom, the temperature was set to  $T = 0.28$  K,  $T = 0.40$  K,  $T = 0.60$  K,  $T = 0.80$  K,  $T = 1.1$  K,  $T = 1.3$  K and to  $T = 1.6$  K. Going from higher to lower  $T$ , the field position of  $\nu = 2$  moves towards larger magnetic fields. We denote this shift by  $\Delta B_{\text{eq}}$ , where we take the position of  $\nu = 2$  at  $T = 1.6$  K as reference. Exemplarily, the dashed lines denote the field position of  $\nu = 2$  at  $T = 0.28$  K and  $T = 1.6$  K, respectively. (b) Normalized dHvA amplitudes for  $\nu = 2$  at  $\alpha = 62.0^{\circ}$  as a function of  $T$  (data points). Error bars denote the uncertainty in reading off  $\Delta M_{\nu=2}$ . The LK fit (line) yields an effective mass of  $m^* = 0.31 \pm 0.01 m_e$ . (c) DHvA amplitudes per electron at spin filling factors (data points) as a function of  $T$ . The dashed and dotted lines are obtained from model calculations at  $\nu = 3$  and  $\nu = 1$ , respectively. Considering  $\nu = 1$ , the experimental values are larger than the calculated ones. We attribute this to exchange enhancement.

We analyze the data using the Lifshitz-Kosevich (LK) formalism (c.f. Sec. 2.2.3). According to the LK formula,  $\Delta M(T)$  can be expressed as

$$\Delta M(T) = M_0 \frac{X}{\sinh(X)}, \quad X = \left( \frac{2\pi^2 k_B m^* T}{\hbar e B} \right). \quad (7.2)$$

Further, we assume that  $\Delta M(T = 0.28 \text{ K})$  is the low temperature saturation value so that we can replace  $M_0$  by  $\Delta M(T = 0.28 \text{ K})$  in Eq. 7.2. Fitting Eq. 7.2 to the data allows us to extract  $m^*$  as the free fitting parameter. We obtain  $m^* = 0.31 \pm 0.01 m_e$ . This value is in good agreement with values reported in the literature [Tsu08, Koz12, Kas12].

The temperature dependence of the dHvA amplitudes at odd filling factors is depicted in Fig. 7.4 (c). Note, that the temperature dependent measurements for each filling factor were performed at different angles, i.e.  $\Delta M_{\nu=3}(T)$  was determined at  $\alpha = 62^\circ$  and  $\Delta M_{\nu=1}(T)$  at  $\alpha = 36.8^\circ$ . In both cases,  $\Delta M(T)$  decreases with increasing temperature.  $\Delta M_{\nu=3}(T)$  could not be traced over the whole temperature regime. This behavior is attributed to the level broadening at elevated temperatures which smears out the dHvA oscillations. At  $\nu = 1$ , large signals arising from NECs were superimposed on the dHvA effect as shown in Fig. 7.1. Owing to this feature, the uncertainty in reading off  $\Delta M_{\nu=1}$  is relatively large compared to the other filling factors. The respective uncertainties are denoted by error bars. The dashed line shows the numerically calculated temperature dependence of  $\nu = 3$  considering  $g^* = 1.93$  and  $\Lambda = 5 \times 10^{-2} \sqrt{B_\perp} \text{ meV}/\sqrt{\text{T}}$ . The experimental values are systematically smaller than the calculated ones, but the relative trend is comparable. We also calculated the temperature dependence of  $\nu = 1$  expected for  $g^* = 1.93$  and  $\Lambda = 5 \times 10^{-2} \sqrt{B_\perp} \text{ meV}/\sqrt{\text{T}}$ . The result is denoted by the dotted line. The experimentally observed dHvA amplitudes are clearly enhanced over the calculated ones within the whole temperature range. Please note that due to the different  $\alpha$  the calculated values for  $\Delta M_{\nu=1}$  are smaller than for  $\Delta M_{\nu=3}$  at  $T \lesssim 0.8 \text{ K}$ , which may be counterintuitive at first glance.

### 7.3.3. Discussion

#### Angular dependence

We first turn to the angular dependence of the thermodynamic energy gaps which was described in Sec. 7.3.1. Earlier transport experiments performed on MgZnO/ZnO heterostructures with comparable  $r_s$  parameter revealed coincidence phenomena in tilted magnetic fields [Tsu08, Koz12]. The condition for coincidence is that the Landau level splitting  $\Delta E_L = \hbar\omega_c$  equals the Zeeman splitting  $\Delta E_Z = g^* \mu_B B$ . As  $\omega_c \propto B \cos \alpha$  this condition is met for certain angles given by  $\cos \alpha = g^* m^* / (2m_e i)$ , the so-called coincidence angles. Here,  $i$  denotes an integer value. The coincidence condition manifests itself in the dHvA effect in that the thermodynamic energy gap  $\Delta E_\nu = \Delta M_{e,\nu} B_\perp$  and correspondingly  $\Delta M_{e,\nu}$  vanishes. The experimentally obtained values for  $\Delta E_\nu$  are displayed in Fig. 7.3 (b). In the experiment, we were limited to angles below  $\alpha = 67^\circ$ . In this angular regime, we did not observe a disappearance of  $\Delta E_{\nu=2}$  or  $\Delta E_{\nu=3}$ . Thus, we conclude that coincidences are absent in the angular regime studied.

However, neglecting the data point at  $\alpha = 62^\circ$ ,  $\Delta E_{\nu=2}$  shows a decreasing trend with increasing  $\alpha$  as mentioned in Sec. 7.3.1. If we extrapolate values of  $\Delta E_{\nu=2}$  to larger angles, one might speculate that  $\Delta E_{\nu=2}$  would disappear between  $70^\circ$  and  $80^\circ$ . According to the coincidence condition the first coincidence is expected at  $\alpha = 72.6^\circ$ . Here we used the band structure Landé factor  $g = 1.93$  [Rey65] and  $m^* = 0.31 m_e$ . Thus, our experimental results are in reasonable agreement with this prediction. Further, we infer from this discussion that  $g^*$  is not significantly enhanced at  $\nu = 2$ . This result is in line with the theory of an oscillating  $g^*$  factor [And74a], that predicts  $g^* = g = 1.93$  at even filling factors.

#### Energy gaps at spin filling factors

The energy gaps at spin filling factors as a function of  $\alpha$  are summarized in Fig. 7.3 (b). First, we focus on the gap at  $\nu = 3$ . From the data we extracted a maximum  $g^*$  of 1.1. This value is reduced compared to the band structure Landé factor  $g = 1.93$  of ZnO. Model calculations including finite level broadening  $\Lambda = 5 \times 10^{-2} \sqrt{B_\perp}$  meV/ $\sqrt{\text{T}}$  and finite temperature shown in Fig. 7.2 (c) reproduce the shape and amplitude of the dHvA oscillation at  $\nu = 3$  very well. Thus, we attribute the reduction of the  $g^*$

factor to the level broadening and finite temperature effects.

Turning to  $\nu = 1$ , the energy gap is enhanced and we find a maximum  $g^*$  of 5.1 at  $\alpha = 36.8^\circ$ . This value is slightly smaller than the one reported in Ref. [Koz12], where  $g^* = 7.28$  was found by addressing excited states in a transport experiment on a sample with comparable  $r_s$  parameter. In addition, we also observed the enhancement of  $\Delta M_{\nu=1}$  over a broad temperature regime as indicated in Fig. 7.4 (c). The enhancement of the spin splitting has often been observed in high mobility 2DES [Nic88, Gol90] and is commonly attributed to the exchange interaction  $E_{\text{Ex}}$  [Mac86, Eng82]. It is given by

$$\Delta E_Z = |g| \mu_B B + E_{\text{Ex}} = |g^*| \mu_B B. \quad (7.3)$$

The relevant energy for the exchange interaction is the Coulomb energy  $E_C = \frac{e^2}{4\pi\epsilon_0\epsilon_r l_B}$  as introduced in Sec. 2.2.4. We therefore conclude that strong Coulomb type interaction effects are present and alter the ground state energy spectrum of the MgZnO/ZnO heterostructure. As a consequence, the energy gap at  $\nu = 1$  is enhanced by a factor of  $\sim 2.5$ .

### Energy gap at $\nu = 2$

Regarding energy gaps at even filling factors in high mobility 2DESs, their enhancement was predicted theoretically by (screened) Hartree-Fock calculations [Mac86, Man97, Gud00]. Experimentally, however, this effect was observed only rarely in GaAs based heterostructures [Hay92, Mei01, Sch02, Wil04b]. The dHvA oscillation at  $\nu = 2$  and  $\alpha = 52^\circ$  is depicted in Fig. 7.2 (c), which includes the experimentally observed  $M(B)$  curve along with model calculations. The calculated dHvA amplitudes which incorporate the effect of disorder and finite temperature, are systematically smaller than the measured ones at  $\nu = 2$ . In spite of the disorder, which apparently reduces  $\Delta M$ ,  $\Delta M_{\nu=2}$  is close to the value predicted for an ideal, disorder-free 2DES with non-interacting electrons. In addition, the angular dependence of the measured energy gaps at  $\nu = 2$  shown in Fig. 7.3 (b) also follows closely the line expected for an ideal 2DES. From these observations we conclude that exchange enhancement renormalizes the energy gap at  $\nu = 2$  in the MgZnO/ZnO heterostructure as well. Moreover, the enhancement of the energy gap at  $\nu = 2$  counteracts the reduction of this energy gap by disorder and finite temperature. Thereby the energy gap at  $\nu = 2$  is close to the value expected for an ideal 2DES.

All in all, our dHvA experiment substantiates that electron-electron interactions play an important role in the magnetic field dependent ground state properties of the MgZnO/ZnO heterostructure at both even and odd integer filling factors.

## 7.4. Non-equilibrium currents

This section focuses on the non-equilibrium magnetization of the MgZnO/ZnO 2DES. The circulating currents are induced when subjecting the 2DES to a time varying magnetic field [Jon95]. In the investigated MgZnO/ZnO 2DES, NECs have only been observed near  $\nu = 1$ . At larger filling factors, NECs were not resolved. Figure 7.1 depicts the magnetization signal stemming from NECs at  $T = 0.28$  K and  $\alpha = 52.0^\circ$ . Figure 7.5 shows the result for  $\alpha = 36.8^\circ$ . The data reveals that the NECs for up- and downsweeps of the magnetic field are asymmetric in terms of the maximum peak height of the magnetization signal.  $M_{\text{NEC}}^{\text{d}}$  ( $M_{\text{NEC}}^{\text{u}}$ ) defines the absolute value of the NEC maximum (minimum) observed in a downsweep (upsweep) of the magnetic field. It is indicated in Fig. 7.5. The signal  $M_{\text{NEC}}^{\text{d}}$  arising from downsweeps is larger than  $M_{\text{NEC}}^{\text{u}}$  obtained during an up-sweep of the magnetic field. In addition, the overall signal shape also differs for up- and downsweep. For the analysis in the following sections we average the NEC signals between both sweep directions to obtain  $M_{\text{NEC}} = (M_{\text{NEC}}^{\text{d}} + M_{\text{NEC}}^{\text{u}}) / 2$  [Smi12]. We start by discussing the sweep-rate dependence of the NECs and the associated QHE breakdown in Sec. 7.4.1. After that we focus on the decay of the induced currents and determine the resistivity  $\rho_{\text{xx}}$  of MgZnO/ZnO based 2DES in the quantum Hall state. Finally the temperature dependent behavior is investigated in Sec. 7.4.3.

### 7.4.1. Sweep-rate dependence of NECs - Quantum Hall effect breakdown

In this section we investigate the dependence of the magnitude of  $M_{\text{NEC}}$  on the field sweep-rate. Therefore we measured  $M_{\text{NEC}}$  as a function of different sweep-rates  $\frac{dB}{dt}$  ranging from 0.02 T/min to 0.40 T/min at  $T = 0.28$  K. The proportionality between induced magnetic moment  $M_{\text{NEC}}$  and circulating non-equilibrium current  $I$  is given by  $M_{\text{NEC}} = I\mathcal{A}$ , where  $\mathcal{A}$  denotes

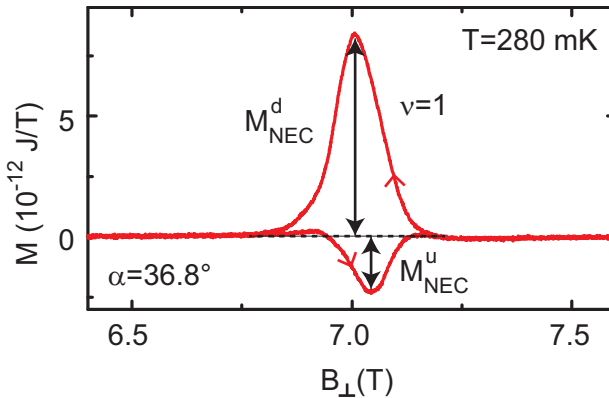


**Figure 7.5.:** NECs in the MgZnO/ZnO heterostructure at  $\alpha = 36.8^\circ$  and  $T = 0.28$  K. The peak height signal and the overall shape of up- and downsweep is not symmetric. For the analysis an averaged signal  $M_{\text{NEC}} = (M_{\text{NEC}}^{\text{d}} + M_{\text{NEC}}^{\text{u}}) / 2$  is used.

the 2DES area. Here, we assume that the current flows around the perimeter of the sample. The currents are generated by an electromotive force  $\varepsilon$  that depends on the field sweep rate via  $\varepsilon = |\mathcal{A} \cos \alpha \frac{dB}{dt}|$ . Figure 7.6 shows  $I$  as a function of  $\varepsilon$ . Two regimes can be distinguished: Initially the induced current increases linearly with the electromotive force as indicated by the linear fit (dashed line). The fit yields the slope  $\Delta I / \Delta \varepsilon = 5.7 \times 10^2$  A/V. In Ref. [Ush09] a simple model was introduced to estimate the corresponding resistivity  $\rho_{\text{xx}}$  of the 2DES [Jon95] in this regime. The induced current in a rectangular sample is given by

$$\Delta I = \frac{1}{\rho_{\text{xx}}} \frac{\Delta \varepsilon}{12 \mathcal{A} \cos \alpha} (a^2 + b^2), \quad (7.4)$$

where  $a$  and  $b$  denote the length and the width of the sample.  $\mathcal{A}$  is the sample area  $a \times b$ . Inserting  $a = 0.9$  mm and  $b = 1.8$  mm we can calculate  $\rho_{\text{xx}}$ . Thus we obtain  $\rho_{\text{xx}} \approx 5 \times 10^{-4} \Omega / \square$ , which is the resistivity of the "zero-resistance" QHE state. For comparison, in related experiments on GaAs based 2DESs resistivities on the same order of magnitude were found [Ush09]. From this result we infer that the properties of the QHE state in the MgZnO/ZnO 2DES are comparable to the ones of GaAs based



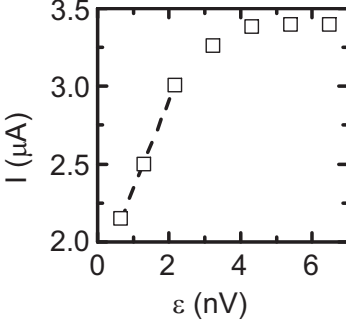


**Figure 7.6.:** Sweep-rate dependence of  $M_{\text{NEC}}$  at  $T = 0.28$  K and  $\alpha = 36.8^\circ$ . The circulating current  $I$  is plotted as a function of the electromotive force  $\varepsilon$ . Initially the curve increases linearly as indicated by the linear fit (dashed line). At large  $\varepsilon$  the curve saturates indicating the QHE breakdown.

systems. This finding is another indication for the high quality of the oxide based 2DES.

After the initial increase the curve saturates at  $\varepsilon \approx 5$  nV. The saturation current  $I_s$  amounts to  $3.4 \mu\text{A}$ . Those characteristics, the initial linear increase together with the saturation at large  $\varepsilon$ , have also been observed in GaAs based heterostructures [Ush09, Smi12]. The fact that  $I$  saturates at large  $\varepsilon$  indicates the high-current breakdown of the quantum Hall effect [Jon96]. This breakdown occurs when the current density exceeds a critical value  $j_c$  causing a sharp increase in  $\rho_{xx}$  away from its dissipationless state. In the single particle edge-state picture the circulating current is confined to a small stripe of width  $l_B = \sqrt{\hbar/eB}$  away from sample edges [Büt88, Jon96]. Along this line we calculate an upper bound for the critical current density by  $j_c = I_s/l_B$  which amounts to  $4 \times 10^3$  A/m. However, according to Ref. [Nac99], the single particle picture underestimates the width of the conductance channel. A more realistic scenario is reported in Refs. [Nac99, Fon91]. Here, the authors claim that the channel width can be well approximated by  $\zeta = \frac{l_B^2}{\pi a^*}$ , where  $a^* = 14 \times 10^{-10}$  denotes the effective Bohr radius calculated for ZnO. Using the relationship  $j_c = I_s/\zeta$  we obtain a critical current density of approximately  $10^2$  A/m. For comparison, in GaAs based 2DES the typical breakdown current densities are on the order of 1 A/m [Nac99]. Thus our measurements suggest breakdown current densities in MgZnO/ZnO based 2DES which are by a factor of 100 larger compared to GaAs based 2DES.

### 7.4.2. Decay of the induced currents

When the magnetic field sweep is stopped abruptly at the center of the NEC signal, the current and thus the magnetic moment do not drop abruptly to zero but the current persists [Jon95, Haa84]. In order to investigate this behavior in MgZnO/ZnO heterostructures, we measured the decay of the NEC at  $\nu = 1$ . A current is induced by sweeping the magnetic field, i.e. by an electromotive force  $\varepsilon$ , at  $T = 0.28$  K. The magnetic field sweep is then stopped at the center of the NEC signal, here at  $B_{\perp} = 7$  T in case of a downsweep, and maintained for the duration of the experiment. We record the magnetic moment as a function of time which allows us to determine the decay time of the induced current. Results for up- and downsweeps of the magnetic field are consistent and we therefore focus here on the decay of the current induced during a downsweep. The results obtained with two different, initial electromotive forces  $\varepsilon \approx 2$  nV and  $\varepsilon \approx 7$  nV, are shown in Fig. 7.7 as open symbols. Please note that the upper curve is shifted by  $4 \mu\text{A}$  for clarity. Both curves initially decrease rapidly with increasing  $t$  while the decrease levels off at larger  $t$ . The current decay induced by  $\varepsilon \approx 2$  nV (upper curve) can be best fitted by a single exponential decay of the form  $I = C_1 \exp(t/t_2)$  (line). The decay time  $t_2$  amounts to 54 s. In contrast, for the lower curve a single exponential fit does not give satisfactory results because the initial current decay for  $t \lesssim 20$  s is too fast. Accordingly, the data is fitted by a sum of two exponential decays of the form  $I = C_1 \exp(t/t_1) + C_2 \exp(t/t_2)$  (line). From the fit we obtain the characteristic decay times  $t_1 = 15$  s and  $t_2 = 61$  s.

The model introduced in Eq. 7.4 fails to describe the persistence of the NECs. In Refs. [Ker07, Ush09] the authors proposed the following mechanism for the current decay. In response to a sweeping magnetic field circulating currents are induced. As a result a Hall electric field is built up between the edge and the center of the 2DES (c.f. Sec. 2.3). Thereby energy is stored capacitively between sample edge and sample center. When the magnetic field sweep is stopped, a charge equalization process is initiated. This process is accompanied by scattering processes giving rise to an exponential decay of the circulating currents.

We first consider the decay curve obtained with  $\varepsilon \approx 7$  nV. Here, we can distinguish between two decay regimes: an initial fast decay and a long lasting smooth decay. According to Fig. 7.6 the electromotive force is large enough such that QHE breakdown occurs. In this regime the resistiv-

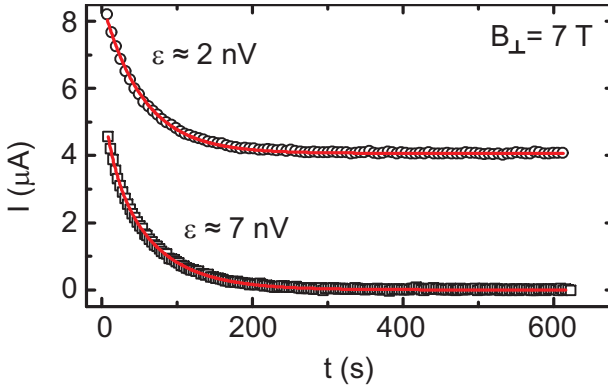


**Figure 7.7.:** Decay of the induced NECs at  $B_{\perp} = 7$  T and  $T = 0.28$  K for an initial electromotive force  $\varepsilon$  of  $\sim 2$  nV (circles) and  $\sim 7$  nV (squares). Note that the upper curve is shifted by  $4 \mu\text{A}$  for clarity. The upper curve is fitted by a simple exponential  $I = C_1 \exp(t/t_2)$  (line) and yields a decay time of  $t_2 \approx 54$  s. The lower curve exhibits two decay regimes. An initial very fast decay is followed by a smooth decay. Accordingly the data is best fitted by an exponential with two decay times of the form  $I = C_1 \exp(t/t_1) + C_2 \exp(t/t_2)$  (line). The characteristic decay times  $t_1$  and  $t_2$  are given by 15 s and 61 s, respectively.

ity is finite. The resulting dissipation induces the fast initial decay of the induced current for  $t \lesssim 20$  s. When the Hall electric field drops below a critical value, the quantum Hall state recovers. Accordingly, the decay is slowed down for  $t \gtrsim 20$  s. It is characterized by the decay time  $t_2$ . For  $\varepsilon \approx 2$  nV, we infer from Fig. 7.6 that no breakdown of the QHE occurs. Hence, the current decay is a single exponential with decay time  $t_2$ .

A semiclassical model can be applied to infer the resistivity  $\rho_{xx}$  from the current decay in the quasi-dissipationless regime. Following Refs. [Haa84, Jon95]  $\rho_{xx}$  can be expressed as

$$\rho_{xx} = \frac{\rho_{xy}}{\omega_c t_2}, \quad (7.5)$$

where  $\omega_c$  denotes the cyclotron frequency and  $\rho_{xy}$  amounts to  $h/e^2$  at  $\nu = 1$ . Inserting our values for  $t_2$  we obtain  $\rho_{xx} \approx 10^{-10} \Omega/\square$  for the "zero-resistance" resistance QHE state.

For comparison, in the experiments on the sweep rate dependence of the induced currents resistivities on the order of  $10^{-4} \Omega/\square$  were found as reported in Sec. 7.4.1.  $\rho_{xx}$  inferred from the current decay is thus several orders of magnitudes smaller. Similar discrepancies in  $\rho_{xx}$  inferred from the different experiments were also found in GaAs based 2DES. The authors of Refs. [Ker07, Ush09] attributed this discrepancy to the residual dissipation and possible QHE breakdown in the sweep rate driven experiments, which enhance the resistivity above its quasi-dissipationless value. It is likely that this effect also accounts for the differences stated here.

High mobility 2DESs in GaAs heterostructures yield decay times of several hours and resistivities on the order of  $10^{-14} \Omega/\square$  [Jon95, Ker07]. As a consequence we learn that the dissipation in the MgZnO/ZnO 2DES seems to be larger such that the decay of the induced current is much faster. This might be due to residual disorder or the presence of scattering centers in the immediate vicinity of the 2DES (see Sec. 7.5 for comparison). Further, according to Eq. 7.5 the effective electron mass in the investigated MgZnO/ZnO samples is about an order of magnitude larger compared to GaAs. According to Eq. 7.5, this effect also enhances the resistivity.

In conclusion, the decay of the NECs provides a unique tool to study the resistance of the QHE regime in a contactless configuration. In the QHE regime, elastic and inelastic backscattering are suppressed in the QHE edge channels [Büt88]. This effect guarantees the quasi-dissipationless charge transport. In contrast to magnetotransport experiments, where  $\rho_{xx}$  and  $\rho_{xy}$  exhibit zero and constant plateau values, respectively, NECs are a very sensitive gauge to probe and quantify the effective suppression of backscattering in the QHE effect regime. Thus experiments on NECs are in this sense a powerful complementary choice to characterize the QHE regime.

### 7.4.3. Temperature dependence of NECs

The temperature dependence of the NECs near  $\nu = 1$  is shown in Fig. 7.8 (a). For clarity, only the downsweeps are shown. The data was recorded at  $\alpha = 36.8^\circ$ . The temperature was varied from 0.28 K (top curve) to 1.6 K (bottom curve).  $M_{\text{NEC}}^{\text{d}}$  decreases with increasing temperature. At  $T \geq 1.1$  K the NEC was not resolved anymore. Further, the field position of the maximum of the NEC signal moves as a function of temperature. Coming from high temperatures, the maximum moves towards larger  $B$ . We denote the displacement of the NEC maxima relative to the

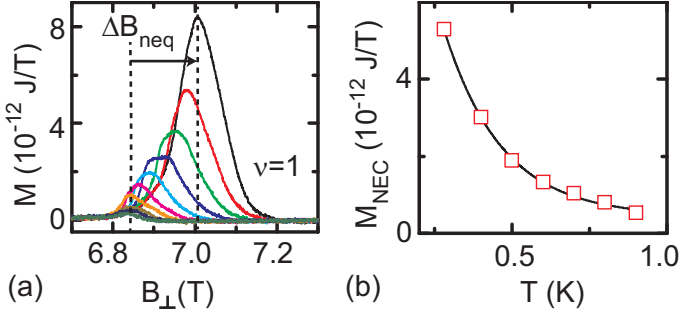


**Figure 7.8.:** (a) Temperature dependence of  $M(B)$  displayed for downsweeps at  $\nu = 1$  and  $\alpha = 36.8^\circ$ . From largest to smallest NEC signal the temperature was set to  $T = 0.28$  K, 0.4 K, 0.5 K, 0.6 K, 0.7 K, 0.8 K, 0.9 K, 1.1 K, 1.3 K and 1.6 K. Thus,  $M_{\text{NEC}}$  decreases with increasing temperature. For  $T \geq 1.1$  K no NEC signal was resolved. Going from higher to lower temperatures the maximum NEC signal moves to larger  $B$ . We denote this shift by  $\Delta B_{\text{neq}}$  relative to the position of  $\nu = 1$ . (b)  $M_{\text{NEC}}$  as a function of  $T$  (squares) and corresponding exponential fit (line).

field position of  $\nu = 1$  by  $\Delta B_{\text{neq}}$ . In Fig. 7.8 (a), the dashed lines indicate the NEC maxima at  $T = 0.28$  K as well as the position of  $\nu = 1$ . This behavior will be discussed in Sec. 7.5. Figure 7.8 (b) depicts the extracted value  $M_{\text{NEC}}$  as a function of temperature (indicated by squares). The data were fitted by a simple exponential decay  $M = M_0 \exp(-T/T_c)$ , where  $T_c = 0.19$  K is obtained as a fitting parameter.

The temperature dependent behavior can be explained by the charge redistribution model of induced currents introduced in Sec. 2.3. As pointed out in Fig. 2.7, the shape of the DOS in the region of localized states governs the temperature dependent behavior of  $M_{\text{NEC}}$ . We derived:

$$M_{\text{NEC}} = \text{const} \times \sigma_{xy} \Delta n(T) R^3 \text{ with } \Delta n = \int_{E_0/2}^{E_0/2 + k_B T \ln C} D(E) dE \quad (7.6)$$

In the case of a high mobility 2DES the DOS is exceptionally small midway between two Landau levels. Approaching the Landau levels,  $D(E)$  will significantly increase. For Gaussian shaped Landau levels as assumed in Sec. 7.3.1, the increase is exponential. Thus, according to Eq. 7.6,  $\Delta n$  decreases as  $T$  increases (note that  $\ln C$  is negative). Thus,  $M_{\text{NEC}}$  is ex-

pected to decrease exponentially with temperature. In Ref. [Mat04a] the exponential dependence of  $M_{\text{NEC}}$  as a function of temperature was also reported for a high mobility GaAs based 2DES. In contrast, for low mobility samples with high residual disorder, a linear dependence was found (c.f. Refs. [Ush09, Mat04a]). Therefore we conclude that the temperature dependence of the NECs suggest the presence of a high mobility 2DES in our MgZnO/ZnO sample with consistent characteristics as observed in high mobility GaAs based 2DESs.

## 7.5. Asymmetric density of states (DOS) and nature of scattering centers

In the previous sections we discussed the dHvA effect as well as NECs. Regarding the temperature dependence of both, dHvA effect and NECs, some features remained unexplained. As shown in Fig. 7.4, the position of  $\nu = 2$ , i.e. the steepest part of  $M(B)$ , moves to larger  $B$  for decreasing  $T$ . This field shift is manifested in an equilibrium feature. Therefore we denote the separation between the position of  $\nu = 2$  at low  $T$  and the one at  $T = 1.6$  K by  $\Delta B_{\text{eq}}$ . Concerning the NECs, a shift was observed as well as depicted in Fig. 7.8 (a). The field position of the temperature-dependent maximum in  $M_{\text{NEC}}$  shifts towards smaller magnetic field values with increasing  $T$ . The shift is a nonequilibrium magnetization phenomenon which occurs near  $\nu = 1$ . Correspondingly,  $\Delta B_{\text{neq}}$  denotes the separation between peaks at low  $T$  and the peak at  $T = 0.9$  K. Figure 7.9 (a) summarizes the relative shifts  $\Delta B_{\text{eq}}/B_{\nu=2}$  (triangles) and  $\Delta B_{\text{neq}}/B_{\nu=1}$  (squares) as a function of  $T$ .  $\Delta B_{\text{eq}}/B_{\nu=2}$  is zero for  $T > 1.1$  K and increases almost linearly with decreasing temperature below  $T \approx 1.1$  K. The behavior of  $\Delta B_{\text{neq}}/B_{\nu=1}$  is similar, except that the linear increase sets in at  $T \approx 0.8$  K. In addition, the overall relative shift  $\Delta B_{\text{neq}}/B_{\nu=1}$  is smaller than  $\Delta B_{\text{eq}}/B_{\nu=2}$  as a function of  $T$ . A linear fit, exemplarily done for  $\Delta B_{\text{neq}}/B_{\nu=1}$  (line), indicates the linear behavior at low temperatures.

The relative shift of both,  $\Delta B_{\text{neq}}$  and  $\Delta B_{\text{eq}}$ , is consistent in temperature and we thus suppose that they have the same microscopic origin. Following Ref. [Tsu07] we exclude that the observed shifts arise from temperature dependent variations in  $n_s$  as they set in only for  $T > 1$  K. Please note, that the direction of the shift in both cases coincides with the high energy

side of the Landau levels in the energy spectrum.

We first focus on  $\Delta B_{\text{neq}}$ . NECs occur when the Fermi energy resides in localized states in the QHE regime. The field position of the maximum NEC is directly connected to the field position of the minimum in  $\rho_{xx}$  [Ruh09, Kav05]. It is therefore instructive to consider magnetotransport data at this point. Figure 7.9 (b) shows results obtained on a reference MgZnO/ZnO 2DES with  $n_s = 1.7 \cdot 10^{11} \text{ cm}^{-2}$  and  $\mu = 3.8 \cdot 10^5 \text{ cm}^2/\text{Vs}$  at  $T = 0.5 \text{ K}$ . The data was provided by Y. Kozuka of the Kawasaki group.  $R_{xx}$ ,  $R_{xy}$  and the classical Hall slope extrapolated from the low field data (dashed line) are shown. At  $\nu = 2$  and  $\nu = 1$ , the Hall plateaus in  $R_{xy}$  do not occur symmetrically with respect to the classical Hall slope. Instead, the Hall plateaus as well as the  $R_{xx}$  minima are shifted to larger fields. For illustration, we included  $\Delta B_{\text{neq}}$  and  $\Delta B_{\text{eq}}$  from the magnetization data at  $T = 0.5 \text{ K}$  in Fig. 7.9 (b). The displacements in the dHvA effect and non-equilibrium magnetization are consistent with the asymmetries obtained in transport measurements. Therefore we conclude, that the microscopic origin of the separate observations is the same.

For an equilibrium property such as the dHvA effect, a temperature dependent shift has not been reported before. Instead, displacements and asymmetries of QHE plateaus and corresponding  $\rho_{xx}$  minima have already been found in transport measurements on GaAs-based heterostructures [Fur86, Hau87, Ray09]. They were attributed to scattering centers being present in the immediate vicinity of the 2DES. Repulsive scattering centers altered the DOS in such a way that it was asymmetric exhibiting an impurity tail at its high energy side [Bon06]. This feature is sketched in Fig. 7.9 (c). Conversely, attractive scatterers led to the opposite asymmetry [Ray09]. As a consequence, localized states of the lower energy level and extended states of the next higher energy level in the DOS could overlap resulting in a shift of the  $\rho_{xx}$  minima towards higher magnetic fields for repulsive scatterers. From the direction of the observed field position shifts we infer that the interaction of charge carriers and scatterers in the MgZnO/ZnO heterostructure is of repulsive nature.

We further observed a pronounced asymmetry between up- and down sweep NEC signals as shown in Fig. 7.5. In the context of an asymmetric DOS the charge redistribution model (c.f. Sec. 2.3) can explain this observation. According to Eq. 7.6  $M_{\text{NEC}}$  depends on the DOS between the LLs. If we assume an asymmetric DOS as shown in Fig. 7.9 (c),  $\Delta n$  depends crucially on the position of the Fermi level as indicated in Fig. 2.7.

It differs for the Fermi level residing above or below integer filling factor  $\nu$ . If we approach integer  $\nu$  from above (downsweep of the magnetic field) or from below (upsweep of the magnetic field) different  $\Delta n$  develop and correspondingly the  $M_{\text{NEC}}$  signals differ. Consistent with the experiment  $M_{\text{NEC}}$  is indeed expected to show an asymmetric behavior depending on the field sweep direction.

### 7.6. Indications for magnetic thaw down

We further observed spike-like overshoots of the equilibrium magnetization as denoted by the horizontal arrows in Figs. 7.1, 7.2 and 7.4 (a) showing magnetization curves near  $\nu = 2$  at  $T = 0.28$  K. This effect has also been observed near  $\nu = 1$  at elevated temperatures where NECs were absent. Temperature dependent data are shown in Fig. 7.10 (a). The overshoot decreases as the temperature increases. At  $T = 2$  K, the overshoot is absent and the pure dHvA effect is recovered. For  $T = 1.6$  K, up- and downsweep of the magnetic field are shown. Obviously, the observed overshoots do not depend on the field sweep direction which suggests an equilibrium phenomenon.

In addition, we tested the dependence of the overshoot on the illumination of the sample. Therefore a blue light-emitting-diode (LED) was used and the samples were illuminated in situ for approximately 30 s prior to further measurements. Figure 7.10 (b) shows the result at  $\nu = 2$  and at two different angles  $\alpha = 52^\circ$  and  $\alpha = 62^\circ$  before (line) and after (dotted line) illumination. At both angles, the overshoot is more pronounced after illumination. Note, that we do not observe a substantial variation of the electron density or the dHvA amplitude by the illumination of the sample. We exclude NECs as the origin of the overshoots because they do not depend on the field sweep direction. In Refs. [BS06b, BS06a] overshoots in  $M(B)$  were reported for tunnel-coupled bilayer 2DESs. The authors speculated that correlation effects or a peculiar form of the DOS were responsible for the overshoots. Considering the additional magnetotransport data taken on a MgZnO/ZnO heterostructure 2DES we attribute the overshoots in our case to an asymmetric DOS and the so-called magnetic thaw down of electrons [Bis12]: an acceptor state is negatively charged and repels conduction electrons. However, the local confinement of the electrons in the 2DES in combination with an applied magnetic field keeps the elec-



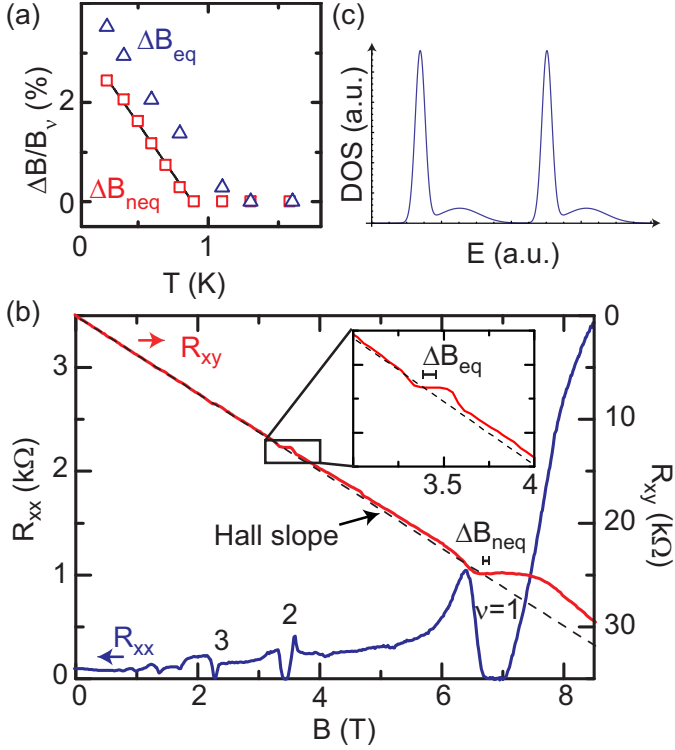


**Figure 7.9.:** (a)  $\Delta B_{\text{neq}}/B_{\nu=1}$  (squares) and  $\Delta B_{\text{eq}}/B_{\nu=2}$  (triangles) as a function of  $T$ . At low  $T$ , both,  $\Delta B_{\text{neq}}$  and  $\Delta B_{\text{eq}}$ , increase linearly with decreasing  $T$  as indicated by the black line for  $\Delta B_{\text{neq}}/B_{\nu=1}$ . Above  $T \approx 1$  K, they are both zero. (b) Transport characterization of the MgZnO/ZnO reference 2DES at  $T = 0.5$  K done by the Kawasaki group. The crossing of the Hall slope with the Hall plateaus at  $\nu = 1$  and  $\nu = 2$  does not occur in the center of the respective plateau. Instead, the plateaus as well as the  $R_{xx}$  minima are shifted to larger fields. The shifts  $\Delta B_{\text{neq}}$  and  $\Delta B_{\text{eq}}$  observed in the magnetometry experiment are indicated. (c) DOS in the presence of repulsive scatterers. An impurity tail exists at the high energy side of the LLs [Bon06].

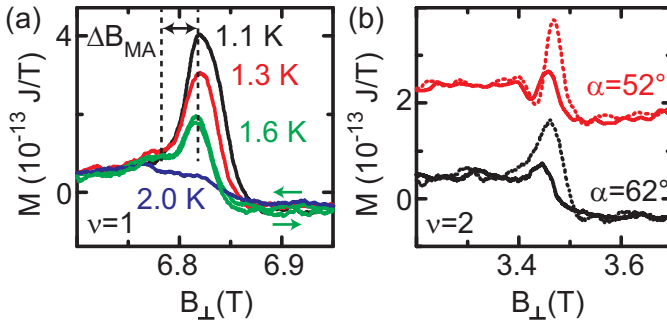


**Figure 7.10.:** (a) Temperature dependence of  $M(B_{\perp})$  near  $\nu = 1$  at  $\alpha = 52^{\circ}$ . The dHvA amplitude is superimposed by an overshoot. For  $T = 1.6$  K the up- and down-sweeps are both shown and they coincide. This indicates that the overshoot is not dependent on the field sweep direction. (b) Overshoot of the dHvA amplitude before (line) and after (dotted line) sample illumination at  $\alpha = 52^{\circ}$  and  $\alpha = 62^{\circ}$  obtained at  $T = 0.28$  K. Data are taken in the dark. The overshoot is enhanced by illumination of the sample.

tron near the acceptor. The authors of Refs. [Bis12, Bon03] attribute this behavior to a combined effect of confining potential and Lorentz force. As a result, discrete electron levels can exist above the extended Landau states. Those states are called magnetoacceptor (MA) states. This situation is schematically depicted in Fig. 7.11. If the Fermi energy resides between the localized acceptor levels and the free Landau levels electrons are transferred into the lower-lying extended Landau states. This process is referred to as magnetic thaw down [Bis12]. When the magnetic thaw down takes place, the free energy  $F$  of the electron system is reduced accordingly. Correspondingly, there is a sudden increase in  $M = -\frac{\partial F}{\partial B}$ . This process would enhance the equilibrium dHvA amplitude. It is likely that the magnetic thaw down process caused the overshoots which were observed in the experiment. Following Ref. [Wie97], we estimate the average density of the magnetoacceptors  $n_{\text{MA}}$  via  $n_{\text{MA}} = n_s \Delta B_{\text{MA}} / B_{\text{av}}$ . Here,  $\Delta B_{\text{MA}}$  denotes the field window of the rising magnetization slope as defined in Fig. 7.10 (a) and  $B_{\text{av}}$  is the mean field value. This analysis yields  $n_{\text{MA}} \approx 10^9 \text{ cm}^{-2}$ .

The observed temperature and illumination dependence is consistent with this explanation. At elevated temperatures, the Fermi distribution smears

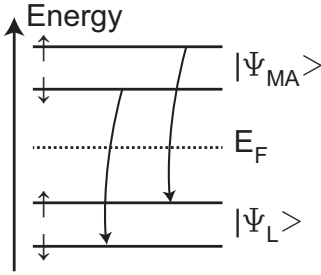


**Figure 7.11.:** Extended Landau states  $|\Psi_L\rangle$  and localized magnetoacceptor states  $|\Psi_{MA}\rangle$  in the QHE regime (after Ref. [Bis12]). When the Fermi level resides between the acceptor and Landau states, localized electrons at acceptors thaw down into delocalized Landau states.

out and the influence of the asymmetric DOS reduces. Illuminating the sample prior to the measurement might ionize potential scatterers in the vicinity of the DOS. Thus, it is likely that additional MAs are created which enhance the overshoot.

In the following we summarize the indications that support the notion of an asymmetric DOS caused by the presence of acceptor-type scatterers:

- Temperature-dependent shifts of the field position of  $\nu = 2$  by  $\Delta B_{eq}$  in the dHvA effect.
- Temperature-dependent shifts of the NEC maximum by  $\Delta B_{neq}$  observed near  $\nu = 1$ .
- In transport measurements  $R_{xx}$  minima and QHE plateaus are asymmetric with respect to the classical Hall slope.
- Overshoots of the dHvA amplitude which we attribute to magnetic thaw down.
- Asymmetry of  $M_{NEC}$  in up- and downsweeps of the magnetic field.

We attribute the origin of the asymmetric DOS to the presence of repulsive scattering centers. They form impurity bands and thereby render the DOS asymmetric. Our torque magnetometry data have allowed us to determine the nature and number of scatterers and thereby get detailed insight into the microscopic sample structure. This might help to further optimize MgZnO/ZnO heterostructures. One may now speculate about the origin of the repulsive scatterers in the immediate vicinity of the 2DES in the

## 7. Magnetization of a 2DES in a MgZnO/ZnO heterostructure

---

MgZnO/ZnO heterostructure. A possible explanation for repulsive scattering centers would be the presence of Zn vacancies at the interface, which were reported in Ref. [Ued03].

## 8. Summary and outlook

In this work, we studied the magnetization of correlated electron systems. More precisely, MnSi thin films, CrB<sub>2</sub> single crystals and 2DESs formed at the interface of MgZnO and ZnO were considered. Micromechanical cantilever magnetometry was employed to investigate the electron systems at low temperature and in high magnetic fields. The micromechanical sensors were fabricated in the framework of this thesis. We designed and tailored the sensors based on either GaAs or CuBe to suit best the experiments. This allowed us to perform highly sensitive magnetization measurements at optimized conditions with all three material systems. The experiments were conducted using vacuum-loading <sup>3</sup>He systems allowing a precise temperature control. The magnetic field was provided by superconducting magnets, either an axial 14 T magnet system or a 9 T/4.5 T vector magnet system. The latter had been set up during this thesis. Cantilever magnetometry proved to be a powerful tool to investigate the magnetization of the correlated electron systems. It is a contactless and non-invasive technique. Thereby we were able to study

- the magnetic anisotropy and the magnetic phase diagram of MnSi thin films,
- the dHvA effect and the Fermi surface topology of CrB<sub>2</sub> single crystals and
- the equilibrium and non-equilibrium magnetization phenomena in MgZnO/ZnO based 2DESs.

In the following we give separate summaries of the main results of the material systems studied. Further, a brief outlook is given.

### **MnSi thin films**

In the experiments on MnSi thin films a magnetic moment sensitivity on the order of  $10^{-11}$  J/T was reached using micromechanical sensors based

on CuBe. The experimental results allowed us to infer a preliminary magnetic phase diagram. At  $T_c \approx 39$  K the transition from a paramagnetic to a magnetically ordered phase was unambiguously identified. At the critical field  $B_c \approx 1$  T a further transition was evident, which we ascribed to a transition from a non-collinear spin state to a field polarized state. Moreover, spike-like signatures were observed at temperatures around 29 K and at a magnetic field of approximately 0.4 T. In the context of Ref. [Li13] it is possible that this phenomenon can be attributed to the skyrmion phase. Angular dependent experiments suggested a dominating uniaxial anisotropy with an easy plane. The anisotropy constants of a 10 nm and a 30 nm thick MnSi film were determined and amounted to  $7.9 \text{ kJm}^{-3}$  and  $1.2 \text{ kJm}^{-3}$ , respectively.

According to Refs. [Kar12, Li13], it is likely that MnSi thin films host a conical, a helical and a skyrmion phase below  $B_c$ . Further highly sensitive magnetometry measurements are necessary to elucidate the phase diagram in this regime. We would then expect to observe further phase transitions. In this regard, it might be fruitful to investigate thinner and smaller samples with GaAs based sensors, which allow for higher magnetic moment sensitivities.

Once the skyrmion phase is identified unambiguously, it will be interesting to combine magnetization and magnetotransport experiments. This would allow to monitor the static magnetization properties in combination with spin-transfer torque effects at the same time on the same sample. For such a combined transport-magnetization experiment the interferometric readout [Spr06] established in our group could be applied. This experiment may be promising to further characterize the magnetic properties of the skyrmion phase.

### **CrB<sub>2</sub> single crystals**

The angular and temperature dependence of the dHvA effect in a single crystal of CrB<sub>2</sub> at low temperatures was studied. Three extremal cross sections of the FS have been evaluated. The experiment suggested that all orbits are closed. The Lifshitz-Kosevich analysis of the data provided effective masses of 0.8 to  $1.22 m_e$  for the different orbits. Further, the experimental results were compared to results obtained from band structure calculations for the cycloidal magnetic order and the nonmagnetic state of

---

CrB<sub>2</sub>. We allocated two orbits to B-*p*-derived Fermi surface pockets of nearly spherical geometry. The shape of those pockets was found to be insensitive to the magnetic order. The third orbit could not be assigned to a Fermi surface pocket without ambiguity. Comparison of the measured effective masses  $m^*$  with the calculated band masses  $m_b$  yielded a mass enhancement factor of up to 2. We obtained an upper bound of the phonon coupling constants  $\lambda$  of about 1 – 1.3. General Fermi surface properties of CrB<sub>2</sub> were compared to the ones of the isostructural compound MgB<sub>2</sub> and certain analogies were identified.

In the present work, we were limited to magnetic fields below 14 T and temperatures greater than 0.3 K. It is likely that these experimental limitations are responsible for the fact that the remaining Cr-*d* derived Fermi surface pockets, which are predicted by theory, were not observed in the experiment. Thus, going to lower temperatures and larger fields might be a promising way to explore the heavy *d* electron states also. In such an experiment the heavy masses could be determined and, via a comparison with the band structure calculation, the mass enhancement may be determined. Along this line important quantitative information about the electron correlation effects could be accessed and further properties of the antiferromagnetic phase such as the nesting properties might be inferred. Despite the similarities between CrB<sub>2</sub> and MgB<sub>2</sub> concerning crystal and electronic structure, which we pointed out in Sec. 6.5, the ground state is antiferromagnetic and superconducting, respectively. Nevertheless, it is now interesting to speculate about the implications of the similarities. Since the B-*p*<sub>*x,y*</sub> orbitals in MgB<sub>2</sub> are at the heart of its superconducting properties it might be possible to generate superconducting instabilities in CrB<sub>2</sub> as well. A potential route along this line discussed in the literature [Bra13a, Bau13] is the application of hydrostatic or uniaxial pressure to CrB<sub>2</sub>. Preliminary calculations suggested that the closed, B-*p* derived Fermi pockets expand when the ratio  $c/a$  of the crystal axes is reduced. Thus CrB<sub>2</sub> might be a promising candidate to study the evolution from itinerant antiferromagnetism to superconductivity.

## 2DES at the interface of MgZnO/ZnO

In this thesis we report the first-time observation of the dHvA effect and NECs in a 2DES in an oxide heterostructure, i.e. in MgZnO/ZnO. The dHvA effect was studied as a function of field angle and temperature. We

observed quantum oscillations at filling factors smaller than  $\nu = 4$ . A Lifshitz-Kosevich analysis of the dHvA amplitude at  $\nu = 2$  allowed us to determine the effective electron mass which yielded  $m^* = 0.31 m_e$ . We further compared our data with numerical model calculations in the single particle picture. We found enhancements of the energy gaps at  $\nu = 2$  (Landau gap) as well as at  $\nu = 1$  (Zeeman gap) over the expected value in the single particle picture. The enhancement was ascribed to the exchange interaction and we determined an effective  $g^*$  factor of 5.1 at  $\nu = 1$ . NECs were observed around  $\nu = 1$ . The analysis of the decay of the induced currents enabled us to estimate the resistivity  $\rho_{xx}$  of the QHE state.  $\rho_{xx}$  amounted to  $\sim 10^{-10} \Omega/\square$  for  $\nu = 1$ . The temperature and sweep rate dependence of the NECs in MgZnO/ZnO is similar to those observed in a high-mobility GaAs based 2DES. Therefore we infer that the quality of the QHE state is comparable for the two different 2DESs. Further, we observed unexpected signatures of both, dHvA effect and NECs. The position of the steepest slope of the dHvA oscillation shifted as a function of temperature. A consistent temperature dependent shift was found when regarding the extrema of the NECs. This effect was attributed to the presence of an asymmetric DOS, which was most likely caused by repulsive scattering centers in the direct vicinity of the 2DES. The asymmetry in the DOS enables a magnetic thaw down of electrons from magnetoacceptor states. Thereby, the quantum oscillatory magnetization was enhanced even beyond the electron-electron interaction.

Future magnetization experiments may focus on the following aspects. First, we observed a renormalization of the ground state energy due to electron-electron interaction. In angular dependent transport experiments coincidence phenomena were observed from which an enhancement of the product  $g^*m^*$  was inferred [Tsu08, Koz12]. To further elucidate the exchange enhancement and possible correlation effects, the coincidence condition may be met in angular dependent magnetization measurements at higher magnetic fields. This would allow to directly monitor the ground state energy as a function of angle in the high field regime. In addition, one could correlate magnetotransport and magnetization experiments using the interferometric readout technique [Spr06]. The experiment would allow to directly compare the energy gaps inferred from excitation spectroscopy with the ones obtained from the dHvA effect.

Second, we found an enhancement of the dHvA amplitude beyond the exchange enhancement which we attributed to magnetic thaw down. Mag-



---

netic thaw down has been observed in transport experiments, but, apart from the investigations in this work, it has not been discussed in the context of the magnetization of a 2DES before. We found that illumination and temperature were control parameters to tune the relevant overshoots. Further investigations that focus on these effects may give new insights into the origin and impact of magnetic thaw down.

Oxide interfaces are likely to bring the physics of 2DESs to a new stage. The 2DES in MgZnO/ZnO combines large mobilities and effective charge carrier masses with low electron densities and a low dielectric constant. Let us first consider the transport scattering times  $\tau_{\text{tr}} = \mu m^*/e$ , which are a measure of the cleanness and quality of the 2DES [Hwa12]. In MgZnO/ZnO based 2DESs  $\tau_{\text{tr}}$  is on the order of 100 ps, which is only about one order of magnitude smaller compared to high mobility GaAs based 2DESs. This illustrates that oxide based 2DESs are not far behind semiconductor based 2DESs anymore in terms of quality and cleanness of the electron system.

At the same time MgZnO/ZnO based 2DESs display large  $r_s$  parameters. They are on the order of 10 and thus much greater than in GaAs based 2DESs. This indicates that exchange and correlation effects are far more important in the MgZnO/ZnO based 2DES.

If growth conditions can be improved further to establish 2DES exhibiting larger  $r_s$  values with increased mobility, even stronger correlation effects and eventually new physics may be observed. An example may be a metal to insulator transition in the limit of low  $n_s$  as speculated in Refs. [Gol11, Hwa12].

In conclusion, electron systems at oxide interfaces, in particular the MgZnO/ZnO based 2DESs, offer a playground for the physics of 2DESs in the limit of high mobility and large  $r_s$  parameter. They afford thus a great opportunity to search for correlation phenomena which may give rise to unforeseen physical phenomena.



# A. Electronic structure calculations for nonmagnetic CrB<sub>2</sub>

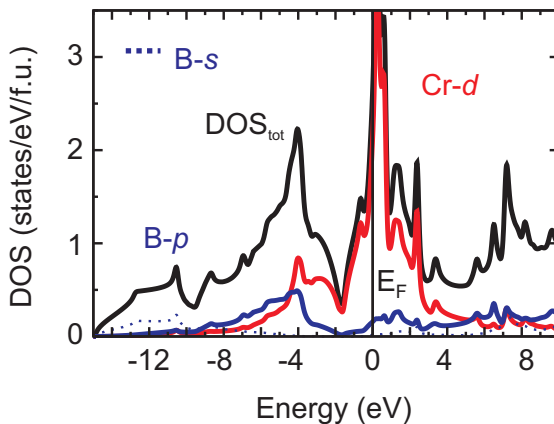


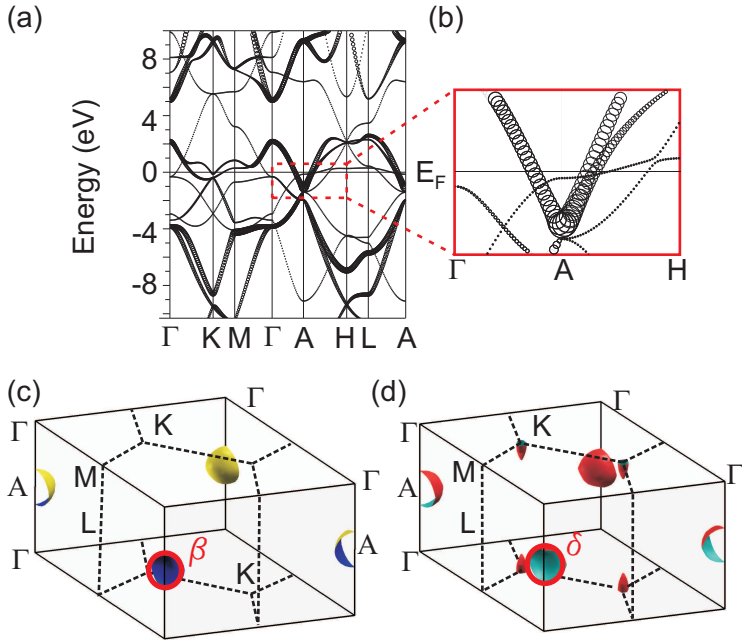
**Figure A.1.:** Density of states (DOS) of nonmagnetic CrB<sub>2</sub> calculated by L. Chioncel and J. Kuneš with the WIEN2k package [Bla12]. The main contribution to the total DOS at the Fermi level arises from Cr-*d* (red) states, but also B-*p* (blue) states are present.

Electronic structure calculations for nonmagnetic CrB<sub>2</sub> are presented in order to underscore which parts of the CrB<sub>2</sub> Fermi surface are sensitive to the exact form of the magnetic order and which parts are not. The calculations were performed by our collaboration partners J. Kuneš and L. Chioncel in the framework of the local density approximation (LDA) method of density functional theory by using the full-potential linearized augmented

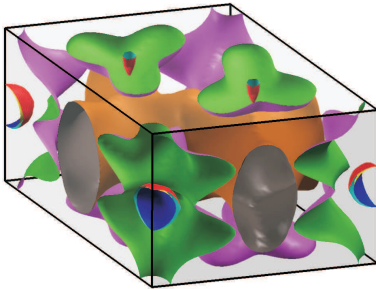
plane-wave method implemented in the WIEN2k package [Bla12]. In the calculations the experimental values for the lattice parameters  $a = 2.969 \text{ \AA}$  and  $c = 3.066 \text{ \AA}$  were used. The results of the LDA were consistent with the Generalized Gradient Approximation (GGA) of the exchange and correlation functionals.

Figure A.1 shows the total, site and orbital-projected density of states (DOS) of nonmagnetic CrB<sub>2</sub>. These results are similar to earlier works [Liu75]. At the Fermi level, by convention at 0 eV, mainly B- $p$  and Cr- $d$  states are present. Contributions from B- $s$  can be neglected. The corresponding band structure can be seen in Fig. A.2 (a). In total, four bands cross the Fermi level. The symbol size of the fat band plot denotes the strength of the in-plane B- $p_{x,y}$  orbital character. From this plot it can be deduced that two of the bands, which cross the Fermi level near the A-point, have predominantly B- $p_{x,y}$  character. These are shown in an expanded view in Fig. A.2 (b). In contrast, bands, which cross the Fermi level near other points in the Brillouin zone, have predominantly Cr- $d$  orbital character.

The corresponding Fermi surface sheets are shown in Fig. A.2 (c-d). Centered around the A-point, two electron-like Fermi surface sheets arise from bands with B- $p_{x,y}$  orbital character. In the calculations for cycloidal magnetic order reported in Chapter 6, these pockets are shifted by  $\pm \mathbf{q}/2$  away from the A-point. The shape of the B- $p$  derived sheets is, however, not significantly affected by the introduction of magnetic order. To further substantiate this important conclusion, calculations for the collinear ferromagnetic state were performed (not shown). We found that also for this case the B- $p$  pockets remain largely unaffected. These supplementary calculations thus underscore the validity of the assignment of the dHvA orbits to the B- $p$ -derived pockets made in Sec. 6.4. The remaining Fermi surface sheets have dominantly Cr- $d$  character and are radically different from the magnetically ordered states. The Fermi surface of nonmagnetic CrB<sub>2</sub> including all bands is shown in Fig. A.3.



**Figure A.2.:** Electronic structure of nonmagnetic  $\text{CrB}_2$  calculated with the WIEN2k package. (a) Band structure of  $\text{CrB}_2$ . The fat band plots indicate B- $p_{x,y}$  orbital character. The expanded view in (b) depicts two bands at the A-point that arise from in-plane B- $p_{x,y}$  orbitals and cross the Fermi level. All other bands that cross the Fermi level have predominantly Cr- $d$  orbital character. (c-d) Calculated Fermi surface sheets of  $\text{CrB}_2$  in the nonmagnetic state. Centered around the A-point, two electron-like Fermi surface sheets arise from bands with B- $p_{x,y}$  orbital character. Note that in the calculation with cycloidal magnetic order shown in Fig. 6.8, the spin degeneracy of these Fermi surface sheets is lifted and they are shifted by  $\pm \mathbf{q}/2$  away from the A-point. Their shape is, however, not significantly affected by the magnetic ordering.



**Figure A.3.:** Complete Fermi surface of nonmagnetic  $\text{CrB}_2$ . The Fermi surface sheets derived from Cr- $d$  orbitals are radically different from the ones predicted for the cycloidal magnetic order.

## B. List of abbreviations

| abbreviation     | explicit                                |
|------------------|---|
| 2DES             | two-dimensional electron system         |
| 3DES             | three-dimensional electron system       |
| CrB <sub>2</sub> | chromium diboride                       |
| CuBe             | copper beryllium                        |
| dHvA             | de Haas-van Alphen                      |
| DOS              | density-of-states                       |
| EA               | easy axis                               |
| FM               | ferromagnet                             |
| FS               | Fermi surface                           |
| GaAs             | gallium arsenide                        |
| HA               | hard axis                               |
| HFA              | Hartree-Fock approximation              |
| LK               | Lifshitz-Kosevich                       |
| LL               | Landau level                            |
| MA               | magnetoacceptor                         |
| MBE              | molecular beam epitaxy                  |
| MCM              | micromechanical cantilever magnetometer |
| MnSi             | manganese silicide                      |
| NEC              | non-equilibrium current                 |
| PM               | paramagnet                              |
| QHE              | quantum Hall effect                     |
| SE               | Schrödinger Equation                    |
| ZnO              | zinc oxide                              |





# List of Figures

|      |  |    |
|------|--|----|
| 2.1. | Coordinate system relative to the sample . . . . .   | 21 |
| 2.2. | Energy density surfaces for uniaxial anisotropy . . . . .                                    | 22 |
| 2.3. | Simulation of the torque magnetization of MnSi . . . . .                                     | 26 |
| 2.4. | Quantization of electron orbits in $\mathbf{k}$ -space . . . . .                             | 30 |
| 2.5. | DOS, chemical potential and magnetization of a 2DES . . . . .                                | 39 |
| 2.6. | Phenomenology of NECs . . . . .  | 44 |
| 2.7. | Charge redistribution model . . . . .  | 46 |
| 3.1. | Operation principle of a MCM . . . . .   | 49 |
| 3.2. | Electrostatic calibration of MCM . . . . .   | 52 |
| 3.3. | Sketch of a CuBe based cantilever . . . . .  | 53 |
| 3.4. | Schematic of the GaAs based MCM . . . . .  | 55 |
| 4.1. | Schematic of the MnSi sample . . . . .   | 58 |
| 4.2. | Crystal structure of CrB <sub>2</sub> . . . . .  | 60 |
| 4.3. | Schematic sketch of the MgZnO/ZnO heterostructure . . . . .                                  | 62 |
| 4.4. | Preparation process of the GaAs based sensors . . . . .                                      | 64 |
| 5.1. | Schematic drawing of the experimental setup . . . . .  | 68 |
| 5.2. | Torque as a function of $B$ in MnSi . . . . .  | 69 |
| 5.3. | Torque as function of $T$ in MnSi . . . . .  | 71 |
| 5.4. | Torque as function of $\varphi$ in MnSi . . . . .  | 72 |
| 5.5. | Thin film MnSi phase diagram . . . . .   | 74 |
| 5.6. | Determination of the anisotropy constant $K_u$ in MnSi . . . . .                             | 77 |
| 6.1. | Orientation of the sample on the cantilever . . . . .  | 80 |
| 6.2. | DHvA effect in CrB <sub>2</sub> . . . . .  | 81 |
| 6.3. | Angular dependence of $\alpha$ , $\beta$ and $\delta$ in the $[100] - [120]$ plane . . . . . | 82 |
| 6.4. | Angular dependence of $\beta$ in the $[001] - [120]$ plane . . . . .                         | 84 |
| 6.5. | Temperature dependence of orbits $\alpha$ and $\beta$ . . . . .                              | 85 |

|       |  |     |
|-------|--|-----|
| 6.6.  | Dingle fit of $\Gamma(B)$ . . . . .  | 86  |
| 6.7.  | Band structure of $\text{CrB}_2$ . . . . .                                     | 88  |
| 6.8.  | Fermi surface of $\text{CrB}_2$ . . . . .                                      | 89  |
| 6.9.  | Calculated angular dependence of orbits $\alpha, \beta$ and $\delta$ . . . . . | 91  |
| 7.1.  | DHvA effect in $\text{MgZnO}/\text{ZnO}$ heterostructures . . . . .            | 99  |
| 7.2.  | Angular dependence of the dHvA effect . . . . .                                | 101 |
| 7.3.  | Angular dependence of energy gaps . . . . .                                    | 104 |
| 7.4.  | Temperature dependence of the dHvA effect . . . . .                            | 105 |
| 7.5.  | Non-equilibrium-currents in $\text{MgZnO}/\text{ZnO}$ . . . . .                | 110 |
| 7.6.  | Sweep-rate dependence of NECs . . . . .  | 111 |
| 7.7.  | Decay of NECs . . . . .  | 113 |
| 7.8.  | Temperature dependence of NECs . . . . .                                       | 115 |
| 7.9.  | $T$ dependent shift of $\rho_{xx}$ minima and of $\nu = 2$ . . . . .           | 119 |
| 7.10. | Magnetic thaw down at $\nu = 1$ and $\nu = 2$ . . . . .                        | 120 |
| 7.11. | Magnetic thaw down of electrons . . . . .                                      | 121 |
| A.1.  | Density of states of nonmagnetic $\text{CrB}_2$ . . . . .                      | 129 |
| A.2.  | Electronic structure of nonmagnetic $\text{CrB}_2$ . . . . .                   | 131 |
| A.3.  | Complete Fermi surface of nonmagnetic $\text{CrB}_2$ . . . . .                 | 132 |

# Bibliography

- [Ahn03] C. H. Ahn, J.-M. Triscone und J. Mannhart: *Electric field effect in correlated oxide systems*, Nature **424**, 1015 (2003).
- [Aka10] S. Akasaka, K. Nakahara, A. Tsukazaki, A. Ohtomo und M. Kawasaki: *Mg<sub>x</sub>Zn<sub>1-x</sub>O films with a low residual donor concentration ( $<10^{15} \text{ cm}^{-3}$ ) grown by molecular beam epitaxy*, Applied Physics Express **3**, 071101 (2010).
- [Ama36] E. Amaldi und E. Fermi: *On the Absorption and the Diffusion of Slow Neutrons*, Phys. Rev. **50**, 899 (1936).
- [Amb00] O. Ambacher, B. Foutz, J. Smart, J. R. Shealy, N. G. Weimann, K. Chu, M. Murphy, A. J. Sierakowski, W. J. Schaff, L. F. Eastman, R. Dimitrov, A. Mitchell und M. Stutzmann: *Two dimensional electron gases induced by spontaneous and piezoelectric polarization in undoped and doped Al-GaN/GaN heterostructures*, Journal of Applied Physics **87**, 334 (2000).
- [And74a] T. Ando und Y. Uemura: *Theory of oscillatory g factor in an MOS inversion layer under strong magnetic fields*, Journal of the Physical Society of Japan **37**, 1044 (1974).
- [And74b] T. Ando und Y. Uemura: *Theory of quantum transport in a two-dimensional electron system under magnetic fields*, J. Phys. Soc. Jpn. **36**, 959 (1974).
- [Ard06] W. Arden: *Future semiconductor material requirements and innovations as projected in the {ITRS} 2005 roadmap*, Materials Science and Engineering: B **134**, 104 (2006).
- [Arn11] B. J. Arnold, S. Kasahara, A. I. Coldea, T. Terashima, Y. Matsuda, T. Shibauchi und A. Carrington: *Nesting of electron and hole Fermi surfaces in nonsuperconducting BaFe<sub>2</sub>P<sub>2</sub>*, Phys. Rev. B **83**, 220504 (2011).
- [Ash76] N. Ashcroft und D. Mermin: *Solid state physics*, Saunders College Publishing, 1976.
- [Bag97] D. M. Bagnall, Y. F. Chen, Z. Zhu, T. Yao, S. Koyama, M. Y. Shen und T. Goto: *Optically pumped lasing of ZnO at room temperature*, Applied Physics Letters **70**, 2230 (1997).
- [Bak80] P. Bak und M. H. Jensen: *Theory of helical magnetic structures and phase transitions in MnSi and FeGe*, Journal of Physics C: Solid State Physics **13**, L881 (1980).
- [Bal05] G. Balakrishnan, S. Majumdar, M. R. Lees und D. Mck. Paul: *Single crystal growth of CrB<sub>2</sub> using a high-temperature image furnace*, J. Cryst. Growth **274**, 294 (2005).
- [Bar48] J. Bardeen und W. H. Brattain: *The transistor, a semi-conductor triode*, Phys. Rev. **74**, 230 (1948).

- [Bar69] R. G. Barnes und R. B. Creel: *Chromium-like antiferromagnetic behavior of CrB<sub>2</sub>*, Physics Letters **29 A**, 203 (1969).
- [Bau12] A. Bauer und C. Pfleiderer: *Magnetic phase diagram of MnSi inferred from magnetization and ac susceptibility*, Phys. Rev. B **85**, 214418 (2012).
- [Bau13] A. Bauer, A. Regnat, C. Blum, S. Gottlieb-Schönmeyer, S. Wurmehl, B. Büchner und C. Pfleiderer: *High-quality single crystal growth of the itinerant antiferromagnet Cr<sup>11</sup>B<sub>2</sub>*, to be published (2013).
- [Ber11] J. Bert, B. Kalisky, C. Bell, M. Kim, Y. Hikita, H. Hwang und K. A. Moler: *Direct imaging of the coexistence of ferromagnetism and superconductivity at the LaAlO<sub>3</sub>/SrTiO<sub>3</sub> interface*, Nat Phys **7**, 767 (2011).
- [Bis12] I. Bisotto, C. Chaubet, A. Raymond, J. C. Harmand, M. Kubisa und W. Zawadzki: *Magnetic thaw down and boil-off of electrons in the quantum Hall effect regime due to magnetoacceptors in GaAs/GaAlAs heterostructures*, Phys. Rev. B **86**, 085321 (2012).
- [Blal12] P. Blaha, K. Schwarz, G. Madsen, D. Kvasnicka und J. Luitz: *WIEN2K*, Technische Universität Wien, Austria, 2012.
- [Bon03] S. Bonifacie, Y. M. Meziani, S. Juillaguet, C. Chaubet, A. Raymond, W. Zawadzki, V. Thierry-Mieg und J. Zeman: *Discrete states of conduction electrons bound to magnetoacceptors in quantum wells*, Phys. Rev. B **68**, 165330 (2003).
- [Bon06] S. Bonifacie, C. Chaubet, B. Jouault und A. Raymond: *Anharmonicity and asymmetry of Landau levels for a disordered two-dimensional electron gas*, Phys. Rev. B **74**, 245303 (2006).
- [Bra13a] M. Brasse, L. Chioncel, J. Kunes, A. Bauer, A. Regnat, C. Blum, S. Wurmehl, C. Pfleiderer, M. A. Wilde und D. Grundler: *De Haas-van Alphen effect and fermi surface properties of single crystal CrB<sub>2</sub>*, arXiv:1304.5994 (2013).
- [Bra13b] M. Brasse, S. M. Sauther, J. Falson, Y. Kozuka, A. Tsukazaki, C. Heyn, M. A. Wilde, M. Kawasaki und D. Grundler: *Enhanced quantum oscillatory magnetization and non-equilibrium currents in an interacting two-dimensional electron system in MgZnO/ZnO with repulsive scatterers*, arXiv:1307.3504 (2013).
- [BS06a] I. Bominaar-Silkens, U. Zeitler, P. Christianen, D. Reuter, A. Wieck und J. Maan: *Interaction effects observed in the magnetization of a bilayer two-dimensional electron system*, Physica E: Low-dimensional Systems and Nanostructures **34**, 191 (2006).
- [BS06b] I. M. A. Bominaar-Silkens, M. R. Schaapman, U. Zeitler, P. C. M. Christianen, J. C. Maan, D. Reuter, A. D. Wieck, D. Schuh und M. Bichler: *Magnetization of bilayer two-dimensional electron systems*, New Journal of Physics **8**, 315 (2006).
- [Bud01] S. L. Bud'ko, G. Lapertot, C. Petrovic, C. E. Cunningham, N. Anderson und P. C. Canfield: *Boron isotope effect in superconducting MgB<sub>2</sub>*, Phys. Rev. Lett. **86**, 1877 (2001).
- [Büt88] M. Büttiker: *Absence of backscattering in the quantum Hall effect in multiprobe conductors*, Phys. Rev. B **38**, 9375 (1988).

- [Bur77] J. Burd, M. Huq und E. Lee: *The determination of magnetic anisotropy constants from torque curves*, Journal of Magnetism and Magnetic Materials **5**, 135 (1977).
- [Can77] R. M. Candea, C. M. Gee, S. J. Hudgens und M. Kastner: *Temperature dependence of the diamagnetic and dielectric susceptibility of silicon*, Phys. Rev. B **16**, 2657 (1977).
- [Car03] A. Carrington, P. J. Meeson, J. R. Cooper, L. Balicas, N. E. Hussey, E. A. Yelland, S. Lee, A. Yamamoto, S. Tajima, S. M. Kazakov und J. Karpinski: *Determination of the Fermi surface of MgB<sub>2</sub> by the de Haas-van Alphen effect*, Phys. Rev. Lett. **91**, 037003 (2003).
- [Car07] A. Carrington, E. Yelland, J. Fletcher und J. Cooper: *de Haasvan Alphen effect investigations of the electronic structure of pure and aluminum-doped MgB<sub>2</sub>*, Physica C: Superconductivity **456**, 92 (2007).
- [Cas72] J. Castaing, J. Danan und M. Rieux: *Calorimetric and resistive investigation of the magnetic properties of CrB<sub>2</sub>*, Solid State Commun. **10**, 563 (1972).
- [Cav01] R. J. Cava: *Genie in a bottle*, Nature **410**, 23 (2001).
- [Chi09] S. Chikazumi: *Physics of ferromagnetism*, Oxford Science Publications, 2009.
- [Cho75] A. Y. Cho und J. Arthur: *Molecular beam epitaxy*, Prog. Solid State Chem. **10**, 157 (1975).
- [Chr94] P. Christ, W. Biberacher, H. Müller und K. Andres: *Magnetization measurements on -(BEDT-TTF)2KHg(SCN)4 [where BEDT-TTF is bis(ethylenedithio)tetrathiafulvalene]*, Solid State Communications **91**, 451 (1994).
- [Coo03] J. Cooper, A. Carrington, P. Meeson, E. Yelland, N. Hussey, L. Balicas, S. Tajima, S. Lee, S. Kazakov und J. Karpinski: *de Haasvan Alphen effect in MgB<sub>2</sub> crystals*, Physica C: Superconductivity **385**, 75 (2003).
- [Cor11] M. Corporation: *Magnetic properties of copper beryllium*, Techn. Ber. (2011).
- [Dag05] E. Dagotto: *Complexity in strongly correlated electronic systems*, Science **309**, 257 (2005).
- [Din52] R. B. Dingle: *Some magnetic properties of metals. I. General introduction, and properties of large systems of electrons*, Proc. Roy. Soc. A. **211**, 517 (1952).
- [Dya91] M. Dyakonov: *Possible mechanism for the breakdown of the quantum hall effect*, Solid State Communications **78**, 817 (1991).
- [Eis85a] J. Eisenstein, H. Störmer, V. Narayanamurti und A. Gossard: *High precision de Haas-van Alphen measurements on a two-dimensional electron gas*, Superlattices and Microstructures **1**, 11 (1985).
- [Eis85b] J. P. Eisenstein: *High-precision torsional magnetometer: Application to two-dimensional electron systems*, Applied Physics Letters **46**, 695 (1985).
- [Eng82] T. Englert, D. Tsui, A. Gossard und C. Uihlein: *g-Factor enhancement in the 2D electron gas in GaAs/AlGaAs heterojunctions*, Surface Science **113**, 295 (1982).

- [Fal11] J. Falson, D. Maryenko, Y. Kozuka, A. Tsukazaki und M. Kawasaki: *Magnesium doping controlled density and mobility of two-dimensional electron Gas in  $Mg_xZn_{1-x}O/ZnO$  heterostructures*, Applied Physics Express **4**, 091101 (2011).
- [Fau05] D. R. Faulhaber und H. W. Jiang: *Nonequilibrium magnetization of a two-dimensional electron gas in a static magnetic field*, Phys. Rev. B **72**, 233308 (2005).
- [Fed09] A. V. Fedorchenko, G. E. Grechnev, A. S. Panfilov, A. V. Logosha, I. V. Svehkarev, V. B. Filippov, A. B. Lyashchenko und A. V. Evdokimov: *Anisotropy of the magnetic properties and the electronic structure of transition-metal diborides*, Low Temperature Physics **35**, 862 (2009).
- [Fon91] P. F. Fontein, J. A. Kleinen, P. Hendriks, F. A. P. Blom, J. H. Wolter, H. G. M. Lochs, F. A. J. M. Driessen, L. J. Giling und C. W. J. Beenakker: *Spatial potential distribution in  $GaAs/Al_xGa_{1-x}As$  heterostructures under quantum Hall conditions studied with the linear electro-optic effect*, Phys. Rev. B **43**, 12090 (1991).
- [Ful12] P. Fulde: *Correlated electrons in quantum matter*, World Scientific, 2012.
- [Fun77] S. Funhashi, Y. Hamaguchi, T. Tanaka und E. Bannai: *Helical magnetic structure in  $CrB_2$* , Solid State Commun. **23**, 859 (1977).
- [Fur86] J. E. Furneaux und T. L. Reinecke: *Effects of interface charge on the quantum Hall effect*, Phys. Rev. B **33**, 6897 (1986).
- [Gar62] C. W. Garland und K. C. Park: *Low-temperature elastic constants of gallium arsenide*, Journal of Applied Physics **33**, 759 (1962).
- [Gol90] B. Goldberg, D. Heiman und A. Pinczuk: *Exchange enhancement of the spin gap of a spin-polarized 2D electron gas determined by optical absorption spectroscopy*, Surface Science **229**, 137 (1990).
- [Gol11] A. Gold: *Transport scattering time and single-particle relaxation time in  $ZnO/MgZnO$  heterostructures: Many-body effects*, Journal of Applied Physics **110**, 043702 (2011).
- [Gre09] G. E. Grechnev, A. S. Panfilov, A. V. Fedorchenko, V. B. Filippov, A. B. Lyashchenko und A. N. Visiliev: *Effect of pressure on the magnetic properties of  $CrB_2$* , Low Temperature Physics **35**, 531 (2009).
- [Gud00] V. Gudmundsson, S. I. Erlingsson und A. Manolescu: *Magnetization in short-period mesoscopic electron systems*, Phys. Rev. B **61**, 4835 (2000).
- [Haa30] W. J. de Haas und van Alphen P. M.: Proc. Netherlands Roy. Acad. Sci. **33**, 1106 (1930).
- [Haa84] T. Haavasoja, H. Störmer, D. Bishop, V. Narayanamurti, A. Gossard und W. Wiegmann: *Magnetization measurements on a two-dimensional electron system*, Surface Science **142**, 294 (1984).
- [Har99] J. G. E. Harris, D. D. Awschalom, F. Matsukura, H. Ohno, K. D. Maranowski und A. C. Gossard: *Integrated micromechanical cantilever magnetometry of  $Ga_{1-x}Mn_xAs$* , Applied Physics Letters **75**, 1140 (1999).
- [Hau87] R. J. Haug, R. R. Gerhardts, K. v. Klitzing und K. Ploog: *Effect of repulsive and attractive scattering centers on the magnetotransport properties of a two-dimensional electron gas*, Phys. Rev. Lett. **59**, 1349 (1987).

- [Hay92] M. Hayne, A. Usher, J. J. Harris und C. T. Foxon: *Exchange enhancement of the Landau-level separation for two-dimensional electrons in GaAs/Ga<sub>1-x</sub>Al<sub>x</sub>As heterojunctions*, Phys. Rev. B **46**, 9515 (1992).
- [Hig09] S. Higashi, P. Kocán und H. Tochihara: *Reactive epitaxial growth of MnSi ultrathin films on Si(111) by Mn deposition*, Phys. Rev. B **79**, 205312 (2009).
- [Hin01] D. G. Hinks, H. Claus und J. D. Joergensen: *The complex nature of superconductivity in MgB<sub>2</sub> as revealed by the reduced total isotope effect*, Nature **411**, 457 (2001).
- [Hub98] A. Hubert und R. Schäfer: *Magnetic domains: The analysis of magnetic microstructures*, Springer, 1998.
- [Hwa12] H. Y. Hwang, Y. Iwasa, M. Kawasaki, B. Keimer, N. Nagaosa und Y. Tokura: *Emergent phenomena at oxide interfaces*, Nat Mater **11**, 103 (2012).
- [Jan69] J. F. Janak: *g-factor of the two-dimensional interacting electron gas*, Phys. Rev. **178**, 1416 (1969).
- [Jon95] C. Jones, A. Usher, M. Elliott, W. Herrenden-Harker, A. Potts, R. Shepherd, T. Cheng und C. Foxon: *The decay of induced eddy currents in a two-dimensional electron system*, Solid State Communications **95**, 409 (1995).
- [Jon96] C. Jones, A. Usher, M. Elliott, W. Herrenden-Harker, A. Potts, R. Shepherd, T. Cheng und C. Foxon: *Contactless detection of current breakdown of the quantum Hall effect*, Solid State Communications **97**, 763 (1996).
- [Jon10] F. Jonietz, S. Mühlbauer, C. Pfleiderer, A. Neubauer, W. Münzer, A. Bauer, T. Adams, R. Georgii, P. Böni, R. A. Duine, K. Everschor, M. Garst und A. Rosch: *Spin transfer torques in MnSi at ultralow current densities*, Science **330**, 1648 (2010).
- [Kar10] E. Karhu, S. Kahwaji, T. L. Monchesky, C. Parsons, M. D. Robertson und C. Maunders: *Structure and magnetic properties of MnSi epitaxial thin films*, Phys. Rev. B **82**, 184417 (2010).
- [Kar11] E. A. Karhu, S. Kahwaji, M. D. Robertson, H. Fritzsche, B. J. Kirby, C. F. Majkrzak und T. L. Monchesky: *Helical magnetic order in MnSi thin films*, Phys. Rev. B **84**, 060404 (2011).
- [Kar12] E. A. Karhu, U. K. Rößler, A. N. Bogdanov, S. Kahwaji, B. J. Kirby, H. Fritzsche, M. D. Robertson, C. F. Majkrzak und T. L. Monchesky: *Chiral modulations and reorientation effects in MnSi thin films*, Phys. Rev. B **85**, 094429 (2012).
- [Kas12] Y. Kasahara, Y. Oshima, J. Falson, Y. Kozuka, A. Tsukazaki, M. Kawasaki und Y. Iwasa: *Correlation-enhanced effective mass of two-dimensional electrons in Mg<sub>x</sub>Zn<sub>1-x</sub>O/ZnO heterostructures*, Phys. Rev. Lett. **109**, 246401 (2012).
- [Kav05] K. Kavokin, M. Portnoi, A. Matthews, A. Usher, J. Gething, D. Ritchie und M. Simmons: *Induced currents, frozen charges and the quantum Hall effect breakdown*, Solid State Communications **134**, 257 (2005).
- [Ker07] T. J. Kershaw, A. Usher, A. S. Sachrajda, J. Gupta, Z. R. Wasilewski, M. Elliott, D. A. Ritchie und M. Y. Simmons: *Decay of long-lived quantum Hall induced currents in 2D electron systems*, New Journal of Physics **9**, 71 (2007).

- [Kit78] Y. Kitaoka, H. Yasuoka, T. Tanaka und Y. Ishizawa: *Nuclear magnetic resonance of  $^{11}\text{B}$  in  $\text{CrB}_2$* , Solid State Commun. **26**, 87 (1978).
- [Kit80] Y. Kitaoka und H. Yasuoka: *NMR-investigations on the spin fluctuations in itinerant antiferromagnets III.  $\text{CrB}_2$* , J. Phys. Soc. Jpn. **49**, 493 (1980).
- [Kli80] K. v. Klitzing, G. Dorda und M. Pepper: *New method for high-accuracy determination of the fine-structure constant based on quantized Hall resistance*, Phys. Rev. Lett. **45**, 494 (1980).
- [Kob80] I. Kobiakov: *Elastic, piezoelectric and dielectric properties of  $\text{ZnO}$  and  $\text{CdS}$  single crystals in a wide range of temperatures*, Solid State Communications **35**, 305 (1980).
- [Kor01] J. Kortus, I. I. Mazin, K. D. Belashchenko, V. P. Antropov und L. L. Boyer: *Superconductivity of metallic boron in  $\text{MgB}_2$* , Phys. Rev. Lett. **86**, 4656 (2001).
- [Koz12] Y. Kozuka, A. Tsukazaki, D. Maryenko, J. Falson, C. Bell, M. Kim, Y. Hikita, H. Y. Hwang und M. Kawasaki: *Single-valley quantum Hall ferromagnet in a dilute  $\text{Mg}_x\text{Zn}_{1-x}\text{O}/\text{ZnO}$  strongly correlated two-dimensional electron system*, Phys. Rev. B **85**, 075302 (2012).
- [Kun04] J. Kuneš und R. Laskowski: *Magnetic ground state and Fermi surface of bcc Eu*, Phys. Rev. B **70**, 174415 (2004).
- [Las04] R. Laskowski, G. K. H. Madsen, P. Blaha und K. Schwarz: *Magnetic structure and electric-field gradients of uranium dioxide: An ab initio study*, Phys. Rev. B **69**, 140408 (2004).
- [Lee09] M. Lee, W. Kang, Y. Onose, Y. Tokura und N. P. Ong: *Unusual Hall effect anomaly in  $\text{MnSi}$  under pressure*, Phys. Rev. Lett. **102**, 186601 (2009).
- [Lee13] J.-S. Lee, Y. W. Xie, H. K. Sato, C. Bell, Y. Hikita, H. Y. Hwang und C.-C. Kao: *Titanium  $d_{xy}$  ferromagnetism at the  $\text{LaAlO}_3/\text{SrTiO}_3$  interface*, Nat Mater **12**, 703 (2013).
- [Li13] Y. Li, N. Kanazawa, X. Z. Yu, A. Tsukazaki, M. Kawasaki, M. Ichikawa, X. F. Jin, F. Kagawa und Y. Tokura: *Robust formation of skyrmions and topological Hall effect anomaly in epitaxial thin films of  $\text{MnSi}$* , Phys. Rev. Lett. **110**, 117202 (2013).
- [Lif54] I. Lifshitz und A. Kosevich: Doklady Akademii Nauk **96**, 963 (1954).
- [Lif55] I. Lifshitz und A. Kosevich: Zh. eksp. teor. fiz. **29**, 730 (1955).
- [Liu75] S. H. Liu, L. Kopp, W. B. England und H. W. Myron: *Energy bands, electronic properties and magnetic ordering of  $\text{CrB}_2$* , Physical Review B **11**, 3463 (1975).
- [Liu01] A. Y. Liu, I. I. Mazin und J. Kortus: *Beyond Eliashberg superconductivity in  $\text{MgB}_2$ : Anharmonicity, two-phonon scattering, and multiple gaps*, Phys. Rev. Lett. **87**, 087005 (2001).
- [Mac86] A. H. MacDonald, H. C. A. Oji und K. L. Liu: *Thermodynamic properties of an interacting two-dimensional electron gas in a strong magnetic field*, Phys. Rev. B **34**, 2681 (1986).
- [Man95] A. Manolescu und R. R. Gerhardt: *Exchange-enhanced spin splitting in a two-dimensional electron system with lateral modulation*, Phys. Rev. B **51**, 1703 (1995).



- [Man97] A. Manolescu und R. R. Gerhardt: *Coulomb effects on the quantum transport of a two-dimensional electron system in periodic electric and magnetic fields*, Phys. Rev. B **56**, 9707 (1997).
- [Man10] J. Mannhart und D. G. Schlom: *Oxide interfaces - An opportunity for electronics*, Science **327**, 1607 (2010).
- [Mat04a] A. J. Matthews, K. V. Kavokin, A. Usher, M. E. Portnoi, M. Zhu, J. D. Gething, M. Elliott, W. G. Herrenden-Harker, K. Phillips, D. A. Ritchie, M. Y. Simmons, C. B. Sorensen, O. P. Hansen, O. A. Mironov, M. Myronov, D. R. Leadley und M. Henini: *Temperature dependence of the breakdown of the quantum Hall effect studied by induced currents*, Phys. Rev. B **70**, 075317 (2004).
- [Mat04b] A. J. Matthews, A. Usher und C. D. H. Williams: *A low-temperature high-sensitivity torsion balance magnetometer with in situ stator adjustment*, Review of Scientific Instruments **75**, 2672 (2004).
- [Maz02] I. I. Mazin und J. Kortus: *Interpretation of the de Haas-van Alphen experiments in MgB<sub>2</sub>*, Phys. Rev. B **65**, 180510 (2002).
- [Mei97] I. Meinel, D. Grundler, S. Bargstädt-Franke, C. Heyn, D. Heitmann und B. David: *High-sensitive superconducting magnetometry on a two-dimensional electron gas up to 10 Tesla*, Applied Physics Letters **70**, 3305 (1997).
- [Mei99] I. Meinel, T. Hengstmann, D. Grundler, D. Heitmann, W. Wegscheider und M. Bichler: *Magnetization of the fractional Quantum Hall states*, Phys. Rev. Lett. **82**, 819 (1999).
- [Mei01] I. Meinel, D. Grundler, D. Heitmann, A. Manolescu, V. Gudmundsson, W. Wegscheider und M. Bichler: *Enhanced magnetization at integer quantum Hall states*, Phys. Rev. B **64**, 121306 (2001).
- [Mic07] C. Michioka, Y. Itoh, K. Yoshimura, Y. Watabe, Y. Kousaka, H. Ichikawa und J. Akimitsu: *NMR studies of single crystal chromium diboride*, Journal of Magnetic Materials **310**, 620 (2007).
- [Moo65] G. Moore: *Cramming more components onto integrated circuits*, Electronics **38**, 114 (1965).
- [Mor01] A. Morrish: *The physical principals of magnetism*, IEEE Press, 2001.
- [Müh09] S. Mühlbauer, S. Hlbauer, B. Binz, F. Jonietz, C. Pfleiderer, A. Rosch, A. Neubauer, R. Georgii und P. Böni: *Skyrmion lattice in a chiral magnet*, Science **323**, 915 (2009).
- [Nac99] G. Nachtwei: *Breakdown of the quantum Hall effect*, Physica E: Low-dimensional Systems and Nanostructures **4**, 79 (1999).
- [Nag01] J. Nagamatsu, N. Nakagawa, T. Muranaka, Y. Zenitani und J. Akimitsu: *Superconductivity at 39 K in magnesium diboride*, Nature **410**, 63 (2001).
- [Neu09] A. Neubauer, C. Pfleiderer, B. Binz, A. Rosch, R. Ritz, P. G. Niklowitz und P. Böni: *Topological Hall effect in the A phase of MnSi*, Phys. Rev. Lett. **102**, 186602 (2009).
- [Nic88] R. J. Nicholas, R. J. Haug, K. v. Klitzing und G. Weimann: *Exchange enhancement of the spin splitting in a GaAs-Ga<sub>x</sub>Al<sub>1-x</sub>As heterojunction*, Phys. Rev. B **37**, 1294 (1988).

- [Nom03] K. Nomura, H. Ohta, K. Ueda, T. Kamiya, M. Hirano und H. Hosono: *Thin-film transistor fabricated in single-crystalline transparent oxide semiconductor*, Science **300**, 1269 (2003).
- [Oht04] A. Ohtomo und H. Hwang: *A high mobility electron gas at the LaAlO<sub>3</sub>/SrTiO<sub>3</sub> heterointerface*, Nature **427**, 423 (2004).
- [Ons52] L. Onsager: *Interpretation of the de Haas-van Alphen effect*, Philosophical Magazine **43**, 1006 (1952).
- [Pfl04] C. Pfleiderer, D. Reznik, L. Pintschovius, H. v. Lohneysen, M. Garst und A. Rosch: *Partial order in the non-Fermi-liquid phase of MnSi*, Nature **427**, 227 (2004).
- [Pic02] W. Pickett: *Mind the double gap*, Nature **418**, 733 (2002).
- [Ram07] A. P. Ramirez: *Oxide electronics emerge*, Science **315**, 1377 (2007).
- [Ray09] A. Raymond, I. Bisotto, Y. M. Meziani, S. Bonifacie, C. Chaubet, A. Cavanaugh und J. C. Harmand: *Effects of repulsive and attractive ionized impurities on the resistivity of semiconductor heterostructures in the quantum Hall regime*, Phys. Rev. B **80**, 195316 (2009).
- [Reg] Private communication with A. Regnat (E21, physics dep., TU München).
- [Rey65] D. C. Reynolds, C. W. Litton und T. C. Collins: *Zeeman effects in the edge emission and absorption of ZnO*, Phys. Rev. **140**, A1726 (1965).
- [Rey07] N. Reyren, S. Thiel, A. D. Caviglia, L. F. Kourkoutis, G. Hammerl, C. Richter, C. W. Schneider, T. Kopp, A.-S. Retschi, D. Jaccard, M. Gabay, D. A. Muller, J.-M. Triscone und J. Mannhart: *Superconducting interfaces between insulating oxides*, Science **317**, 1196 (2007).
- [Rit13] R. Ritz, M. Halder, M. Wagner, C. Franz, A. Bauer und C. Pfleiderer: *Formation of a topological non-Fermi liquid in MnSi*, Nature **497**, 231 (2013).
- [Rou12] P. Rourke und S. Julian: *Numerical extraction of de Haasvan Alphen frequencies from calculated band energies*, Computer Physics Communications **183**, 324 (2012).
- [Ruh06] N. Ruhe, J. I. Springborn, C. Heyn, M. A. Wilde und D. Grundler: *Simultaneous measurement of the de Haas-van Alphen and the Shubnikov-de Haas effect in a two-dimensional electron system*, Phys. Rev. B **74**, 235326 (2006).
- [Ruh09] N. Ruhe, G. Stracke, C. Heyn, D. Heitmann, H. Hardtdegen, T. Schäpers, B. Rupperecht, M. A. Wilde und D. Grundler: *Origin and limiting mechanism of induced nonequilibrium currents in gated two-dimensional electron systems*, Phys. Rev. B **80**, 115336 (2009).
- [Rup13] B. Rupperecht, S. Heedt, H. Hardtdegen, T. Schäpers, C. Heyn, M. A. Wilde und D. Grundler: *Frequency anomaly in the Rashba-effect induced magnetization oscillations of a high-mobility two-dimensional electron system*, Phys. Rev. B **87**, 035307 (2013).
- [San98] L. M. Sandratskii: *Noncollinear magnetism in itinerant-electron systems: Theory and applications*, Advances in Physics **47**, 91 (1998).
- [Sch00] M. P. Schwarz, D. Grundler, I. Meinel, C. Heyn und D. Heitmann: *Micromechanical cantilever magnetometer with an integrated two-dimensional electron system*, Applied Physics Letters **76**, 3564 (2000).

- [Sch02] M. P. Schwarz, M. A. Wilde, S. Groth, D. Grundler, C. Heyn und D. Heitmann: *Sawtoothlike de Haas-van Alphen oscillations of a two-dimensional electron system*, Phys. Rev. B **65**, 245315 (2002).
- [Sch03] M. P. Schwarz, D. Grundler, C. Heyn, D. Heitmann, D. Reuter und A. Wieck: *Induced nonequilibrium currents in the magnetization of mesoscopic dots in the quantum Hall regime*, Phys. Rev. B **68**, 245315 (2003).
- [Sch12a] J. M. Schneider, B. A. Piot, I. Sheikin und D. K. Maude: *Using the de Haas-van Alphen effect to map out the closed three-dimensional Fermi surface of natural graphite*, Phys. Rev. Lett. **108**, 117401 (2012).
- [Sch12b] T. Schulz, R. Ritz, A. Bauer, M. Halder, M. Wagner, C. Franz, C. Pfeleiderer, K. Everschor, M. Garst und A. Rosch: *Emergent electrodynamics of skyrmions in a chiral magnet*, Nat Phys **8**, 301 (2012).
- [Sek12] S. Seki, X. Z. Yu, S. Ishiwata und Y. Tokura: *Observation of skyrmions in a multiferroic material*, Science **336**, 198 (2012).
- [Sho84] D. Shoenberg: *Magnetic oscillations in metals*, Cambridge University Press, 1984.
- [Sig92] T. I. Sigfusson, K. P. Emilsson und P. Mattocks: *Application of the maximum-entropy technique to the analysis of de Haas-van Alphen data*, Phys. Rev. B **46**, 10446 (1992).
- [Sko08] R. Skomski: *Simple models of magnetism*, Oxford University Press, 2008.
- [Smi12] M. J. Smith, A. Usher, C. D. H. Williams, A. Shytov, A. S. Sachrajda, A. Kam und Z. R. Wasilewski: *Induced currents in the quantum Hall regime: Energy storage, persistence, and I-V characteristics*, Phys. Rev. B **86**, 195314 (2012).
- [Spr06] J. Springborn, N. Ruhe, C. Heyn, M. Wilde, D. Heitmann und D. Grundler: *Gate-controlled de Haas-van Alphen effect in an interacting two-dimensional electron system*, Physica E: Low-dimensional systems and nanostructures **34**, 172 (2006).
- [Stö83] H. L. Störmer, T. Haavasoja, V. Narayanamurti, A. C. Gossard und W. Wiegmann: *Observation of the de Haas-van Alphen effect in a two-dimensional electron system*, Journal of Vacuum Science & Technology B: Microelectronics and Nanometer Structures **1**, 423 (1983).
- [Sto48] E. Stoner und E. Wohlfahrt: *A mechanism of magnetic hysteresis in heterogeneous alloys*, Philos. Trans. R. Soc. London **240**, 599 (1948).
- [Suz93] T. Suzuki: *Heavy fermion state in low carrier concentration systems for rare earth pnictides and chalcogenides*, Physica B: Condensed Matter **186/188**, 347 (1993).
- [Tam08] H. Tampo, H. Shibata, K. Maejima, A. Yamada, K. Matsubara, P. Fons, S. Kashiwaya, S. Niki, Y. Chiba, T. Wakamatsu und H. Kanie: *Polarization-induced two-dimensional electron gases in ZnMgO/ZnO heterostructures*, Applied Physics Letters **93**, 202104 (2008).
- [Tam09] H. Tampo, H. Shibata, K. Maejima, T.-W. Chiu, H. Itoh, A. Yamada, K. Matsubara, P. Fons, Y. Chiba, T. Wakamatsu, Y. Takeshita, H. Kanie und S. Niki: *Band profiles of ZnMgO/ZnO heterostructures confirmed by Kelvin probe force microscopy*, Applied Physics Letters **94**, 242107 (2009).

- [Tem88] I. M. Templeton: *A high-sensitivity torsional magnetometer for two-dimensional electron systems*, Journal of Applied Physics **64**, 3570 (1988).
- [Tim72] S. Timoshenko: *Mechanics of materials*, Van Nostrand Reinhold, 1972.
- [Tok00] Y. Tokura und N. Nagaosa: *Orbital physics in transition-metal oxides*, Science **288**, 462 (2000).
- [Ton12] A. Tonomura, X. Yu, K. Yanagisawa, T. Matsuda, Y. Onose, N. Kanazawa, H. S. Park und Y. Tokura: *Real-space observation of skyrmion lattice in helimagnet MnSi thin samples*, Nano Letters **12**, 1673 (2012).
- [Tsu07] A. Tsukazaki, A. Ohtomo, T. Kita, Y. Ohno, H. Ohno und M. Kawasaki: *Quantum Hall effect in polar oxide heterostructures*, Science **315**, 1388 (2007).
- [Tsu08] A. Tsukazaki, A. Ohtomo, M. Kawasaki, S. Akasaka, H. Yuji, K. Tamura, K. Nakahara, T. Tanabe, A. Kamisawa, T. Gokmen, J. Shabani und M. Shayegan: *Spin susceptibility and effective mass of two-dimensional electrons in  $\text{Mg}_x\text{Zn}_{1-x}\text{O}/\text{ZnO}$  heterostructures*, Phys. Rev. B **78**, 233308 (2008).
- [Tsu10] A. Tsukazaki, S. Akasaka, K. Nakahara, Y. Ohno, H. Ohno, D. Maryenko, A. Ohtomo und M. Kawasaki: *Observation of the fractional quantum Hall effect in an oxide*, Nat Mater **9**, 889 (2010).
- [Ued03] A. Uedono, T. Koida, A. Tsukazaki, M. Kawasaki, Z. Q. Chen, S. Chichibu und H. Koinuma: *Defects in ZnO thin films grown on  $\text{ScAlMgO}_4$  substrates probed by a monoenergetic positron beam*, Journal of Applied Physics **93**, 2481 (2003).
- [Ush09] A. Usher und M. Elliott: *Magnetometry of low-dimensional electron and hole systems*, Journal of Physics: Condensed Matter **21**, 103202 (2009).
- [Vaj01] P. Vajeeston, P. Ravindran, C. Ravi und R. Asokamani: *Electronic structure, bonding, and ground-state properties of  $\text{AlB}_2$ -type transition-metal diborides*, Physical Review B **63**, 045115 (2001).
- [Was96] A. Wasserman und M. Springford: *The influence of many-body interactions on the de Haas-van Alphen effect*, Advances in Physics **45**, 471 (1996).
- [Wie97] S. A. J. Wieggers, M. Specht, L. P. Lévy, M. Y. Simmons, D. A. Ritchie, A. Cavanna, B. Etienne, G. Martinez und P. Wyder: *Magnetization and energy gaps of a high-mobility 2D electron gas in the quantum limit*, Phys. Rev. Lett. **79**, 3238 (1997).
- [Wie98] S. A. J. Wieggers, A. S. van Steenberghe, M. E. Jeuken, M. Bravin, P. E. Wolf, G. Remenyi, J. A. A. J. Perenboom und J. C. Maan: *A sensitive and versatile torque magnetometer for use in high magnetic fields*, Review of Scientific Instruments **69**, 2369 (1998).
- [Wil98] M. Willemin, C. Rossel, J. Brugger, M. H. Despont, H. Rothuizen, P. Vettiger, J. Hofer und H. Keller: *Piezoresistive cantilever designed for torque magnetometry*, Journal of Applied Physics **83**, 1163 (1998).
- [Wie] Private communication with B. Wiedemann (chair E21, physics dep., TU München).
- [Wil04a] M. Wilde: *Magnetization measurements on low-dimensional electron systems in high-mobility GaAs and SiGe heterostructures*, Dissertation, University of Hamburg (2004).

- [Wil04b] M. Wilde, J. Springborn, C. Heyn, D. Heitmann und D. Grundler: *Magnetization of GaAs quantum wires with quasi one-dimensional electron systems*, Physica E: Low-dimensional Systems and Nanostructures **22**, 729 (2004).
- [Wil08] M. A. Wilde, J. I. Springborn, O. Roesler, N. Ruhe, M. P. Schwarz, D. Heitmann und D. Grundler: *Magnetometry on quantum Hall systems: Thermodynamic energy gaps and the density of states distribution*, physica status solidi (b) **245**, 344 (2008).
- [Wil10] M. Wilde, D. Grundler und D. Heitmann: *Quantum materials*, Springer, 2010.
- [Xi08] X. X. Xi: *Two-band superconductor magnesium diboride*, Reports on Progress in Physics **71**, 116501 (2008).
- [Yan07] M. Yano, K. Hashimoto, K. Fujimoto, K. Koike, S. Sasa, M. Inoue, Y. Uetsuji, T. Ohnishi und K. Inaba: *Polarization-induced two-dimensional electron gas at Zn<sub>1-x</sub>Mg<sub>x</sub>O/ZnO heterointerface*, Journal of Crystal Growth **301302**, 353 (2007).
- [Yel02] E. A. Yelland, J. R. Cooper, A. Carrington, N. E. Hussey, P. J. Meeson, S. Lee, A. Yamamoto und S. Tajima: *de Haas-van Alphen Effect in Single Crystal MgB<sub>2</sub>*, Phys. Rev. Lett. **88**, 217002 (2002).
- [Yu10a] X. Z. Yu, Y. Onose, N. Kanazawa, J. H. Park, J. H. Han, Y. Matsui, N. Nagaosa und Y. Tokura: *Real-space observation of a two-dimensional skyrmion crystal*, Nature **465**, 901 (2010).
- [Yu10b] X. Z. Yu, Y. Onose, N. Kanazawa, J. H. Park, J. H. Han, Y. Matsui, N. Nagaosa und Y. Tokura: *Real-space observation of a two-dimensional skyrmion crystal*, Nature **465**, 901 (2010).
- [Zhu03] M. Zhu, A. Usher, A. J. Matthews, A. Potts, M. Elliott, W. G. Herrenden-Harker, D. A. Ritchie und M. Y. Simmons: *Magnetization measurements of high-mobility two-dimensional electron gases*, Phys. Rev. B **67**, 155329 (2003).
- [Zim65] J. Ziman: *Principles of the theory of solids*, Cambridge University Press, 1965.



# Publications

- A. Brandlmaier, M. Brasse, S. Geprägs, M. Weiler, R. Gross, S. T. B. Goennenwein: *Magneto-optical imaging of elastic strain-controlled magnetization reorientation*, Eur. Phys. J. B **85**, 124 (2012).
- M. Brasse, L. Chioncel, J. Kuneš, A. Bauer, A. Regnat, C. G. F. Blum, S. Wurmehl, C. Pfleiderer, M. A. Wilde, and D. Grundler: *De Haas-van Alphen effect and Fermi surface properties of single crystal CrB<sub>2</sub>*, Physical Review B **88**, 155138 (2013).
- M. Brasse, S. M. Sauther, J. Falson, Y. Kozuka, A. Tsukazaki, Ch. Heyn, M. A. Wilde, M. Kawasaki and D. Grundler: *Enhanced quantum oscillatory magnetization and non-equilibrium currents in an interacting two-dimensional electron system in MgZnO/ZnO with repulsive scatterers*, accepted by Physical Review B, (2014).





# Acknowledgments

I would like to express my gratitude to all the people who contributed to this work and supported me during my Ph.D. time. In particular:

- Prof. Dr. Dirk Grundler for giving me the opportunity to work at E10 and for the supervision of this thesis. I thank him for the many fruitful discussions, for sharing his deep scientific insight and for the kind support at all times.
- Dr. Marc Wilde for his overall support and guidance throughout this work. In particular I want to thank him for the countless discussions concerning scientific or technical issues, for his encouragement when we encountered problems and for his open door at all times.
- cantilever coworkers: Stephan Albert, Florian Herzog, Benedikt Rupprecht and Tjark Windisch for their helping hands and great support. It was a pleasure to work with you.
- diploma and bachelor students: Amadeus Mlynarski, Schorsch Sauter, Mathias Frank and Ludwig Schaidhammer for their commitment and contributions to this work.
- collaborators at TU München, chair E21: Andreas Bauer, Alexander Regnat and Prof. Christian Pfeleiderer for providing me with the CrB<sub>2</sub> sample, for the many illuminating scientific discussions and the support during the publication process of the CrB<sub>2</sub> manuscript; Birgit Wiedemann and Prof. Peter Böni for providing us with MnSi thin films and Cr single crystals and for the helpful scientific exchange.
- Dr. Jan Kuneš, Academy of Sciences, Prague, Czech Republic and Prof. Livio Chioncel, University of Augsburg for the band structure calculations of CrB<sub>2</sub> and the helpful discussions.
- Dr. Y. Kozuka and Prof. M. Kawasaki, University of Tokyo, Japan, for providing me with MgZnO/ZnO samples and for the collaborative efforts.

## Acknowledgments

---

- Prof. Thorsten Hesjedal, University of Oxford, UK for the growth of the MnSi thin films.
- Dr. Rainer Jany, University of Augsburg, and Prof. Dr. Jochen Mannhart, MPI-FKF Stuttgart, for the SrTiO<sub>3</sub>/LaAlO<sub>3</sub> samples and the scientific exchange.
- Dr. Christian Heyn, University of Hamburg, for the GaAs heterostructures.
- E10 technical and organizational staff for the helping hands on short notice and for the support.
- all other E10 group members for the enjoyable working atmosphere, for sharing a good time and many laughs.
- my family and Martina, for their unlimited support in every aspect and just for being always there!

This research has received funding from the TRR 80: *From Electronic Correlations to Functionality* which is gratefully acknowledged.